DISSERTATION
submitted to the
COMBINED FACULTY OF
NATURAL SCIENCES AND MATHEMATICS
of the
RUPERTO-CAROLA-UNIVERSITY OF HEIDELBERG,
GERMANY
for the degree of
DOCTOR OF NATURAL SCIENCES

Put forward by

M. Sc. Mei Sasaki
born in: Tokyo, Japan

Oral examination: 4 February 2015

Statistical properties of dark matter mini-haloes and the criterion for HD formation in the early universe

Referees:

Prof. Dr. Ralf S. Klessen

Prof. Dr. Norbert Christlieb

Dedicated to my parents, my sister, and my fiancé Takashi Moriya.

Abstract

The aim of this work is to explore how dark matter structures and astronomical objects (the first generation of stars) formed in the high-redshift universe. We investigate properties of dark matter mini-haloes and clarify the process of primordial star formation that takes place in different dark matter mini-haloes. The specific questions that we aim to answer in this work include how dark matter mini-haloes found at $z \geq 15$ differ from their more massive lower-redshift counterparts and what determines the amount of HD that forms in primordial gas at the initial stage of protostellar collapse. We ran a high-resolution N-body simulation that has the highest mass resolution ever achieved for a representative cosmological volume at these high redshifts, and made precision measurements of various physical properties that characterise dark matter haloes. As expected from the differences in the slope of the dark matter density power spectrum, the dependence of formation time on dark matter halo mass is very weak in the case of the haloes that we study here. Despite this difference, dark matter structures at high redshift share many properties with their much more massive counterparts that form at later times. We ran a separate set of cosmological hydrodynamical simulations to study gas starting to collapse in dark matter haloes. We found that in some of our simulated mini-haloes, HD cooling became important during the initial collapse, and investigated in detail why this occurred. We compared HD-rich and HD-poor mini-haloes in our simulations and found that the amount of HD that forms is linked to the speed of the gravitational collapse. If the collapse is rapid, dynamical heating prevents the gas from cooling to temperatures low enough for HD cooling to become important, but if the collapse is slow, HD cooling can come to dominate, resulting in a minimum gas temperature which is lower by a factor of two. We investigated what properties of the mini-haloes were responsible for determining the collapse time, and showed that, contrary to previous suggestions, the mass of the mini-halo and the rotational energy of the gas appear to have little influence on the speed of the collapse. We therefore suspect that the main factor determining whether the collapse is slow or rapid, and hence whether HD cooling becomes important or not, is the degree of turbulence in the gas.

Zusammenfassung

Das Ziel dieser Arbeit ist es, die Struktur von Dunkler Materie und astronomischen Objekten (der ersten Generation von Sternen), die im frühen Universum entstanden sind, zu erforschen. Wir untersuchen die Eigenschaften von Dunkle Materie Mini-Halos und den Prozess der primordialen Sternentstehung, der in den verschiedenen Mini-Halos stattfindet. Die genauen Fragestellungen, die wir in dieser Arbeit verfolgen, beinhalten, ob sich Mini-Halos bei einer Rotverschiebung von $z \geq 15$ von ihren massiveren Gegenstücken zu späteren Zeiten unterscheiden und was die Menge an HD bestimmt, die sich im primordialen Gas am Beginn des protostellaren Kollaps bildet. Wir haben eine hochaufgelöste N-Körper Simulation durchgeführt, welche die höchste jemals erreichte Massen-Auflösung in einem repräsentativen kosmologischen Volumen bei dieser hohen Rotverschiebung hat und präzise Messungen von verschiedenen physikalischen Größen durchgeführt, welche die Eigenschaften der Dunkle Materie Halos charakterisieren. In den hier untersuchten Halos hängt die Entstehungszeit nur schwach von der Masse der Dunkle Materie Halos ab, wie aus den unterschiedlichen Steigungen der Dichte-Leistungsspektren zu erwarten war. Trotz dieses Unterschieds teilen die Dunkle Materie Strukturen bei hoher Rotverschiebung viele Eigenschaften mit ihren massiveren Gegenstücken, die später entstehen. Wir haben zusätzlich eine Reihe von kosmologischen hydrodynamischen Simulationen durchgeführt, um Gas zu untersuchen, das gerade beginnt, in den Halos zu kollabieren. In einigen unserer simulierten Mini-Halos wurde Kühlen durch HD während des anfänglichen Kollaps wichtig, und wir verfolgen den Grund dafür im Detail. Aus dem Vergleich von HD-reichen und HD-armen Mini-Halos in unserer Simulation ergibt sich, dass die Menge von HD, die gebildet wird, mit der Geschwindigkeit des Gravitations-Kollapses zusammenhängt. Wenn der Kollaps schnell verläuft, verhindert dynamisches Heizen, dass HD-Kühlen wichtig wird, das erst bei niedrigen Temperaturen einsetzt. Falls der Kollaps langsam ist, kann HD-Kühlen dominant werden, wodurch minimale Gastemperaturen, die um einen Faktor zwei niedriger liegen, erreicht werden können. Wir untersuchten, welche Eigenschaften der Mini-Halos die Kollapszeit bestimmen, und zeigen, im Gegensatz zu früheren Erwartungen, dass die Masse und die Rotationsenergie wenig bis gar keinen Einfluss auf die Kollaps-Geschwindigkeit haben. Daher vermuten wir, dass der Faktor, der bestimmt, ob ein Kollaps langsam oder schnell verläuft, und damit, ob HD-Kühlung wichtig wird, der Grad der Turbulenz des Gases ist.

Acknowledgements

To be honest, my PhD experience was one of those that made me consider quitting on a regular basis. I am not sure if I enjoyed doing it—I would have continued astronomy the rest of my life if things worked out a little easier. However, I am certain I could not have finished my PhD without the help and encouragement from the following people.

First of all, I would like to express my gratitude to my supervisor, Prof. Ralf Klessen, who offered me an opportunity to work on an interesting topic in Heidelberg, for all the support he has offered me through my PhD. He introduced me to many astronomers, sent me to conferences, thus offering opportunities to interact with many astronomers, and organised many informal meetings for science discussions. He is a friendly group leader interested in many things, which allows many junior members of the group to pursue their scientific interest. I cannot thank enough to Dr. Simon Glover and Dr. Paul Clark, for having lots of scientific discussions and being patient and encouraging throughout. Things have been much more difficult if it were not for Simon's wisdom or Paul's hacking skills. I learnt a lot from stimulating discussions with them. Chapter 4 would not have existed without Paul or Simon.

I am also grateful to Prof. Volker Springel, who have offered me the codes that I have based my scientific work on, and gave me professional pieces of advice. Occasionally I contacted him for help when I felt I was stuck, and always felt smarter after writing to/discussing with him. If I were to work in a leading position in my future job some day, I would like to treat junior members in the group like Volker does his people. I would also like to thank Prof. Matthias Bartelmann, who have offered me valuable pieces of advice especially when I was working on my structure formation paper. He helped me figure out small but important questions in structure formation. He is always encouraging when I drop in his office to discuss something. The same gratitude goes to Prof. Björn Malte Schäfer. I am grateful to Dr. Thomas Greif for offering his expertise in the field of primordial star formation and sharing his experience with the moving mesh code. I also thank Dr. Federico Marinacci for answering my simple questions on the AREPO code. My sincere thanks also goes to Prof. Norbert Christlieb and Prof. Luca Amendola, for being part of my defence committee.

In some respects, I deeply thank my former supervisor, Prof. Naoki Yoshida, for being a characteristic supervisor. I probably could not have made up my mind to 'escape' to Germany to do a PhD if it were not for him. I learnt to maintain sanity and keep struggling even in the most desperate and helpless situations from working with him.

List of publications

Refereed publications

- **Sasaki, Mei**, Clark, Paul C., Springel, Volker, Klessen, Ralf S., Glover, Simon C. O. Statistical properties of dark matter mini-haloes at z >= 15, 2014, Monthly Notices of the Royal Astronomical Society, Volume 442, Issue 3, p.1942-1955

- **Sasaki, Mei**, et al. 2015. The criterion for HD formation in the early universe - in prep.

Conference proceedings

- **Sasaki, Mei**, Clark, Paul C., Klessen, Ralf S., Glover, Simon C. O., Springel, Volker, Yoshida, Naoki. Statistical properties of dark matter mini-halos, 2012, FIRST STARS IV - FROM HAYASHI TO THE FUTURE -. AIP Conference Proceedings, Volume 1480, pp. 409-411

Contents

1 Introduction

Where did we come from? Where are we going? Thanks to the advances in natural sciences, scientists today can do a much better job in answering such fundamental questions than in the past. We have a common understanding that the universe was much smaller in size, hotter, and denser when it was born in a Big Bang about 13.8 Gyrs ago, and that it continues to expand at an increasing rate. We also know that the first generation of stars contributed significantly in changing the simple homogeneous state of the universe at the time of its birth to the more complex and diverse state as it is today.

The goal of this thesis is to make a small advancement in the fields of first star formation and structure formation.

Stars are divided into three populations according to the amount of 'metals', i.e. elements heavier than lithium (Li) they contain: Population I (metal-rich), Population II (metal-poor), and Population III (metal-free). Since metals did not exist immediately after the Big Bang, the first stars to form in the universe were Population III (Pop III) stars. Once the Pop III stars have formed, at the end of their lives, elements synthesised at the centres of the stars were distributed by supernova explosions. Therefore, it is believed that there is a gradual transition from Pop III to Pop II stars. Pop II stars are most often found in the bulge and halo of galaxies. Pop I stars are mostly found in the disks of galaxies. The Sun is an example of a Pop I star.

In this chapter, we will first summarise the key concepts in structure formation. Then we will briefly explain baryonic physics which is relevant for Pop III star formation.

1.1 CDM universe

If we consider the line element ds of the form

$$ds^2 = g_{\mu\nu}dx^\mu dx^\nu, \tag{1.1}$$

under the assumptions of homogeneity and isotropy, we arrive at the below metric (Robertson-Walker metric):

$$ds^2 = -c^2 dt^2 + a^2(t)\left[\frac{dr^2}{1-Kr^2} + r^2(d\theta^2 + \sin^2\theta d\phi^2)\right]. \tag{1.2}$$

The Einstein's equations read

$$R_{\mu\nu} - \frac{1}{2}Rg_{\mu\nu} + \Lambda g_{\mu\nu} = \frac{8\pi G}{c^4}T_{\mu\nu}, \tag{1.3}$$

where $R_{\mu\nu}$ is the Ricci tensor, R $(= g^{\mu\nu}R_{\mu\nu})$ is the Ricci scalar, Λ is the cosmological constant, and $T_{\mu\nu}$ is the energy-momentum tensor $(T_{00} = \rho c^2, T_{ij} = p\delta_{ij}$ where $1 \leq i, j \leq 3)$. Substituting this metric (equation (1.2)) in the Einstein equations (equation (1.3)) we obtain Friedman equation,

$$\frac{H(a)}{H_0} = \sqrt{\frac{\Omega_r}{a^4} + \frac{\Omega_m}{a^3} + \frac{\Omega_K}{a^2} + \Omega_\Lambda}$$

$$H(a) = \dot{a}/a \tag{1.4}$$

where $\Omega_K = -Kc^2/H_0^2$, $\Omega_\Lambda = \frac{\Lambda c^2}{8\pi G}/\rho_{\mathrm{cr},0}$, and Ω_m (Ω_r) denotes the density of matter (radiation) scaled by critical density of the universe at present, $\rho_{\mathrm{cr},0} = 3H_0^2/8\pi G$. This equation tells us the scale factor a at a given time. It is used to convert scale factor and physical time inside our cosmological simulations. The phases usually studied by N-body or hydrodynamical simulations is either matter-dominated or cosmological-constant-dominated era (meaning either the term Ω_m/a^3 or the term Ω_Λ is dominant in the rhs of equation (1.4)), therefore, the radiation and curvature terms are actually not included in the code. The precise values of the cosmological parameters that appear in these equations are known, for example, by measuring the height and locations of peaks in the angular power spectrum of anisotropies in cosmic microwave background (Komatsu et al., 2011). We know that a large portion of the matter component of Friedmann equations is cold dark matter (CDM), meaning that the velocity dispersions of the dark matter particles at the time they became non-relativistic was not big enough to erase the density perturbations already present at that time.

1.2 Equations that govern the density peak evolution in the universe

If we rewrite the continuity equation and equation of motion in comoving coordinates, it reads:

$$\frac{\partial \rho}{\partial t} + 3H\rho + \nabla \cdot (\rho\boldsymbol{u}) = 0 \tag{1.5}$$

$$\frac{\partial \boldsymbol{u}}{\partial t} + 2H\boldsymbol{u} + (\boldsymbol{u} \cdot \nabla)\boldsymbol{u} = -\frac{1}{a^2}\nabla\left(\phi + \frac{1}{2}a\ddot{a}x^2\right) - \frac{\nabla p}{a^2\rho}, \tag{1.6}$$

where $\boldsymbol{r}$ is the physical coordinates, $\boldsymbol{x} = \boldsymbol{r}/a$ is comoving coordinates, and $\boldsymbol{u} = \dot{\boldsymbol{x}}$ is the velocity in comoving coordinates, ρ is the density, p is the pressure, ϕ is the gravitational potential. The gravitational potential ϕ is given by Poisson equation, which is expressed in the following equation when differentiated in proper coordinates,

$$\triangle \phi = 4\pi G\rho. \tag{1.7}$$

There is no general analytical solution for this equation. When the density perturbations are still small, it is possible to perturb equations (1.5) and (1.6) and keep only linear terms to follow the evolution of density peaks. Of course, for the dark matter

component, the last term in equation (1.6) is not present. Let us define density perturbation by $\delta(\boldsymbol{x}) \equiv (\rho(\boldsymbol{x}) - \bar{\rho})/\bar{\rho}$ where $\bar{\rho}$ is the background density at a given time. Then, in the linear regime, if we assume $\delta(\boldsymbol{x}) \propto \exp(i\boldsymbol{k} \cdot \boldsymbol{x})$, the evolution of $\delta(\boldsymbol{x})$ is described by

$$\frac{\partial^2 \delta}{\partial t^2} + 2H \frac{\partial \delta}{\partial t} - \left(4\pi G\bar{\rho} - \frac{c_s^2 k^2}{a^2} \right) \delta = 0. \tag{1.8}$$

This shows that the modes with $4\pi G\bar{\rho} - c_s^2 k^2/a^2 > 0$ keeps growing in the presence of a small initial positive perturbation. This corresponds to density perturbations with wavelength $\lambda \equiv 2\pi/k > c_s/a\sqrt{\pi/G\bar{\rho}}$, or in proper wavelength, $\lambda_p > c_s\sqrt{\pi/G\bar{\rho}}$ (the Jeans length, see also Section 1.9). However, this tactics would not work when the density perturbations have grown too big.

1.3 Power spectrum, transfer function, initial conditions

The power spectrum for density perturbations is given by

$$P(k) = \langle |\delta_{\boldsymbol{k}}|^2 \rangle, \tag{1.9}$$

where $\delta_{\boldsymbol{k}}$ is the Fourier transformation of density perturbation $\delta(\boldsymbol{x})$. In fact, the power spectrum is a variable with dimensions of (length)^3, and to evaluate its value, the non-dimensional quantity

$$\Delta^2(k) \equiv \frac{k^3 P(k)}{2\pi^2} \tag{1.10}$$

is used. We can write $d^3 k P(k)/(2\pi)^3 = d\ln k \Delta^2(k)$ assuming isotropy and thus replacing the integral $d^3 k$ by $4\pi k^2 dk$. Therefore, equation (1.10) shows the power present in a logarithmic bin.

The initial conditions for our cosmological simulations are generated in the following way:

First the linear power spectrum is given by

$$P(k) = A\, k\, T(k)^2, \tag{1.11}$$

where A is the normalisation factor, which depends on both cosmological parameters used and the redshift the power spectrum is calculated. $T(k)$ gives the amplitude of density perturbations relative to the largest scales (e.g. normalised such that $T(k) \to 1$ as $k \to 0$). This transfer function has the approximate form of

$$T(k) \begin{cases} 1\ (k \ll k_\mathrm{H}(t_\mathrm{eq})) \\ k^{-2}\ (k \gg k_\mathrm{H}(t_\mathrm{eq})) \end{cases}, \tag{1.12}$$

where $k_\mathrm{H}(t_\mathrm{eq})$ denotes the wavenumber that corresponds to the Hubble radius ($r_\mathrm{H} \equiv c/H$) at the time of matter-radiation equality (meaning when $\Omega_r/a^4 = \Omega_m/a^3$ in equation (1.4)). For the density perturbations that 'enter the horizon' (i.e. wavelength
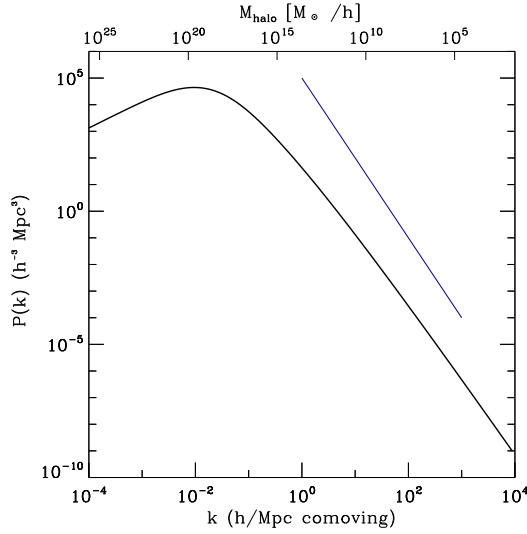
Figure 1.1: The linearly extrapolated power spectrum of dark matter at $z = 0$ for the cosmological parameters adopted in Sasaki et al. (2014) and in Chapter 2. The critical slope of k^{-3} is shown with dark blue line.

becomes equal to the Hubble radius) in the radiation-dominated era, the density perturbations stop growing. This functional form accounts for the fact that the modes that enter the horizon earlier (smaller modes) are more suppressed. As a result of this k-dependence in the transfer function, the power spectrum of density perturbations have a turnover (see Fig. 1.1).

The exact functional form of $T(k)$ often used are,

$$T(k) = \left\{ 1 + \left[ak + (bk)^{3/2} + (ck)^2 \right]^{\nu} \right\}^{-1/\nu}, \tag{1.13}$$

where

$$a = 6.4(\Omega_0 h^2)^{-1} \tag{1.14}$$
$$b = 3.0(\Omega_0 h^2)^{-1} \tag{1.15}$$
$$c = 1.7(\Omega_0 h^2)^{-1} \tag{1.16}$$
$$\nu = 1.13, \tag{1.17}$$

as derived by Bond and Efstathiou (1984) and

$$T(k) = T_0(q) = \frac{L_0}{L_0 + C_0 q^2}, \tag{1.18}$$

with $L_0(q)$ and $C_0(q)$ of the form

$$L_0(q) = \ln(2e + 1.8q), \tag{1.19}$$
$$C_0(q) = 14.2 + \frac{731}{1 + 62.5q}, \tag{1.20}$$

where $q = k/h\text{Mpc}^{-1}\Theta_{2.7}^2\Gamma$, with $\Gamma = \Omega_0 h$ and $\Theta_{2.7} = T_{\text{CMB}}/2.7$ [K] as derived by Eisenstein and Hu (1998) (note that we followed the notation of the original paper and used Ω_0 instead of Ω_m here). The latter is used for generating initial conditions for simulations presented in Chapter 2. For the initial condition generator we used, it is also possible to adopt an arbitrary form of transfer function that is provided by the user.

Then by applying Fourier transform, it is possible to get particle dispositions in real space that has a Power spectrum $P(k)$.

The transfer functions that are used here are valid when the density perturbations are still small ($\delta(\boldsymbol{x}) \sim 1$). However, we need different methods to probe the densest regions in the universe at later times. Therefore, this prescription is widely used to generate initial conditions (particle distributions for N-body simulations) in the early universe when the density is uniform. We find the evolution of dense structures later in cosmic history by numerically integrating the equation of motion over time.

1.4 Spherical collapse model

The simplest model to explain formation of dense structures is the spherical collapse model. We here consider time evolution of spherically symmetric density perturbations with radius $R(t)$ that contains total mass of M (= const.)

$$\frac{d^2R}{dt^2} = -\frac{GM}{R^2}. \tag{1.21}$$

Time integrating equation (1.21), we obtain

$$\left(\frac{dR}{dt}\right)^2 = \frac{2GM}{R} + 2E, \tag{1.22}$$

where E is an integration constant. We see from equation (1.22) that the sign of E decides on the fate of this sphere. If $E > 0$, then the rhs of equation (1.22) is always > 0, and the radius of sphere will monotonically increase (non-bound solution). If $E < 0$, then initially the rhs of equation (1.22) is > 0, however, at $R = -\frac{GM}{E}$, becomes equal to 0, and the expansion of $R(t)$ stops, and after that, the sphere starts to fall inside (bound solution). Therefore, depending on the initial state, there are two different kinds of regions inside the universe. Those with $E > 0$ that continue to expand, and those with $E < 0$ that stop to expand and starts to fall back at some point.

The solutions to these equations are given in the form

$$\begin{cases} R = A^2(1 - \cos\theta) \\ t = \frac{A^3}{\sqrt{GM}}(\theta - \sin\theta) \end{cases} (\text{E} < 0) \tag{1.23}$$

$$\begin{cases} R = A^2(\cosh\theta - 1) \\ t = \frac{A^3}{\sqrt{GM}}(\sinh\theta - \theta) \end{cases} (\text{E} > 0) \tag{1.24}$$

where A is an integration constant and θ is the intervening variable.

For the bound solution, the maximum value in $R(t)$ is achieved (the sphere stops expanding) when $\theta = \pi$. According to equation (1.23) this is when

$$t_{\text{turn}} = \frac{\pi A^3}{\sqrt{GM}}, \ R_{\text{turn}} = 2A^2 \tag{1.25}$$

and the sphere collapses to a point when $\theta = 2\pi$

$$t_{\text{coll}} = \frac{2\pi A^3}{\sqrt{GM}}, \ R_{\text{coll}} = 0. \tag{1.26}$$

From the above equation, if we adopt an Einstein-de Sitter universe ($\Omega_m = 1, \Omega_r = \Omega_\Lambda = \Omega_K = 0$ in equation (1.4)) for simplicity, then the background density is given by $\bar{\rho} = 1/(6\pi G t^2)$. Substituting the density inside the sphere, $\rho = M/(4\pi R^3/3)$, density perturbations ($= \rho/\bar{\rho} - 1$) can be formulated as

$$\delta(t) = \frac{9GMt^2}{2R^3} - 1 = \begin{cases} \frac{9}{2}\frac{(\theta - \sin\theta)^2}{(1 - \cos\theta)^3} - 1 (\text{E} < 0) \\ \frac{9}{2}\frac{(\sinh\theta - \theta)^2}{(\cosh\theta - 1)^3} - 1 (\text{E} > 0) \end{cases} \tag{1.27}$$

If we consider that the sphere virializes between the turn around point and the collapse point, then the kinetic energy and potential energy at this virialization satisfies

$$2K_{\text{vir}} + U_{\text{vir}} = 0 \, (\text{virial equilibrium}) \tag{1.28}$$

and

$$K_{\text{vir}} + U_{\text{vir}} = \frac{3}{5}G\frac{M^2}{R_{\text{turn}}} \, (\text{energy conservation}). \tag{1.29}$$

We assumed constant density inside the sphere in deriving equation (1.29). Thus we obtain

$$U_{\text{vir}} = \frac{6}{5}G\frac{M^2}{R_{\text{turn}}} = \frac{3}{5}G\frac{M^2}{R_{\text{turn}}/2}. \tag{1.30}$$

Therefore, when virialized, the radius of the sphere is $R_{\text{vir}} = R_{\text{turn}}/2 = A^2$, when $\theta = 3\pi/2$. The time required for the mass inside the sphere to virialize is the order of t_{coll}, therefore, the density perturbation at this point is

$$\delta_{\text{vir}} = \frac{M/(4\pi R_{\text{vir}}^3/3)}{\bar{\rho}(t_{\text{coll}})} - 1 = 18\pi^2 - 1 \simeq 177. \tag{1.31}$$

In the spherical model, gravitationally collapsed regions have density contrast of ~ 177 compared to the mean background density. Even if we adopt different cosmologies, this resulting value changes little (Peebles, 1980). Inspired by this spherical collapse model, the overdensity of 200 is widely used as a threshold to identify virialized regions in three-dimensional collisionless simulations intended to follow the structure

formation in a cosmological context. ρ_{200} (R_{200}) is often used to represent the density (radius) of such regions.

Let us look at the spherical collapse model when the density perturbations are still small and compare it with linear theory. By expanding equation (1.27) in terms of θ, we obtain

$$\delta = \frac{3}{20}\theta^2 + \mathcal{O}(\theta^4) \tag{1.32}$$

$$t = \frac{A^3}{6\sqrt{GM}}\theta^3 + \mathcal{O}(\theta^5) \tag{1.33}$$

To lowest order, $\delta \propto t^{2/3}$. If we note linear density perturbation by δ_{L}, we can write

$$\delta_{\mathrm{L}}(t) = \frac{3}{20}\left(\frac{6\sqrt{GM}}{A^3}t\right)^{2/3}. \tag{1.34}$$

To compare values of δ and δ_{L}, the linear density perturbations at the point of collapse is

$$\delta_{\mathrm{L}}(t_{\mathrm{coll}}) = \frac{3(12\pi)^{2/3}}{20} \simeq 1.69. \tag{1.35}$$

The Press-Schechter theory explained in the next section is based on the idea that once the linear density perturbations reach the value of 1.69, the structure has formed.

1.5 Press-Schechter mass functions

We hereby describe a popular analytical model to predict the number of objects with certain mass (Press and Schechter, 1974).

In this model, the critical value of density perturbations to form astronomical objects are assumed to be $\delta_c \simeq 1.69$, which is taken from a spherical collapse model (see Section 1.4).

If we assume that the density perturbations follow a Gaussian distribution, then the probability distribution function for the density perturbations averaged over mass of M is expressed as

$$P(\delta_M)d\delta_M = \frac{1}{\sqrt{2\pi\delta^2(M)}}\exp\left(-\frac{\delta_M^2}{2\sigma^2(M)}\right). \tag{1.36}$$

The assumption of Gaussianity is reasonable since recent measurements in the cosmic microwave background suggest very low non-Gaussianity (Planck Collaboration et al., 2014) and most simple form of inflation theory predicts Gaussian density perturbations. Even if the density perturbations are not exactly Gaussian, we can consider them as sums of a large number of different modes in k-space that are independent of each other, which, by the central limit theorem, suggests that the density perturbations in real space approach asymptotically to a Gaussian distribution.

Therefore, the fraction that exceeds the critical value when averaged over a region with mass M is

$$P_{>\delta_c}(M) = \int_{\delta_c}^{\infty} P(\delta_M)d\delta_M = \frac{1}{\sqrt{2\pi}} \int_{\delta_c/\sigma(M)}^{\infty} e^{-x^2/2}dx, \qquad (1.37)$$

where $\sigma(M)$ is the overdensity in a sphere of mass M and given by

$$\sigma(M) \equiv \int d\boldsymbol{x'}\delta(\boldsymbol{x'})W_R(\boldsymbol{x}-\boldsymbol{x'}), \qquad (1.38)$$

where W_R and R is defined by

$$W_R(\boldsymbol{x}) = \left\{ \begin{array}{l} 1 \ (|\boldsymbol{x}| < R) \\ 0 \ (|\boldsymbol{x}| > R) \end{array} \right. , \quad M = \frac{4\pi}{3}R^3\bar{\rho}. \qquad (1.39)$$

If we represent the number of objects with masses between M and $M + dM$ per unit volume by $n(M)dM$, and multiply the rhs by a factor of 2 to account for mass that reside in under-dense regions, we arrive at

$$n(M)MdM = 2\bar{\rho}\left|\frac{dP_{>\delta_c}}{dM}\right|dM. \qquad (1.40)$$

Combining equations (1.37) and (1.40), we obtain the following equation:

$$n(M) = \sqrt{\frac{2}{\pi}}\frac{\bar{\rho}}{M^2}\left|\frac{d\ln\sigma(M)}{d\ln M}\right|\frac{\delta_c}{\sigma(M)}\exp\left(-\frac{\delta_c^2}{2\sigma^2(M)}\right). \qquad (1.41)$$

This is known to be in good match with the results of numerical simulations for a broad mass range. For the mass function at the smallest mass ranges, see the plot in Chapter 2.

1.6 N-body simulations

N-body simulations are the primary tool to investigate the formation of gravitationally bound objects in the universe, once the density perturbations have become so large that the perturbation theory does not work. (See Section 1.3 for one definition when the density perturbation is large.) In this approach, by using large number of particles, the acceleration due to gravitational force is obtained for each particle by adding up contributions from all other particles. Perhaps this is conceptually the most straightforward way to follow the evolution of collisionless self-gravitating systems and thus has a long history. There are in principle other ways such as solving the Boltzmann equation in phase space (Yoshikawa et al., 2013). Note this is an expensive operation that scales as $\mathcal{O}(N^6)$(!) for 3D case.

In modelling the smooth underlying dark matter distribution with a finite number of particles in the simulation, in order to prevent artificial two-body interactions, softening length ϵ is widely used in the field to smooth gravitational forces when two

particles become too close to each other. Suppose we are calculating the gravitational force between i-th particle and j-th particle, the gravitational force proportional to $\frac{1}{|\boldsymbol{r}_i-\boldsymbol{r}_j|^2}$ is modified to $\frac{1}{|\boldsymbol{r}_i-\boldsymbol{r}_j|^2+\epsilon^2}$, where $\boldsymbol{r}_i$ and $\boldsymbol{r}_j$ represent the positions of the particles in proper coordinates. ϵ is typically set to a few percent of the mean particle separation in the simulation box.

In order to calculate gravitational forces that work on particles, it is necessary to sum up contributions from all other particles for each timestep. This is an $\mathcal{O}(N^2)$ calculation, and can become increasingly time-consuming as the number of particles increases. The astrophysical community has developed several ways to solve this problem. Calculating the gravitational force is much more expensive in terms of computational time than in any other operations in many-body simulations. One solution is to build a special purpose computer dedicated to accelerate this operation (Makino et al., 1997). Another way is to reduce the cost of force calculation by grouping particles far away from the particle on which we are to calculate the gravitational forces (for example, tree method; originally from Barnes and Hut 1986). This method scales as $\mathcal{O}(N\log N)$. However, even with special purpose computer, the maximum number of particles we can plausibly solve by direct summation is $\sim 10^6$ (Makino, 2002). Therefore in modern structure formation simulations, approximate methods to reduce the cost of force calculation is essential.

1.7 Relaxation time

Following the discussions of Binney and Tremaine (2008) and lecture slides for an astrophysical school[1], let us consider a system that consists of N particles ('stars') with mass m, and estimate the time it takes for a star for its velocity to be changed significantly by encounters with other stars. Here we would like to estimate the timescale at which we start to see numerical artifacts resulting from the discretisation of the underlying smooth dark matter density field by finite number of particles in our N-body simulations. We would like to study the change of velocity of a point mass ('subject star') with uniform mass m by an encounter with another point mass ('field star'). If we assume that the subject star travels along a straight trajectory while passing along the field star with speed v, impact parameter b, that the position of the field star does not change throughout this encounter, and that the change in velocity is small ($|\delta\boldsymbol{v}|/v \ll 1$) (see how we defined the coordinates in Fig. 1.2), then the perpendicular component of the force on the subject star can be written as

$$F_\perp = \frac{Gm^2}{b^2+x^2}\cos\theta = \frac{Gm^2 b}{(b^2+x^2)^{3/2}} = \frac{Gm^2}{b^2}\left[1+(vt/b)^2\right]^{-3/2}. \qquad (1.42)$$

The parallel component of force vanishes when integrated over time.

By time integrating this force (setting the origin of time to the moment of closest

---

[1]
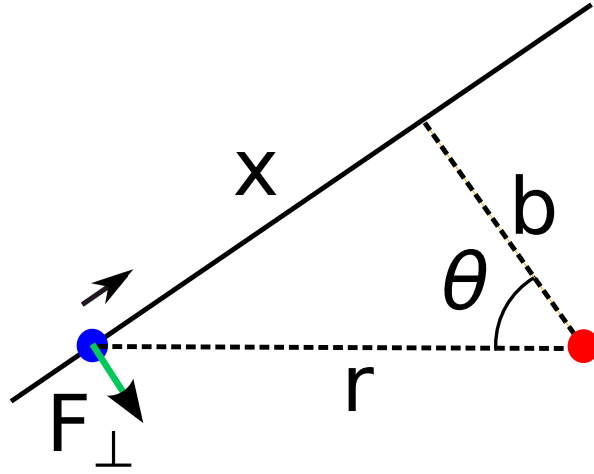
Figure 1.2: Coordinates adopted in calculating the velocity change of the subject star. The subject star is represented with a blue circle, the field star with a red circle. The trajectory of the subject star is demonstrated with a solid line here.

approach of two stars), the change in velocity is

$$
\begin{aligned}
\delta v &= \frac{1}{m} \int_{-\infty}^{\infty} dt F_{\perp} = \frac{GM}{b^2} \int_{-\infty}^{\infty} \frac{dt}{[1 + (vt/b)^2]^{3/2}} \\
&= \frac{Gm}{bv} \int_{-\infty}^{\infty} \frac{ds}{(1 + s^2)^{3/2}} = \frac{2Gm}{bv}.
\end{aligned}
\tag{1.43}
$$

The assumption that the change in velocity is small breaks down when $\delta v \simeq v$ (*), namely, when $b \lesssim 2Gm/v^2$. The typical speed v of field star is given by

$$
v^2 \approx \frac{GNm}{R}.
\tag{1.44}
$$

Substituting equation (1.44) to expression (*), we find that the minimum value allowed for the impact parameter is $b_{\min} = 2R/N$.

Suppose N stars are located in a disk of radius R. The surface density of stars is $N/(\pi R^2)$, and therefore the expected number of encounters for this subject star per crossing with impact parameter in the range b and $b + db$ is

$$
dn = \frac{N}{\pi R^2} 2\pi b db = \frac{2N}{R^2} b db
\tag{1.45}
$$

By adding up different encounters, after one crossing, the change in mean-square velocity becomes

$$
(\Delta v)^2 = \int \left(\frac{2Gm}{bv} \right) dn = 8N \frac{Gm^2}{Rv} \int \frac{db}{b} = 8N \frac{Gm^2}{Rv} \ln \Lambda,
\tag{1.46}
$$

where

$$\ln \Lambda \equiv \ln \left(\frac{b_{\max}}{b_{\min}} \right). \tag{1.47}$$

Using equation (1.44) to eliminate R in equation (1.46), we get

$$\frac{(\Delta v)^2}{v^2} \approx \frac{8 \ln \Lambda}{N} \tag{1.48}$$

Since equation (1.48) gives the change in velocity after one crossing, the number of crossings n_{relax} that is required for the velocity of subject star to change by of order itself is

$$n_{\mathrm{relax}} \simeq \frac{N}{8 \ln \Lambda}. \tag{1.49}$$

The relaxation time is defined as $t_{\mathrm{relax}} = n_{\mathrm{relax}} t_{\mathrm{cross}}$, where $t_{\mathrm{cross}} = R/v$, therefore,

$$t_{\mathrm{relax}} = \frac{N}{8 \ln \Lambda} t_{\mathrm{cross}}. \tag{1.50}$$

Now if we evaluate the minimum and maximum value for the impact parameter,

$$b_{\max} = R, \tag{1.51}$$

$$b_{\min} = \frac{2R}{N}, \tag{1.52}$$

$$\Lambda = \ln \frac{R}{2R/N} = \ln \left(\frac{N}{2} \right), \tag{1.53}$$

thus we obtain

$$t_{\mathrm{relax}} \simeq \frac{N}{8 \ln N} t_{\mathrm{cross}}. \tag{1.54}$$

If we replace stars by dark matter particles, this equation can be used to evaluate the relaxation time for dark matter haloes in structure formation simulations. Here we consider the region that is factor of 200 denser than the critical density (this is from analogy with the spherical collapse model, see Section 1.4 for an explanation of why regions ~ 200 times denser than the background density is relevant). It follows from

$$M_{200} = \frac{4\pi}{3} 200 \rho_{\mathrm{crit}} R_{200}^3, \tag{1.55}$$

$$v_{200} = \sqrt{\frac{GM_{200}}{R_{200}}}, \tag{1.56}$$

and

$$\rho_{\mathrm{crit}} = \frac{3H^2}{8\pi G} \tag{1.57}$$

11

that

$$t_{\text{cross}} \simeq \frac{R_{200}}{v_{200}} \sim \frac{1}{2H}. \tag{1.58}$$

Plugging equation (1.58) into equation (1.54) yields

$$t_{\text{relax}} \simeq \frac{N}{16 \ln N} \left(\frac{1}{H} \right), \tag{1.59}$$

which shows, for systems that is reasonably well resolved ($N > 100$), relaxation time is longer than the age of the universe ($\sim \frac{1}{H}$), and that the output of our collisionless simulations are not just artifacts resulting from two-body interactions.

1.8 Identification of structure in cosmological simulations

In a simulation using collisionless particles to represent dark matter density, the method to identify structures that have formed inside the simulation domain can be problematic. Different groups have adopted different methods and this is one of the factors that make comparison of the works from different groups difficult. Most of the structure-finding algorithms adopted today are descendants of either of the two methods: the friends-of-friends (FOF) method (Davis et al., 1985) and the spherical-overdensity (SO) method (Lacey and Cole, 1994). Methods based on SO first identify density peaks, and then grow shells around these peaks until the density drops under some predefined lower limit. This limit is usually taken from the spherical collapse model. Methods based on FOF tries to link together particles that are located close to each other (either in 3D space or in 6D phase-space). In the work presented in Chapter 2, an additional algorithm to spot dense regions inside FOF haloes is used (SUBFIND). A summary of various different approaches to identify structures is given in Knebe et al. (2013). They find that when comparing properties of corresponding objects identified by different algorithms, directly measurable properties such as position, bulk velocity, maximum velocity have scatter of only a few percent, while derived properties such as shape or spin have a much larger scatter. For an example on how halo identification affects the value of spin parameter, compare Fig. 2.3 with A.5. Measuring the shape of haloes (i.e. fitting the particle distribution with an ellipsoid) is difficult, because the shape of haloes we find in structure formation simulations are not exactly ellipsoids. Instead, their shapes change as a function of radius (we checked that for the data analysed in Chapter 2, the inner parts of the halo are more spherical).

1.9 Condition for star formation

In Fig. 1.3, the cooling functions for various elements in atomic gas with solar composition is shown. In the early universe, when the first generation of stars form in a region where there was no preceding generations of stars, elements heavier than Li are absent. Therefore most of the elements relevant for cooling in the local interstellar medium (ISM) (e.g. C^+, Si^+, Fe^+, O, S^+) are absent. Cooling due to atomic hydrogen
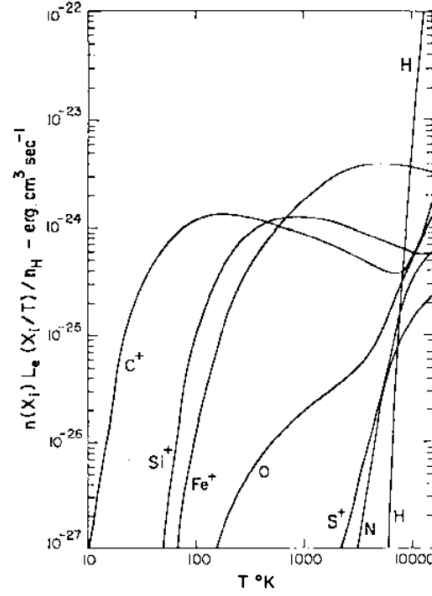
Figure 1.3: Cooling functions of various elements weighted by their abundance. Taken from Fig.1 in Dalgarno and McCray (1972)
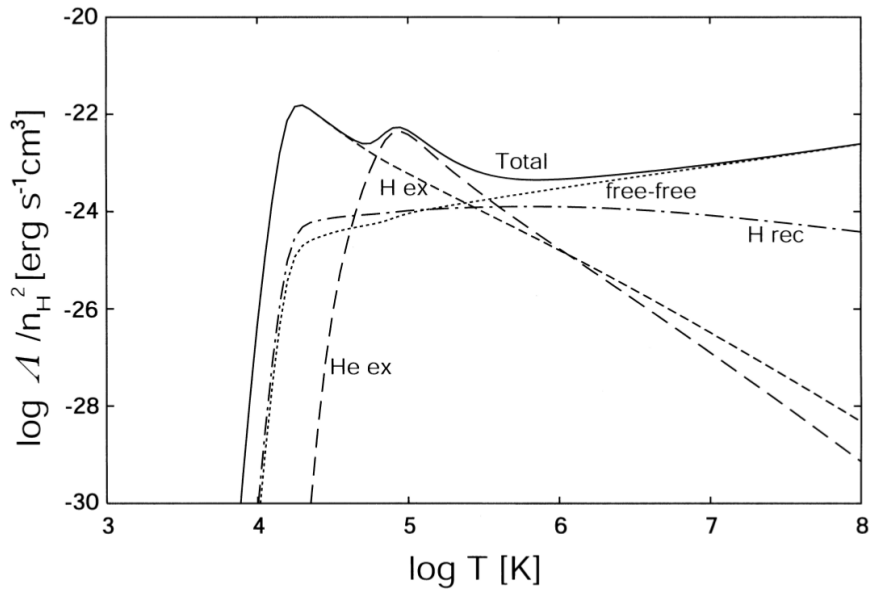
Figure 1.4: Cooling function of H atom and He atom in primordial gas. Taken from Fig.1 in Nishi (2002)

and atomic helium is effective only at $T > 10^4$ K (Nishi, 2002, and Fig. 1.4). In such a case, H_2 line cooling is the primary physical process that lowers the temperatures of gas to $T \ll 10^4$ K.

In order for the gas to start collapsing inside the centres of the dark matter haloes, several conditions have to be met.

In Section 1.2 we introduced the Jeans length in a cosmological context, however, the formulation is the same even in proper coordinates. Thus, the minimum gas mass in haloes required to start a run-away collapse (the Jeans mass) is:

$$M_J \equiv \frac{4\pi}{3}\bar{\rho}\left(\frac{\lambda_J}{2}\right)^3, \tag{1.60}$$

where

$$\lambda_J = c_s\sqrt{\frac{\pi}{G\bar{\rho}}}. \tag{1.61}$$

Otherwise, the collapse will be halted by the internal pressure.

For $T = 200$ K, $n = 10^4$ cm^{-3}, the Jeans mass is > 100 $M_\odot$. The clump with this mass may fragment into smaller pieces later in the collapse, so this mass cannot be directly associated with the masses of resulting stars.

The criterion $t_{\text{cool}} = \varepsilon/\dot{\varepsilon} \sim \frac{3}{2}nkT/\Lambda(T) < t_{\text{ff}} \sim \frac{1}{\sqrt{G\bar{\rho}}}, t_H \equiv a/\dot{a}$ also has to be met (Tegmark et al., 1997), where T is the temperature of gas, Λ represents cooling function, and ε represents the thermal energy. This gives a minimum mass of the halo for primordial gas to collapse inside it. The exact lower mass depends on the reaction rates adopted. However, by assuming the virial temperature of primordial gas to be 1000 K, Glover (2013) calculates the critical halo mass as:

$$M_{\text{crit}} \simeq 6 \times 10^5 h^{-1}\left(\frac{\mu}{1.2}\right)^{-3/2}\Omega_m^{-1/2}\left(\frac{1+z}{10}\right)^{-3/2}. \tag{1.62}$$

If this condition is not met, the gas collapse is either prevented by thermal pressure or the expansion of the universe. Yoshida et al. (2003) has shown this explicitly with direct hydrodynamical simulations in a cosmological context. The latter also suggests that dynamical heating from mergers could delay the initial collapse of primordial gas.

1.10 Pop III - Pop II transition

The transition in the characteristic mass for different populations of stars can be understood to lowest order by the argument of Jeans masses. As heavy elements produced inside the stars and dust that is formed out of these metals are distributed to the interstellar medium, there are more coolants and the Jeans masses become lower.

There are two main theories about the main driver for transition from Pop III to Pop II stars. There are works that argue C^+ and O produced as a result of earlier
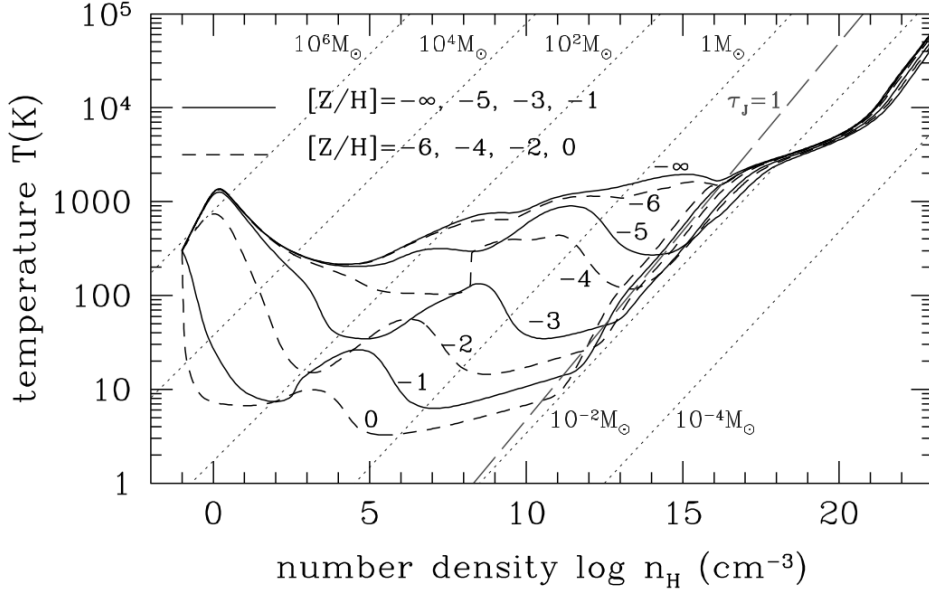
Figure 1.5: Thermal evolution of gas with different metallicities. The second trough in temperatures is induced by dust cooling. Taken from Fig.1 in Omukai (2000)

generation of stars lowers the characteristic masses of Pop II stars (Bromm et al., 2001; Bromm and Loeb, 2003; Santoro and Shull, 2006). Theoretically, there is a concept of 'critical metallicity', Z_{crit}, above which the mode of star formation changes from Pop III stars to Pop II stars. In this theory, the critical metallicity Z_{crit} is found to be $\sim 10^{-3} Z_{\odot}$. On the other hand, Omukai (2000) and Schneider et al. (2003) emphasises the importance of dust, which could be produced from supernova explosions of the first stars (Todini and Ferrara, 2001; Nozawa et al., 2003). They followed the thermal evolution of gas with different metallicities and demonstrated that the dust grains are mostly responsible for the fragmentation which is taking place in the enriched gas (see Fig. 1.5). Based on works of Clark et al. (2008), Dopcke et al. (2011, 2013) have improved on the treatment of dust and found formation of low-mass stars. For this dust cooling scenario, $Z_{crit} = 10^{-6} - 10^{-4} Z_{\odot}$ is considered to be capable of changing the characteristic mass of stars.

1.11 Reactions involving H_2 in the primordial gas

As discussed in Section 1.9, H_2 plays an important role in the cooling of the metal-free gas. In primordial gas, the chemical reactions that is relevant for the formation of H_2 at densities higher than $\sim 10^8$ cm^{-3} is

$$H + H + H \rightarrow H_2 + H, \tag{1.63}$$

as can be seen from the fact that the speed at which this reaction proceeds increases rapidly as density increases (proportional to the cube of number density of hydrogen atoms).

Other important channels in which H_2 forms at lower densities are

$$\begin{align}
H + e^- &\rightarrow H^- + \gamma \tag{1.64} \\
H^- + H &\rightarrow H_2 + e^- \tag{1.65}
\end{align}$$

and

$$\begin{align}
H + H^+ &\rightarrow H_2^+ + \gamma \tag{1.66} \\
H_2^+ + H &\rightarrow H_2 + H^+. \tag{1.67}
\end{align}$$

The processes presented here are less efficient than H_2 formation in the local interstellar medium, where H_2 molecules typically form on dust grains. In the absence of dust grains, $H + H \rightarrow H_2 + \gamma$ is an inefficient process since H_2 molecules cannot radiate away excess energy because they do not possess a dipole moment.

1.12 Protostellar collapse

The capital letters in square brackets in this paragraph represent different points in the ρ-T diagram demonstrated in Fig. 1.6 and correspond to different physical processes. At densities $< 1\,\mathrm{cm}^{-3}$, compressional heating is more efficient than H_2 line cooling, so the temperature increases [A]. After that, the temperature decreases due to H_2 line cooling (there is also small amount of contribution from HD) [B]. The temperature reaches the minimum at $\sim 10^4\,\mathrm{cm}^{-3}$. This is because at $n \sim 10^4\,\mathrm{cm}^{-3}$ the energy levels of H_2 that are relevant for cooling reach local thermal equilibrium (LTE)[C]. It means each energy level is populated according to its local thermal equilibrium value which depends only on temperature and the cooling rate no longer scales as $\propto n^2$ and only as $\propto n$. According to reaction (1.63), the fraction of hydrogen molecules starts to increase rapidly at $n \sim 10^{10}\,\mathrm{cm}^{-3}$ from 10^{-3} to unity. At $n \sim 10^{10}$–$10^{12}\,\mathrm{cm}^{-3}$, H_2 cooling starts to become optically thick [E]. Collisionally induced emission/absorption becomes important [F]. As the temperature rises, H_2 starts to dissociate at densities around $\sim 10^{20}\,\mathrm{cm}^{-3}$ [G].

First Omukai and Nishi (1998) in one-dimensional calculations and then Yoshida et al. (2008) in three-dimensions have demonstrated that from primordial gas, protostars of size ~ 0.1 AU form.

1.13 Accretion phase

The Jeans mass gives an estimate of the protostar mass. However, the final mass of stars is determined by the accretion phase that follows this initial collapse. By dimensional analysis, we find that the accretion rate $\dot{M}_\mathrm{acc} \sim M_\mathrm{J}/t_\mathrm{ff} \sim c_s^3/G$. Therefore, the mass accretion is expected to be higher during Pop III star formation, where the temperature remains higher than during present day star formation.
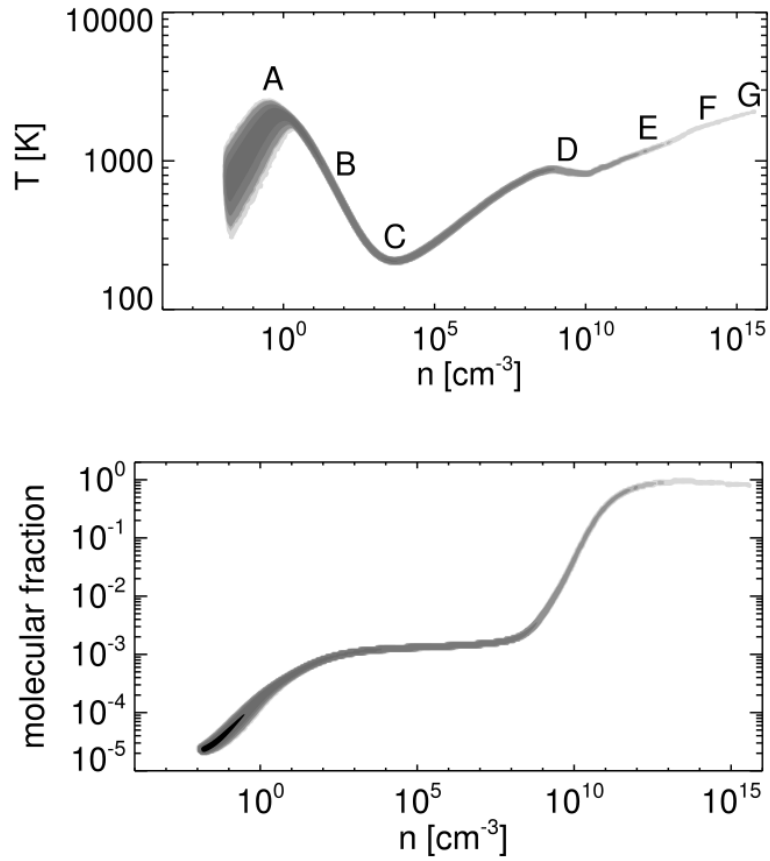
Figure 1.6: Temperature and molecular fraction as a function of number density. Taken from Fig. 3 in Yoshida et al. (2006)

As shown in Fig. 1.7, what influences Pop III stars have on the surrounding ISM is different depending on their final mass. Here, 'final mass' refers to the mass of the star when it has stopped accreting matter. Note that this 'final mass' is referred to as 'initial mass' in Heger and Woosley (2002) and in Fig. 1.7, meaning the mass of the star before it undergoes subsequent stages of evolution.

Stars with final mass ('initial mass' according to Heger and Woosley 2002) $M < 10 \, \mathrm{M_\odot}$ result in white dwarf, those in the mass range $10 \, \mathrm{M_\odot} < M < 25 \, \mathrm{M_\odot}$ explode as supernovae and results in neutron stars, those in the mass range $25 \mathrm{M_\odot} < M < 100 \mathrm{M_\odot}$ explode as supernovae and result in black holes. For those with mass $M > 100 \, \mathrm{M_\odot}$, first the pulsational pair instability destroys the outer layers of the stars, then they end up as black holes. Stars in the mass range $140 \, \mathrm{M_\odot} < M < 260 \, \mathrm{M_\odot}$ end their lives as pair instability supernovae, and nothing is left behind. In the cases of stars with mass $M > 260 \, \mathrm{M_\odot}$, after pair instability takes place, the stars end up in black holes. Therefore, knowing the final mass of Population III stars is the ultimate goal for the research on Population III stars. This is still under investigation today.

Early works on the evolution of protostars include Stahler et al. (1986b), Stahler et al. (1986a), Omukai and Palla (2001), Omukai and Palla (2003). They solved stellar structure equations by assuming a constant accretion onto the hydrostatic core. Their main finding is that there is a critical mass accretion value $\dot{M}_{\mathrm{crit}} \sim 4 \times 10^{-3} \, \mathrm{M_\odot \, yr^{-1}}$, above which the mass accretion is stopped shortly after.

Some authors have made use of sink particles to study the mass accretion onto Pop III stars (Bromm and Loeb, 2004; Clark et al., 2008; Stacy et al., 2010; Smith et al., 2011). Sink particles are point masses to approximate mass in regions within a predetermined radius. Sink particle technique prevents timesteps imposed by the Courant criterion to become too small and allows us to follow the growth of stars for a longer time. Once the sink particles are formed, they are decoupled from the gas and only affect gas through gravitational forces and by accretion of gas. The mass and the velocity of a sink particle is calculated from the mass and the momentum of gas particles/cells they have accreted. This allows multiple stars to be formed in a single simulation domain and allows statistical study on the mass of Pop III stars. Clark et al. (2011b) has shown that the disks form around the first generation of stars, and since the mass of these disks keep increasing, at some point, the disks start to fragment and result in multiple Pop III stars that have a broad range of masses.

Recent simulations include radiation from protostars in calculating the accretion rates (Stacy et al., 2012; Susa, 2013; Hirano et al., 2014). The picture that emerges from Hirano et al. (2014) is that there is a wide range in the mass of Pop III stars and that the low mass Pop III stars can form by radiation halting accretion onto the central star.

1.14 Observational signatures

Although the luminosity of single Population III star is not enough to be observed (Wiggins et al., 2014), the SNe resulting from Population III stars are considered to be a promising channel for observing the distant universe (Weinmann and Lilly,
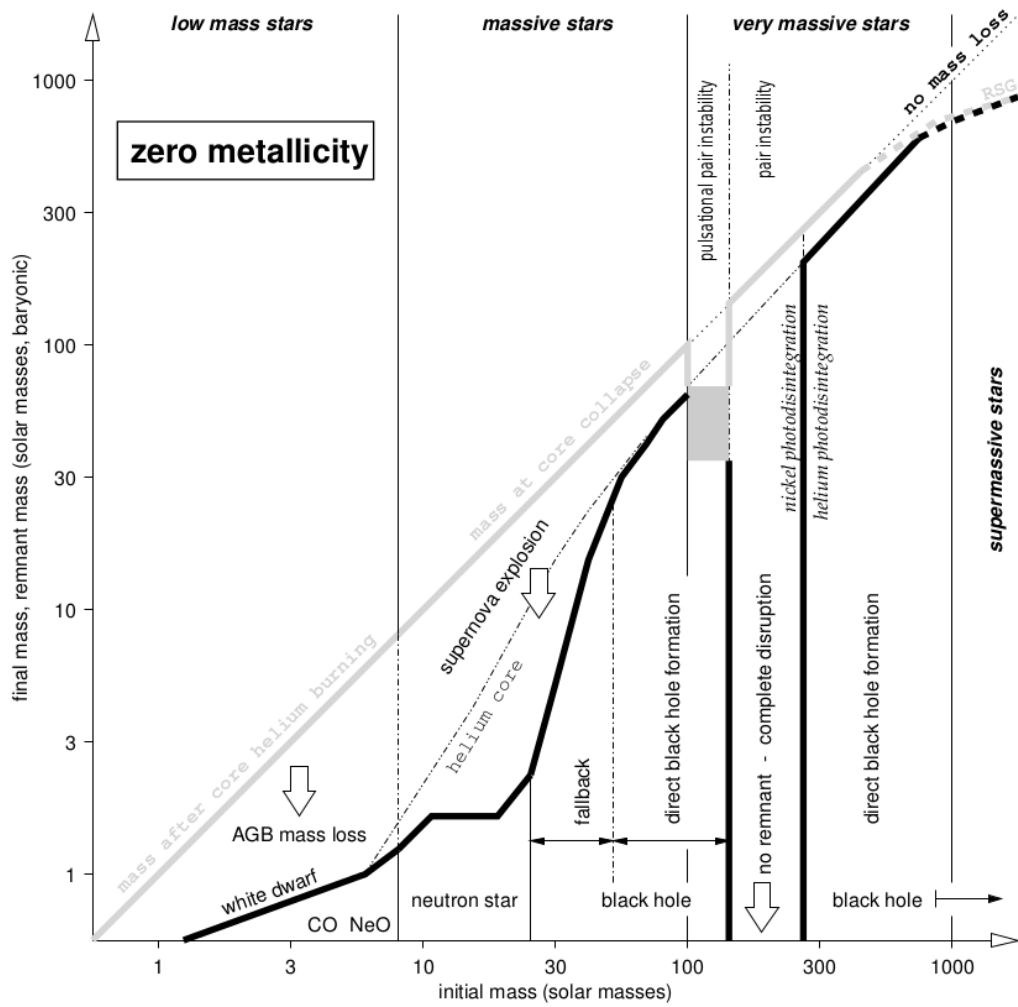
Figure 1.7: Relation between the initial and the final stellar mass. Taken from Fig. 2 in Heger and Woosley (2002)

2005; Meiksin and Whalen, 2013; de Souza et al., 2014). Gamma-Ray Busts (GRBs) are especially favoured because of their high luminosity and have long been studied as a probe of the distant universe (Bromm and Loeb, 2006). The difficulty in using GRB observation to constrain theory of Pop III star formation is that the luminosity function of GRBs is poorly determined (McLure et al., 2010; Bouwens et al., 2011) and that in metal-free stars GRBs may be much less common than in higher metallicity stars (Matzner, 2003).

There are also some attempts made to search for metal-poor stars in the Galaxy, the field known as 'stellar archaeology' (Frebel, 2010). By looking at a pattern in chemical abundances, they provide valuable information about properties of the interstellar medium from which they formed. By finding many samples of low-metallicity stars, we get stricter constraints on the model for first star formation and the later processes that produce heavy elements. A successful model would have to explain the correlation between [Fe/H] and other elements, as well as the scatter in the correlation. There has been some success in explaining observed abundances of elements by modelling yields of Pop III Supernovae or hypernovae (Tominaga et al., 2007; Heger and Woosley, 2010).

Another interesting possibility may be the 21-cm line of neutral hydrogen. This offers rich information about the state of the universe at high-redshift that is inaccessible using other methods (see e.g. Furlanetto et al., 2006).

1.15 Structure of this thesis

In Chapter 2 of this thesis, we investigate the properties of less massive dark matter structures than studied previously. Since such structure correspond to higher k in the power spectrum, the initial density perturbations are statistically different from their massive counterparts, and therefore it is worthwhile making a comparison with their lower-redshift counterparts. Another motivation to study dark matter mini-haloes are that they are the cites where Pop III star formation takes place. Chapter 3 briefly explains the principles of the moving-mesh code and describes the necessary modification we have made to the code to study the initial collapse of primordial gas. In Chapter 4, we focus on the early protostellar collapse stage of Pop III star formation, which takes place deep inside the gravitational potential well of dark matter mini-haloes, and demonstrate what decides on the abundance of HD that is formed during this phase. Chapter 5 summarises the results of this thesis.

2 Statistical properties of dark matter mini-haloes at z >= 15

The co-authors of this study are Paul C. Clark, Volker Springel, Ralf S. Klessen, and Simon C. O. Glover (Sasaki et al., 2014).

Understanding the formation of the first objects in the universe critically depends on knowing whether the properties of small dark matter structures at high-redshift ($z \geq 15$) are different from their more massive lower-redshift counterparts. To clarify this point, we performed a high-resolution N-body simulation of a cosmological volume $1\,h^{-1}$Mpc comoving on a side, reaching the highest mass resolution to date in this regime. We make precision measurements of various physical properties that characterise dark matter haloes (such as the virial ratio, spin parameter, shape, and formation times, etc.) for the high-redshift ($z \geq 15$) dark matter mini-haloes we find in our simulation, and compare them to literature results and a moderate-resolution comparison run within a cube of side-length $100\,h^{-1}$Mpc. We find that dark matter haloes at high-redshift have a log-normal distribution of the dimensionless spin parameter centred around $\bar{\lambda} \sim 0.03$, similar to their more massive counterparts. They tend to have a small ratio of the length of the shortest axis to the longest axis (sphericity), and are highly prolate. In fact, haloes of given mass that formed recently are the least spherical, have the highest virial ratios, and have the highest spins. Interestingly, the formation times of our mini-haloes depend only very weakly on mass, in contrast to more massive objects. This is expected from the slope of the linear power spectrum of density perturbations at this scale, but despite this difference, dark matter structures at high-redshift share many properties with their much more massive counterparts observed at later times.

2.1 Introduction

Understanding the formation of cosmic structures at all scales has been of central interest in the field of astrophysics for several decades. We now have a widely accepted cosmological paradigm to describe the universe, known as Λcold dark matter (ΛCDM), and its basic physical parameters are well determined today (Komatsu et al., 2011). Once this paradigm is fixed, it is conceptually a straight-forward task to follow density perturbations growing under gravity, allowing one to connect small Gaussian density perturbations in the early universe to non-linear dark matter haloes, one of which hosts our Galaxy.

An extensive body of research on studying large-scale structure formation with N-body simulations has been accumulated (Efstathiou et al. 1988, Lacey and Cole 1994, Katz et al. 1999, Kauffmann et al. 1999, Springel et al. 2005). More recently, very

large simulations that targeted the formation of the Milky Way halo, including of the order of a few billion particles in the high-resolution region, were performed and clarified the hierarchical growth process which formed our Galaxy (Diemand et al. 2008, Springel et al. 2008, Ishiyama et al. 2009, Stadel et al. 2009). However, much less work has been done on small-scale structure formation, where objects with virial radii of the order of $\sim$ kpc are resolved.

Because there is a turnover in the power spectrum of density fluctuations at $k \sim 0.01\,h\,\mathrm{Mpc}^{-1}$ comoving, and the slope of the power spectrum asymptotically approaches the critical value of -3 at high wave numbers (see Fig. 2.7), the density perturbations that exist in our initial conditions ($1\,h^{-1}\mathrm{Mpc}$ in size) at $z \sim 100$ are statistically different from those in a box of $100\,h^{-1}\mathrm{Mpc}$ in size. Therefore, there is no reason to expect that the collapsed objects forming at these different scales are strictly self-similar. Our goal is to study the small-scale regime of the power spectrum and the properties of the corresponding first dark matter haloes, and to quantify the differences with larger dark matter haloes that form later.

An important additional motivation for studying these small-scale structures lies in Population III (Pop III) star formation. Recent works (O'Shea and Norman, 2007; Gao et al., 2007; Turk et al., 2009; Clark et al., 2011a; Greif et al., 2011; Smith et al., 2011; Greif et al., 2012) show that the properties of Pop III stars (such as their masses or multiplicity) formed in each dark matter halo strongly depend on the physical conditions in the halo, and halo-to-halo differences can be large. Since cosmological hydrodynamical simulations are computationally expensive, previous calculations have focused on the first or the first few mini-haloes to collapse in the cosmological volume of interest. They studied statistical properties of Pop III stars by using a group of realisations of cosmological simulations and typically studied only one halo from each realisation. As such, halo-to-halo differences within a single cosmological realisation are still largely unknown, and our current understanding of the Pop III star formation process may be biased by our selection of the first collapsing halo. Recent works such as Hirano et al. (2014), however, have increased the number of samples significantly. But it is computationally still not possible to model all the haloes in the simulation domain with hydrodynamic simulations.

In our work, we adopt a pure N-body simulation to statistically study halo-to-halo variations on scales relevant for Pop III star formation. We model a cubic region of $1\,h^{-1}\mathrm{Mpc}$ in size using 2048^3 dark matter particles with a mass of $\sim 9\,\mathrm{M}_\odot$ each, and follow the dynamical evolution of this region from a redshift of $z \sim 100$ to $z = 15$. Full details of the simulation are provided in Section 2. To date many numerical studies of Pop III star formation have used a friends-of-friends (FOF) method to identify haloes in the computational volume (Yoshida et al., 2003). In order to make a meaningful comparison with these Pop III studies, we adopt a similar approach here. However, it has been shown that such a method of decomposing the dark matter structure can produce noisy results, with particles near the boundaries switching between neighbouring haloes somewhat randomly each time-step, or 'bridging' distinct bound structures into single larger structure (Bertschinger and Gelb, 1991). We demonstrate in Figs 2.1 and 2.2 that this is more extreme for the high-redshift dark matter haloes found in our simulations. To account for this feature of the FOF method, we use

the SUBFIND (Springel et al. 2001) method to identify dense regions inside each FOF group, and we use the most massive of these 'subhaloes' for analysis. Haloes in which SUBFIND fails to identify substructure (< 1 percent of all haloes) are removed from our analysis.

Among the previous works, our study has many similarities with the work of Jang-Condell and Hernquist (2001). We probe slightly higher redshift than they did (their analysis is at $z = 10$, whereas ours is at $z = 15$), and our simulation is carried out at significantly higher resolution: we adopt 2048^3 particles, compared to the 128^3 particles used in their study, for modelling essentially the same comoving volume in space. As such, our study presents a factor of 4000 improvement in mass resolution compared to previous systematic studies of this kind. There have also been more recent attempts to study the properties of dark matter haloes at $z = 15$ (Davis and Natarajan 2009, Davis and Natarajan 2010). While they concentrated on relatively limited properties of dark matter haloes (e.g. shape, angular momentum, clustering), our work investigates broader aspects of haloes including formation time and how physical quantities depend on formation time. In short, this paper aims at new precision measurements of statistical properties of dark matter haloes in the early universe as enabled by our high-resolution N-body simulations.

This paper is structured as follows. In Section 2, we discuss the numerical methods adopted in our work, and in Section 3, we present and discuss our results. Finally, we give our conclusions in Section 4. An Appendix informs about technical aspects of our analysis such as convergence tests.

2.2 Methods

We have performed an N-body cosmological simulation with 2048^3 dark matter particles, using the GADGET-3 code. Our initial conditions were generated using N-GenIC, the initial condition generator originally developed for the Millenium Simulation (Springel et al., 2005). We first identify haloes by the friends-of-friends (FOF) algorithm with a standard linking length of $b = 0.2$ in units of the mean particle spacing, corresponding to $\sim 0.1\,h^{-1}$kpc in comoving units, followed by an application of the substructure finding algorithm SUBFIND to identify bound structures within haloes. Substructures thus defined are used for constructing a merger tree, and the most massive substructure identified in a given FOF group, referred to as 'main subhalo', is analysed throughout this study, unless otherwise noted.

We employ cosmological parameters consistent with the WMAP-7 measurements ($\Omega_m = 0.271$, $\Omega_\Lambda = 0.729$, $\sigma_8 = 0.809$, $h = 0.703$; Komatsu et al., 2011)[1]. The simulation box is $1\,h^{-1}$Mpc in length, and thus the particle mass in our simulation is $\sim 9\,\mathrm{M}_\odot$. We set the gravitational softening length to be $0.01\,h^{-1}$kpc. The lengths quoted here are in comoving units. We started from a redshift $z \sim 100$ and followed the formation of dark matter haloes down to $z = 15$, by which time numerous dark matter haloes capable of hosting Pop III stars have formed. Unless otherwise noted,

---

[1]We would not expect our results to differ significantly if we were to use the WMAP-9 parameters (Hinshaw et al., 2013), or those measured by Planck (Planck Collaboration et al., 2013).

we analysed the simulation output at the end of simulation (i.e. $z = 15$). Hereafter we refer to this simulation as the 'Small' run.

We also performed a moderate-resolution comparison simulation at larger scales, using 512^3 particles to follow structure formation inside a region of $100\,h^{-1}\mathrm{Mpc}$ on a side with force softening length $4.0\,h^{-1}\mathrm{kpc}$. The results of this comparison simulation are mostly presented in Appendix A.1, which we will refer to where necessary. This simulation is referred to as the 'Large' run hereafter. The essential parameters of the two simulations are summarised in Table A.1.

2.2.1 Merger trees

A FOF group is identified by linking all particles that are separated by less than a fraction $b = 0.2$ of the mean particle separation. Thus, this method is approximately selecting regions that are by a factor of $1/b^3$ denser than the mean cosmic density (by this choice of b, naively we expect that the selected region corresponds to an overdensity ~ 200 relative to the background, similar to the expected virial overdensity according to the top-hat collapse model). However, FOF is known to occasionally link separate objects across particle bridges, and it is also not suitable for identifying bound substructures inside dense regions.

Therefore, in each FOF group, bound substructures are identified using SUBFIND[2]. In short, inside each FOF halo, locally overdense regions are spotted by identifying saddle points in an adaptively smoothed dark matter density field. The latter is constructed with an SPH smoothing kernel with $N_{\mathrm{dens}} = 64$ neighbours, while the topological identification of locally overdense regions is based on $N_{\mathrm{ngb}} = 20$ nearest neighbours (the notation here follows Springel et al. 2001). Two structures connected with only a thin bridge of dark matter particles would be identified as two different (sub)haloes by SUBFIND. Each dark matter particle inside a FOF group is either associated to one subhalo or to none. In the algorithm, all subhaloes are checked to see whether they are gravitationally bound. In defining a formation time for dark matter halo, we shall concentrate on the most massive subhalo in each FOF halo at the final output time; the most massive subhalo typically contains a dominant fraction of the mass of its host FOF halo.

For each FOF group, we investigate when its most massive subhalo gained half of its final mass at $z = 15$. This is done by following the merger tree along the most massive progenitor in adjacent snapshots. We estimate the formation time by linearly interpolating between the bound mass of subhalo at two subsequent SUBFIND output times: one output immediately after the subhalo gained half its final mass, and one output immediately before. A similar approach is adopted in works such as that of Gao et al. (2005).

---

[2]We refer the reader to Springel et al. (2001) for the details of the algorithm.
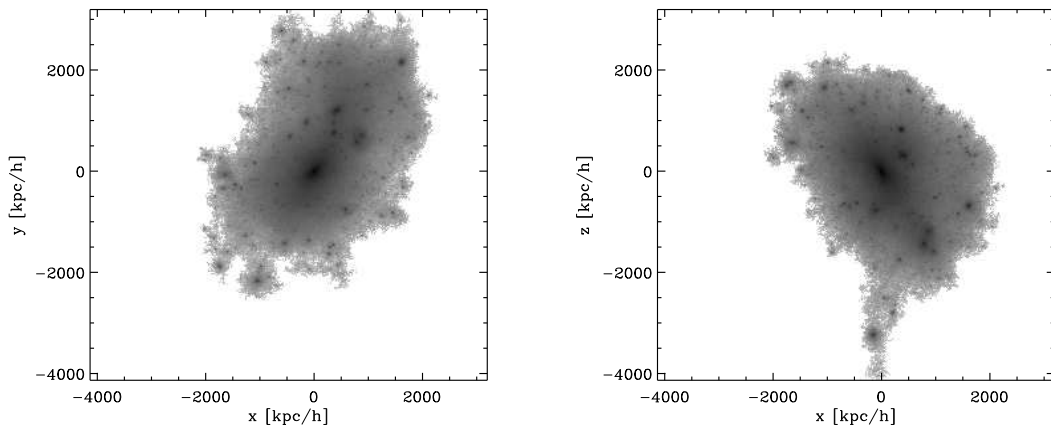
Figure 2.1: One example of a FOF halo found in the 'Large' run at $z = 0$. Its shape resembles a sphere, and it is rich in substructure.

2.3 Results

In the following, we determine and discuss various physical properties that characterise dark matter haloes, and try to clarify differences and similarities of dark matter structures that reside at early time in a small box of $\sim 1\,h^{-1}\mathrm{Mpc}$ on a side, relative to those forming later in a larger ($\sim 100\,h^{-1}\mathrm{Mpc}$) simulation box.

In Fig. 2.1 and Fig. 2.2, we show representative density maps of FOF objects taken from our 'Large' and 'Small' runs, respectively. It is easily recognisable that the particular FOF halo shown at $z = 15$ is filamentary and appears to be composed of different dense regions that are connected together. In contrast, the FOF halo at $z = 0$ is much more spherical, and contains rich substructure. While not as extreme in all cases, we confirmed these general differences through inspection of a large number of images of different haloes. Since the particles located at the outer regions of each FOF haloes are typically not bound to the halo, and could therefore obscure our analysis of the halo binding, shape, etc. in later sections we chose to analyse the most massive substructure identified by SUBFIND in each FOF halo.

2.3.1 Spin parameter

We begin with the dimensionless spin parameter of a halo. It is defined as

$$\lambda = \frac{J|E|^{1/2}}{GM^{5/2}}, \tag{2.1}$$

where J is the total angular momentum of a halo, E is the total energy, G is the gravitational constant, and M is the mass. For objects in the Keplerian rotation, this
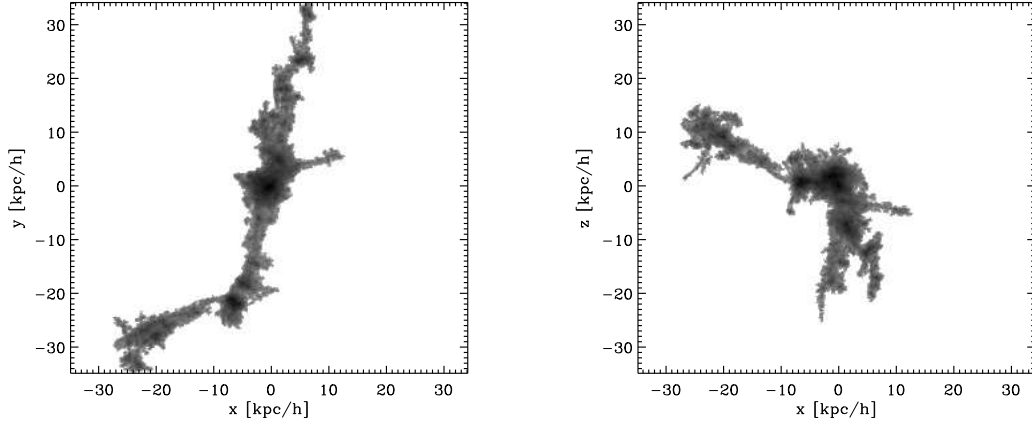
Figure 2.2: One example of a FOF halo found in the 'Small' run at $z = 15$. It has a filamentary shape.

value is of the order of unity. For our analysis of angular momentum, we included only haloes that have at least 1000 particles inside their main subhaloes, i.e. with a minimum mass of $\sim 10^4 \, M_\odot$. The spin of dark matter haloes is a result of tidal torques that they experience during their formation and subsequent evolution (White, 1984).

We show the median, and 20%, 80% percentiles of this parameter in a series of logarithmic mass bins in Fig. 2.3. We find that at all the redshifts we looked at, the spin parameter λ weakly depends on mass.

The distribution of λ is often fitted by a log-normal distribution (Warren et al., 1992):

$$p(\lambda) \, \mathrm{d}\lambda = \frac{1}{\sqrt{2\pi}\sigma_\lambda} \exp\left[-\frac{\ln^2(\lambda/\bar{\lambda})}{2\sigma_\lambda^2} \right] \frac{\mathrm{d}\lambda}{\lambda}. \tag{2.2}$$

We obtained a log-normal fit to the spin distribution at $z = 15$ with parameters $\bar{\lambda} = 0.0262$ and $\sigma_\lambda = 0.495$ (Fig. 2.4, top) for all haloes with at least 1000 particles. In other parts of this paper, lower limit of 100 particles is introduced such that lower mass haloes, which are not well-resolved, will be excluded from our analysis in this paper (shape, virial ratios, formation times etc). We adopted a more demanding criterion here, since the spin parameter is known to depend more strongly on how well the dark matter haloes are resolved than other physical parameters (Davis and Natarajan 2010, see also Appendix A.3 of this paper). Jang-Condell and Hernquist (2001) found that the spin distribution follows a log-normal distribution at $z = 10$ (with $\bar{\lambda} = 0.033$, which is overplotted with a dashed-line in Fig. 2.4). The similar value in $\bar{\lambda}$ is a bit surprising, because although we model essentially the same volume in comoving space with slightly different redshift, the different mass resolutions in the

two simulations mean that we resolve dark matter haloes in different mass ranges. This outcome is however consistent with findings from analytical works that predict that $\bar{\lambda}$ has no strong dependence on the power spectrum (Heavens and Peacock, 1988).

Since we calculate spin parameter from substructure within FOF haloes, we do not suffer from artificial high-end tail of spin distribution in Fig. 2.4 as in Bett et al. (2007), who analysed a simulation output produced with the same code as ours, GADGET-3, on a larger scale but chose to analyse FOF haloes.

Because the spin of a halo is a sum of slight differences in position and velocity space, it is sensitive to how well the halo is resolved. As such, our study qualifies as the most precise measurement of the spin parameter at $z = 15$ thus far. We expect that our estimate of the spin parameter for subhaloes with mass $> 10^4\, h^{-1}\mathrm{M}_\odot$ (corresponding to $> 10^3$ particles) is correct within a factor of 2 at a $1\,\sigma$ level (Trenti et al., 2010). We obtain $\bar{\lambda} = 0.0247$ and $\sigma_\lambda = 0.486$ for haloes in the mass range $10^{5\pm0.2}\, h^{-1}\mathrm{M}_\odot$ and $\bar{\lambda} = 0.0274$ and $\sigma_\lambda = 0.495$ for haloes in the mass range $10^{4\pm0.2}\, h^{-1}\mathrm{M}_\odot$ (Fig. 2.4, bottom). This is in contrast to the result of Davis and Natarajan (2009), where they find the more massive haloes to have systematically larger spin. This is a result of different halo identification algorithms. The particles that lie in the surfaces of dark matter haloes contribute little in terms of mass but much in terms of angular momentum. Therefore, the actual value of spin parameter heavily depends on halo identification methods employed. Comparison of Figs 2.3 and A.5 shows that the FOF gives a positive correlation between spin and halo mass, which is not present when we employ the more conservative SUBFIND method.

In simulations with dark matter and gas, it has been found that the spin parameters of both components follow similar distributions (van den Bosch et al., 2002). As we aim to study the environmental conditions of first star formation, knowledge of λ is a key prerequisite. There is a recent work that estimates the Pop III initial mass function (IMF) from the rotational velocity of haloes (de Souza et al., 2013). Hirano et al. (2014) selected ~ 100 haloes from multiple realisations of structure formation and resimulated many samples of Pop III star forming regions in a suite of two-dimensional radiation hydrodynamic simulations, ending up with a statistical study of the final mass of a single protostar. Their spin distribution of the dark matter component is centred on $\bar{\lambda} = 0.0495$, considerably higher than the values found in most pure dark matter simulations including ours. This is largely due to a selection effect and the positive mass-spin relationship of FOF haloes described earlier: these authors employed a standard FOF algorithm to extract the haloes, and focused on the more massive haloes in the simulation (i.e. those massive enough to have triggered H_2 cooling), which are likely to have higher spin.

2.3.2 Virial ratios

In this paper, we define the virial ratio as $2.0 \times E_\mathrm{K}/E_\mathrm{G}$, so that a value of unity corresponds to virial equilibrium. The total kinetic energy E_K is defined as

$$E_\mathrm{K} = \frac{1}{2}\Sigma_i\, m_i v_i^2 \;, \tag{2.3}$$
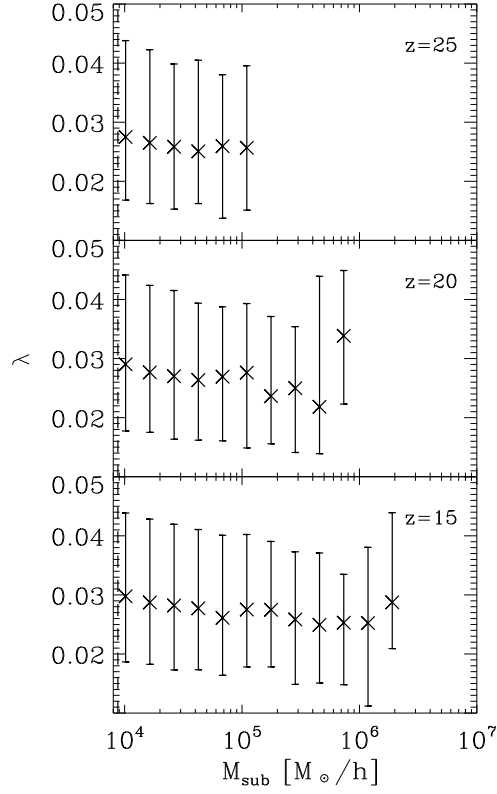
Figure 2.3: Distribution of the dimensionless spin parameter λ in dark matter haloes of different mass at redshift $z \sim 25$ (top panel), $z \sim 20$ (middle panel), and $z \sim 15$ (bottom panel). Crosses indicate the median value of λ, while the error bars indicate the 20th and 80th percentiles. The dashed vertical lines represent lower mass limit of 1000 particles. We exclude any bins that contained less than 10 samples. The same holds for Fig. 2.5.
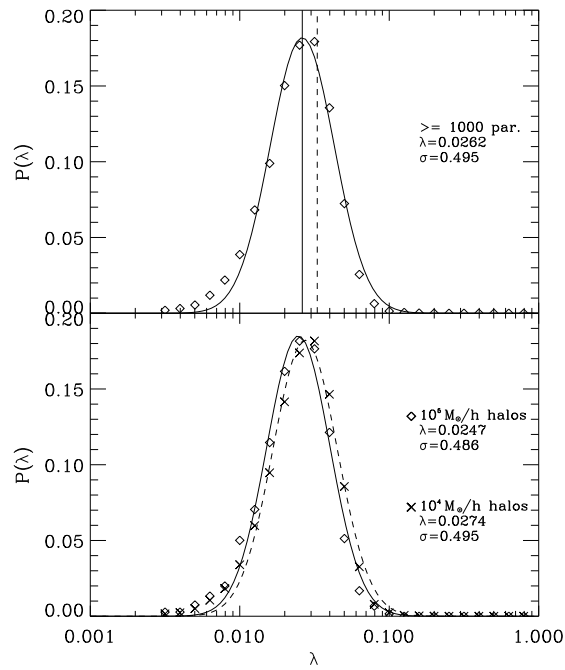
Figure 2.4: The top panel is the spin distribution for all haloes with ≥ 1000 particles at $z = 15$. The bottom panel shows the spin distribution for haloes within a mass range of $10^{5\pm0.2}\,h^{-1}\mathrm{M}_\odot$ (diamonds) and $10^{4\pm0.2}\,h^{-1}\mathrm{M}_\odot$ (crosses). The symbols represent data from our simulations, and the lines indicate log-normal fits. The vertical solid (dashed) lines represent $\bar{\lambda}$ for our (Jang-Condell and Hernquist 2001) simulation.

with velocity being defined relative to the centre-of-mass velocity of the halo throughout this paper. The gravitational potential energy E_G is defined as

$$E_G = \frac{1}{2} \sum_{i \neq j} G \frac{m_i m_j}{r_{ij}}. \tag{2.4}$$

The sum is taken over all particles i and j that belong to the main subhalo in a specific FOF halo, with m_i and m_j being their mass, and r_{ij} their distance. This quantity is numerically calculated by direct summation.

Fig. 2.5 shows the distribution of virial ratios for different dark matter haloes at redshifts $z \sim 25$ (top), 20 (middle), 15 (bottom). We see that there is some variation in this quantity, but the median, and the 20%, 80% percentiles of the virial ratio are well above unity for all mass ranges we have investigated, and thus the dark matter haloes are not virialized but instead are usually perturbed. This has previously been noted by Jang-Condell and Hernquist (2001) and Davis and Natarajan (2010), with relatively low resolution at high redshifts, and also by, for example, Hetznecker and Burkert (2006) at lower redshifts, $z < 3$. It is also beneficial to compare results of the 'Large' box run with the 'Small' run. It is clear from Fig. A.3 that dark matter haloes found in the larger simulation box at $z = 0$ have systematically lower virial ratios, and are thus closer to virial equilibrium than those at $z = 15$.

The median value of the virial ratio in Fig. 2.5 increases with increasing halo mass. The median value of a given mass bin does not evolve considerably over a range of redshift, in contrast to Hetznecker and Burkert (2006), who have found that the virial ratio decreases monotonically with redshift between $z = 3$ and $z = 0$. These differences reflect the different dynamical states of dark matter mini-haloes at $z \geq 15$ and more massive systems at $z < 3$.

Our results show that dark matter haloes at $z \sim 15$ cannot be considered to typically represent isolated systems undergoing collapse (see also discussion in Section 2.3.6). The excess kinetic energy of the dark matter haloes, if shared by their gas component, could influence the star formation taking place because the properties of the turbulence in the interstellar medium strongly influence the star formation process within them (Clark et al. 2011a, Prieto et al. 2012). Distinguishing relaxed haloes from unrelaxed haloes is not a straight-forward task, and needs to be based on complex criteria that involve, for example, virial ratios and the fraction of mass in substructures (Neto et al., 2007). Our simple definition of virial ratio should however already give a useful proxy for the dynamical state of a halo.

2.3.3 Mass function

We now compare the halo mass distribution with predictions of analytical models. Let Δn be the number density of objects with mass (FOF mass found for our groups or mass of main subhalo in our group) within a logarithmic bin, and $\Delta \log M$ be $\log M_2/M_1$ where M_2/M_1 is the ratio of upper and lower values for each mass bin (constant). In Fig. 2.6, $\frac{\Delta n}{\Delta \log M}$ is plotted against the median value in each mass bin along with Poisson error bars (error bars are omitted for subhalo data for easy
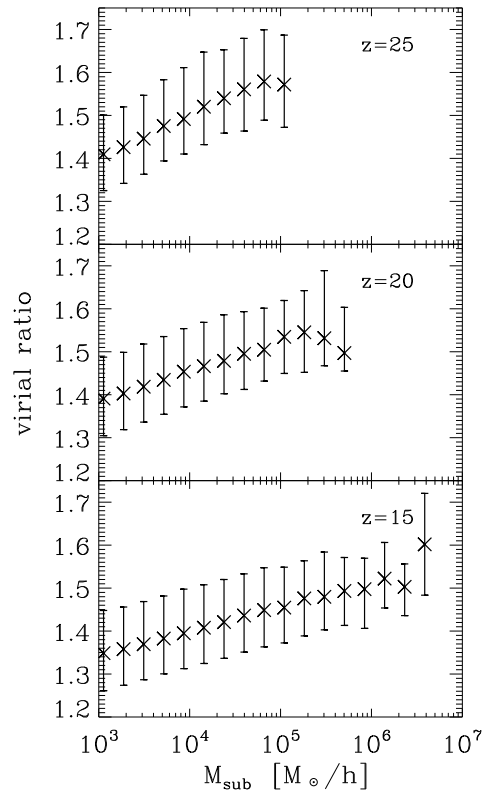
Figure 2.5: Distribution of the virial ratio in dark matter haloes of different mass at redshift $z \sim 25$ (top panel), $z \sim 20$ (middle panel), and $z \sim 15$ (bottom panel). The virial ratio is defined such that it tends to unity at virial equilibrium. Crosses indicate the median value of the virial ratio, while the error bars indicate the 20th and 80th percentiles. The mass bins are spaced logarithmically, and symbols are only plotted for bins containing at least 10 dark matter haloes.
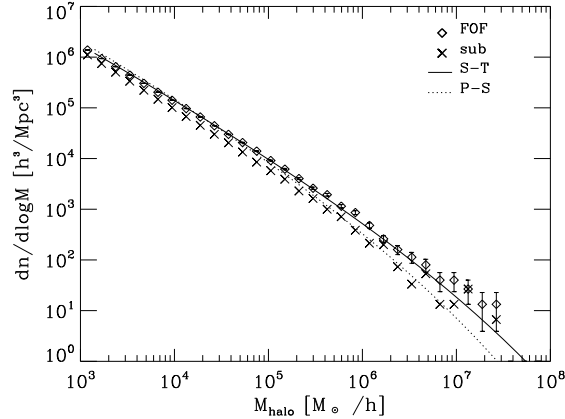
Figure 2.6: Mass function of dark matter haloes at $z = 15$ (diamond symbols represent number counts for FOF haloes, when crosses denote those for the main subhalo in a FOF halo). The Press-Schechter (Press and Schechter, 1974) and Sheth-Tormen functions (Sheth and Tormen, 1999) are over-plotted.

recognition). The analytical Press-Schechter (Press and Schechter, 1974) and Sheth-Tormen models (Sheth and Tormen, 1999) are plotted with continuous and dotted lines, respectively. The Press-Schechter function underestimates the number of haloes in the high mass range, whereas the Sheth-Tormen function gives a good fit to the simulated FOF data over a broad range of masses including the high-mass end. Since subhaloes contain only part of mass of its host FOF haloes and therefore some of the haloes that belonged to a particular mass bin is shifted to neighbouring lower mass bin, number density of subhaloes in a given mass bin is systematically smaller than FOF haloes. Overall, we find that these analytical fitting formulae reproduce not only the statistics of dark matter haloes with mass $10^7 \, h^{-1} \mathrm{M}_\odot$ as previously known (Ishiyama et al., 2013) at $z = 0$, but they also describe less massive haloes obtained from our simulations, such as those as small as $10^3 \, h^{-1} \mathrm{M}_\odot$ at $z = 15$.

2.3.4 Formation time

The linear power spectrum of density perturbations at $z = 0$ for the cosmological parameters we adopt in our work is plotted in Fig. 2.7, where the dark blue line show the critical slope of -3. In this section, we express the slope of the power spectrum by p. Therefore, $P(k) \propto k^p$, where the slope p changes as a function of wavenumber k. For the linear power spectrum shown in Fig. 2.7, $p = -2.37, -2.62, -2.74, -2.80$ at $k = 1, 10, 100, 1000h \, \mathrm{Mpc}^{-1}$.

The power spectrum increases at very low wavenumbers, then turns over and starts to decrease again, approaching power law with $p \simeq -3$ at high wavenumbers. For the mass scales extensively studied by earlier works, $M_{\mathrm{halo}} \sim 10^{12} \, h^{-1} \mathrm{M}_\odot$, the slope is substantially shallower compared to a mass scale of $M_{\mathrm{halo}} \sim 10^6 \, h^{-1} \mathrm{M}_\odot$ where
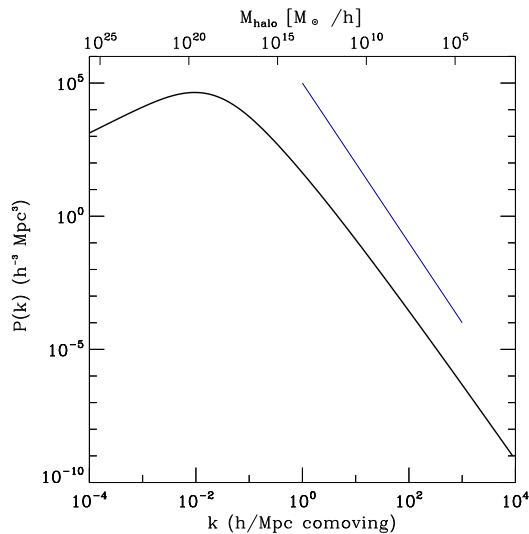
Figure 2.7: The linearly extrapolated power spectrum of dark matter at $z = 0$ for the cosmological parameters we adopt. The critical slope of k^{-3} is shown with dark blue line.

the slope is close to the critical value of $p = -3$. It is critical in the sense that the non-dimensional power,

$$\Delta^2(k) = \frac{k^3 P(k)}{2\pi^2} \tag{2.5}$$

becomes independent of wavenumber k. $\Delta^2(k)$ represents the amount of perturbations in a logarithmic bin in k. For $p > -3$, $\Delta^2(k)$ is a monotonically increasing function of k. Therefore, given $p > -3$, for a fixed time, there is more power in small scales (large k) than in large scales (small k). Thus, small gravitational structures form first in such regimes (explicitly shown in Fig. 1 in Harker et al. 2006). In contrast, for $p = -3$, $\Delta^2(k)$ is independent of wavenumber k, thus the dark matter structures of various mass collapse simultaneously and in a non-hierarchical fashion. We now show this explicitly using our high-resolution simulation.

Adopting the methods described in Section 2.2.1, we identified the formation time of each FOF halo. In Fig. 2.8, we divide dark matter haloes in various mass bins and plot the median, and 20%, 80% values of formation time in each mass bin. We find that in the mass range we are interested in, massive dark matter haloes and small haloes form simultaneously (this is only true statistically, because there is a dispersion of $\sim 10\,\mathrm{Myr}$ in the formation time in a given mass bin). This is quite different from the more massive regime, where less massive haloes form first (Harker et al. 2006, also see results of the 'Large' run in Fig. A.2). This implies that the formation processes of dark matter mini-haloes found at high redshift in a simulation box of $1\,h^{-1}\mathrm{Mpc}$ differ substantially from those found at much higher halo masses in larger boxes.
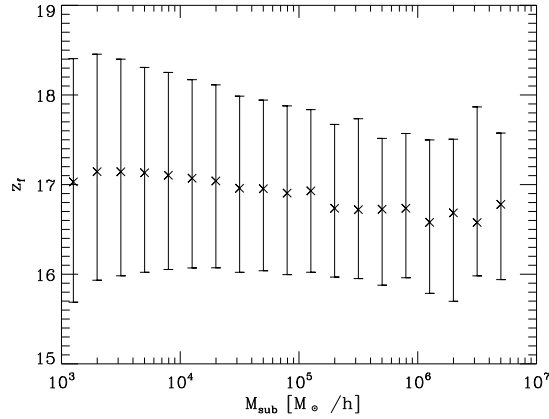
Figure 2.8: Formation time of dark matter haloes as a function of their mass. Median, 20 %, and 80 % values in each mass bin are plotted. Haloes that differ in mass by $\sim$ four orders of magnitude form simultaneously. This is quite different from the formation time for more massive systems at $z = 0$. Compare with Fig. A.2.

2.3.5 Halo shape

Often the high-density regions found in collisionless N-body simulations are not exactly spherically symmetric, as opposed to the assumption which is made to derive Press-Schechter mass function for example. Modelling dark matter haloes as ellipsoids and measuring their three axes provide a way to quantify the shape of these haloes and how much it differs from the spherical collapse model. Moreover, there are several different kinds of approaches made observationally to estimate halo shapes in the local universe: First, there are ways to measure dark matter distribution by weak lensing using X-ray clusters (Oguri et al., 2010). Secondly, there are also attempts to determine dark matter halo shapes for galaxies statistically using surveys (Hoekstra et al., 2004). Lastly, there are also efforts made to derive the gravitational potential of our Galaxy by using the kinematics of tidal tails of the Sagittarius dwarf spheroidal galaxy (Law et al., 2009). The less massive haloes found in our study are influenced by a much shorter wavelength portion of the ΛCDM power spectrum than the haloes examined in these observational studies, and it is therefore interesting to see whether there is any systematic difference in the shapes of these mini-haloes.

We define a second moment tensor of the halo shape as:

$$I_{ij} = \sum_n x_i x_j, \tag{2.6}$$

where x_i ($i = 1$, 2, 3 corresponding to x, y, and z coordinates) is the particle position with respect to the centre of the halo, which we define as the position of the particle with the lowest potential energy. The same form of the shape matrix was adopted
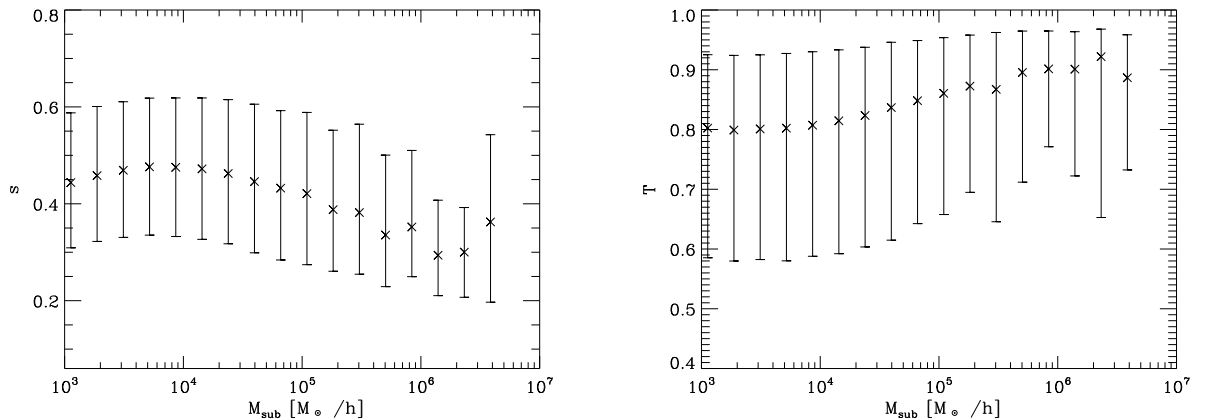
Figure 2.9: Median of sphericity s and triaxiality T in different mass bins for dark matter haloes at $z = 15$. The sphericity and triaxiality are defined by equations (2.10) and (2.11), respectively.

in the earlier studies of Jang-Condell and Hernquist (2001) and Macciò et al. (2008). We note that sometimes I_{ij} is defined as $\sum_n x_i x_j / r'^2$, i.e. with a $1/r'^2$ normalisation factor (Moore et al. 2004, Allgood et al. 2006). But we here adopt the former, more widely used formulation.

The sum is taken over all the particles that belong to the main subhalo in a FOF halo. After evaluating the inertia tensor, we compute its eigenvalues I_1, I_2, and I_3, which are the three principal moments of inertia of the halo, and which satisfy the relationship $I_1 \geq I_2 \geq I_3$. The lengths of the axes a, b, and c associated with the principal moments of inertia are given by

$$a = \sqrt{(5\,I_1)/N_p}, \tag{2.7}$$

$$b = \sqrt{(5\,I_2)/N_p}, \tag{2.8}$$

$$c = \sqrt{(5\,I_3)/N_p}, \tag{2.9}$$

where N_p is the number of particles summed up in equation (2.6). The sphericity of the halo is then defined as

$$s = c/a. \tag{2.10}$$

From the above formulation, it should be clear that a spherically symmetric halo has $s = 1$. The triaxiality of the halo is defined as

$$T = (a^2 - b^2)/(a^2 - c^2). \tag{2.11}$$

By definition, an oblate halo ($a = b > c$) has $T = 0$, and a prolate halo ($a > b = c$) has $T = 1$.

Black solid lines in the different rows in Fig. 2.10 show the distribution of sphericity s for different mass ranges (namely haloes with mass $10^{4\pm0.2}\,h^{-1}\mathrm{M}_\odot$, $10^{5\pm0.2}\,h^{-1}\mathrm{M}_\odot$, and $10^{6\pm0.2}\,h^{-1}\mathrm{M}_\odot$). We find that the distribution of s based on all haloes has a peak at $0.4-0.45$, which is smaller than the value typically found for more massive haloes at lower redshifts. For example, Allgood et al. (2006) and Macciò et al. (2008) investigated haloes with masses $\sim 10^{12}\,h^{-1}\mathrm{M}_\odot$ to $10^{15}\,h^{-1}\mathrm{M}_\odot$ and found almost no haloes with $s < 0.4$. This could be due to more frequent mergers at $z = 15$ compared to $z = 0$.

If we compare the distribution function of s and T, $10^5\,\mathrm{M}_\odot$ haloes are more likely than $10^4\,\mathrm{M}_\odot$ haloes to have lower values of sphericity s and higher values of triaxiality T. This tendency of more massive haloes having small s and larger T, that has been observed elsewhere (Allgood et al. 2006, Macciò et al. 2008), is even clearer in Fig. 2.9, in which we show median values of s and T as a function of halo mass. Comparing Fig. 2.9 with Fig. A.1, we find that haloes found at $z = 0$ are systematically more spherical and only moderately more prolate compared to haloes at $z = 15$.

Fig. 2.10 also shows that for all the three different mass ranges studied here, a large fraction of haloes are prolate ($T \sim 1$). This is similar as found in previous studies that focused on haloes forming in different regimes (e.g. more massive haloes, Dubinski and Carlberg 1991, Warren et al. 1992). This is most likely because dark matter haloes of various mass scales form from filamentary structures. However, we find a significant disagreement with de Souza et al. (2013), who worked on similar mass ranges and practically the same redshift, but with hydrodynamical simulations. Their dark matter haloes with mass $\sim 10^5\,\mathrm{M}_\odot$ at $11 < z < 16$ have $s \sim 0.3$ and more than 90% have $T \lesssim 0.4$, whereas the dark matter haloes with mass $\sim 10^5\,h^{-1}\mathrm{M}_\odot$ at $z = 15$ in our simulations have medians $s \sim 0.4$ and $T \sim 0.85$. We note that de Souza et al. (2013) adopt a definition of I_{ij} equivalent to ours. The difference in shape could be due either to the inclusion of gas cooling or to a very different mass resolution. We resolve substructures inside dark matter haloes with mass $\sim 10^5\,h^{-1}\mathrm{M}_\odot$ with $\sim 10^4$ particles, whereas de Souza et al. (2013) resolve haloes with the same mass with only ~ 200 particles. We speculate that the inclusion of gas makes a bigger difference than the mass resolution, however, since our convergence study shows that even with a relatively small particle number of 200 particles or so, the errors in the axial ratios (b/a, c/a) remain within 10% (see Table A.2).

Histograms with different colour in Fig. 2.10 represent halo shape distributions for haloes with different values of the spin parameter. We sorted dark matter haloes in each mass range into percentiles according to their spin. If we denote the 33% and 67% percentile values of the spin parameter in each mass range as $\lambda_{1/3}$ and $\lambda_{2/3}$, we have plotted the probability distribution of halo shapes for three different kinds of halo selections: all the haloes in a certain mass range, only haloes with $\lambda > \lambda_{2/3}$, and only haloes with $\lambda < \lambda_{1/3}$. We found that, in all the mass ranges we looked at, dark matter haloes with high spin are less spherical and more highly prolate, a trend already confirmed in lower redshift dark matter haloes by previous works (Bett et al., 2007). Davis and Natarajan (2010), who used different methods to identify haloes and estimate their shapes, also found similar trends for high-redshift dark matter haloes with relatively low resolution. This widely observed correlation could occur because

haloes that experienced strong gravitational forces during their formation are likely to have high spin and an aspherical shape.

In short, using the highest-resolution simulation to date for resolving a large sample of substructure inside dark matter mini-haloes of mass $> 10^3\,\mathrm{M_\odot}$, we have demonstrated that dark matter mini-haloes we find in our simulations at $z \sim 15$ have qualitatively many similarities with dark matter haloes found at $z <\sim 6$ regarding their shape.

2.3.6 Correlation between formation time and virial ratio / formation time and halo shape

Many authors have studied the effect of the mass accretion history on the concentration and density profile of dark matter haloes (Bullock et al. 2001, Wechsler et al. 2002, Tasitsiomi et al. 2004). Much less work has been done on the relationship between formation time and other halo properties. For dark matter haloes found in mass scales capable of hosting Pop III star formation, we show for the first time that there is a direct connection between the shape of a halo, its dynamical state, or its spin and its formation time. This could provide interesting clues on the formation processes of dark matter haloes.

We sorted the dark matter haloes in different mass bins into three groups according to their formation time. In Fig. 2.11, we show that the haloes that formed later (young haloes) have higher values of the virial ratio, while in Figs 2.12 and 2.13, we show that haloes that formed later (young haloes) have smaller sphericities and larger spin parameters. This is because haloes of a given mass that formed later accumulated their mass recently, and thus had no time for relaxation.

To clarify this point, let us make comparison of relevant time-scales. The Hubble time, $t_{\mathrm{H}} = a/\dot{a}$ is ~ 300 Myr at $z = 15$. If we estimate the relaxation time t_{relax} of dark matter haloes by $t_{\mathrm{relax}} = \frac{1}{\sqrt{G\rho}} = \frac{1}{\sqrt{G200\rho_{\mathrm{crit}}(z=15)}}$, $t_{\mathrm{relax}} \sim 60$ Myr at $z = 15$ ($< t_{\mathrm{H}}$, as expected). The old haloes analysed here typically formed at around $z = 18 - 20$ whereas the young haloes formed at $z < 16$. Thus the former typically had more than $\Delta t(z = 18, z = 15) \sim 80$ Myr ($> t_{\mathrm{relax}}$) while the latter had less than $\Delta t(z = 16, z = 15) \sim 45$ Myr ($< t_{\mathrm{relax}}$) since the time of formation. This could account for the differences in physical properties we observe when we stop our simulation at $z = 15$.

In fact, Hetznecker and Burkert (2006) have demonstrated that major mergers increase the value of the spin parameter and the virial ratio. Allgood et al. (2006) have also found that haloes forming earlier (old haloes) are more spherical. They have also shown that the dependence on formation time is weaker for higher mass haloes, at least in their simulation box. The different methods adopted to calculate halo shape and formation time preclude a direct comparison, but the high-mass end of Fig. 2.12 clearly shows similar trends.

Our results confirm that the formation epoch of dark matter haloes influences global parameters such as shape, virial ratio, and spin. Each dark matter halo has a different evolution history. Furthermore, even the dark matter haloes that have similar mass accretion histories could have accreted their mass from different spatial locations or through different channels. A single global parameter such as formation time is not
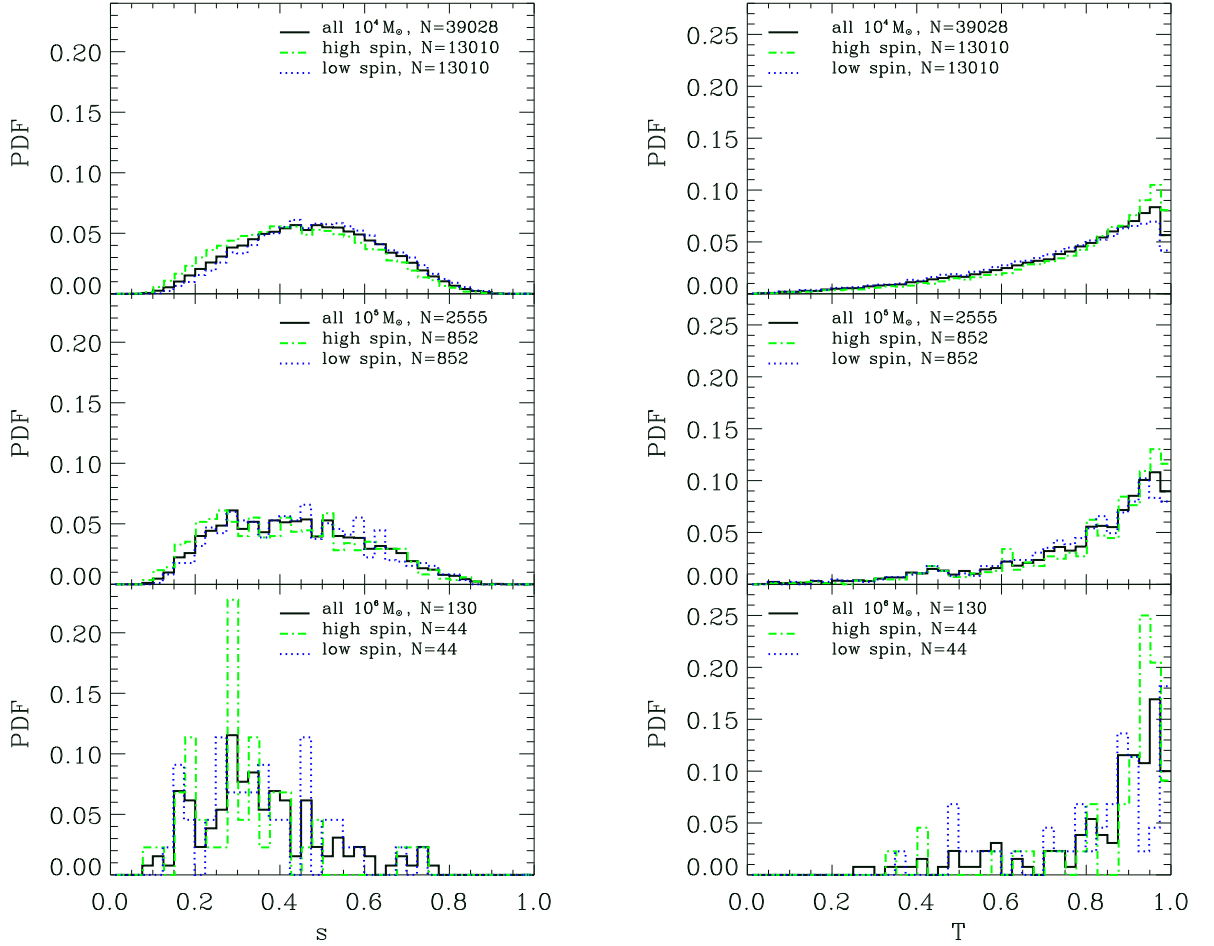
Figure 2.10: Sphericity s and triaxiality T for haloes with mass $10^{4\pm0.2}\,h^{-1}\mathrm{M}_\odot$, $10^{5\pm0.2}\,h^{-1}\mathrm{M}_\odot$, and $10^{6\pm0.2}\,h^{-1}\mathrm{M}_\odot$ at $z = 15$. Different lines represent distributions for different groups in each mass range. (Blue dotted lines correspond to haloes with $\lambda < \lambda_{1/3}$, green dash-dotted lines correspond to haloes with $\lambda > \lambda_{2/3}$, and black solid lines correspond to all subhaloes in that mass range.)
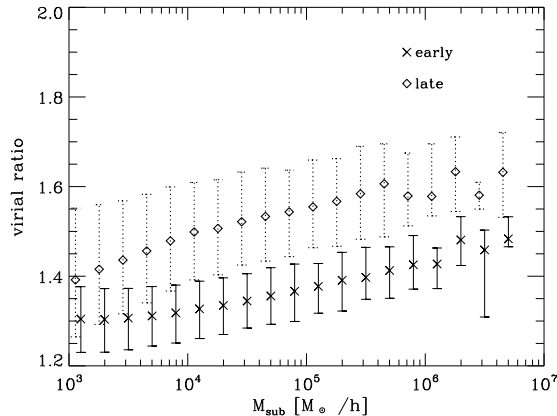
Figure 2.11: Relation between formation time and virial ratios. We grouped the haloes
in each mass bin into three groups. Early one-third (old haloes), middle
one-third (intermediate haloes), and late one-third (young haloes). We
plot the median values for early (crosses) and late (diamonds) thirds.
The error bars indicate 20th and 80th percentile values for each group.
(Error bars are plotted in solid lines for haloes forming earlier, and in
dotted lines for haloes forming later. For easy reference, haloes forming
later are slightly offset in mass.) We found that haloes that formed later
(young haloes) have higher virial ratios on average due to lack of time
for relaxation.

enough to account for this, and the scatter in Figs 2.11 and 2.12 could be due to
variations in the processes that let haloes accumulate their mass.

2.3.7 Correlation function

The two-point correlation function calculated from N-body simulations is a useful
quantity, since it can be compared directly with galaxy clustering data (Springel et al.,
2005). We perform a similar analysis to clarify the properties of the mini-haloes we
find at $z = 15$. Gao et al. (2005) have demonstrated that haloes that assembled earlier
are more strongly clustered, casting doubt on an assumption made in excursion-set
theory (Bond et al., 1991), namely that halo properties depend only on mass and are
independent of environment.

Here we study the clustering of haloes with different spins. In order to quantify the
clustering between dark matter mini-haloes, we make two kinds of catalogues of dark
matter haloes: a simulated halo catalogue and a random catalogue. The simulated
halo catalogue is a list of positions of haloes obtained from our simulation. The
random catalogue is a list of random points distributed in a box that is equal in size
to our simulation box. We measure the two-point correlation function $\xi(r)$ following
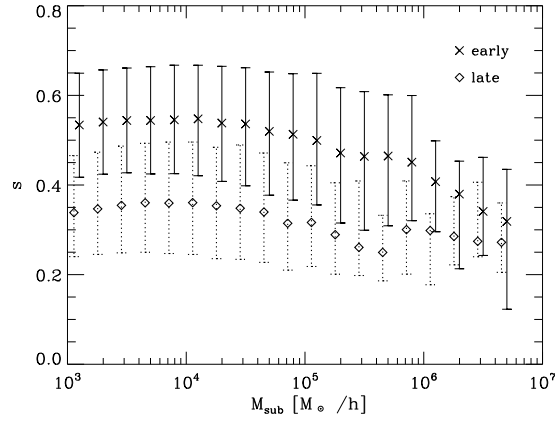
Figure 2.12: Relation between formation time and sphericity. We grouped the haloes in each mass bin into three groups. We plot the median values with error bars for early (crosses) and late (diamonds) thirds as in Fig. 2.11. We found that haloes that formed later (young haloes) are less spherical due to recent mass accumulation.
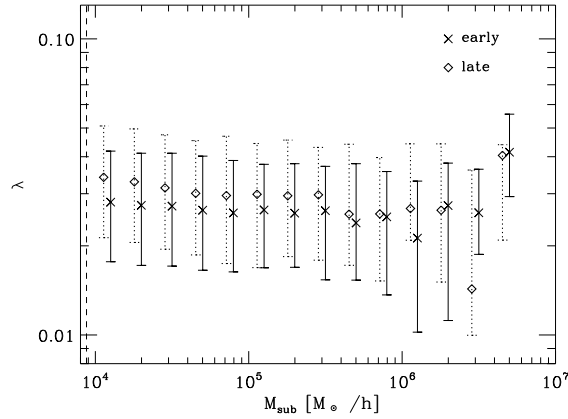
Figure 2.13: Relation between formation time and spin parameter. We grouped the haloes in each mass bin into three groups. We plot the median values with error bars for early (crosses) and late (diamonds) thirds as in Fig. 2.11. We found that haloes that formed later (young haloes) have higher values of spin parameter due to recent mass accumulation. The dashed vertical lines represent lower mass limit of 1000 particles.

Hamilton (1993),

$$\xi(r) = \frac{DD(r)RR(r)}{RD(r)^2} - 1, \tag{2.12}$$

where $DD(r)$, $RD(r)$, $RR(r)$ stand for, respectively, the number of pairs with separation r in the simulated halo catalogue (halo-halo pairs), the simulated halo catalogue and random catalogue (halo-random point pairs), and just the random catalogue (random point-random point pairs). The statistical errors are estimated through $RR(r)\sqrt{DD(r)}/RD(r)^2$.

The two-point correlation functions for haloes in the mass bin $10^{5\pm0.2}\,\mathrm{M_\odot}$ and $10^{4\pm0.2}\,\mathrm{M_\odot}$ are depicted in Fig. 2.14 as a function of separation in units of comoving h^{-1}kpc. As in Section 2.3.5, we sorted dark matter haloes in both mass ranges into three subsets according to their spin. We found that haloes with high spin are more clustered, which is well-known in large-scale simulations (Bett et al. 2007, Gao and White 2007), but was only investigated with relatively low resolution in much smaller scales (Davis and Natarajan 2009). This suggests that haloes that form in a clustered environment are more likely to experience tidal forces from neighbouring overdense regions, and therefore tend to have larger spin parameters.

2.4 Conclusions

In this paper, we have performed a high-resolution numerical simulation of structure formation up to the high redshift $z = 15$, inside a simulation box of side-length $1\,h^{-1}$Mpc. Exploiting our good statistics and resolution, we made high precision measurements for a variety of global physical parameters of haloes and demonstrated correlations between some of these properties. We clarified the characteristics of dark matter mini-haloes by comparing the results of our high-resolution simulation with works found in the literature on more massive haloes and at lower redshift ($z < 6$), and with results from our own moderate-resolution complementary simulation within a cubic region of $100\,h^{-1}$Mpc on a side that we evolved until $z = 0$. Our main findings are as follows.

1. Dark matter haloes found in our simulations have a distribution of spin parameters that is well fitted by a log-normal function around $\bar{\lambda} = 0.0262$, with dispersion $\sigma_\lambda = 0.495$. This value for $\bar{\lambda}$ is similar to the value ~ 0.03 obtained by studying more massive objects at $z \sim 0$ (e.g. galaxy clusters). The dimensionless spin parameter λ is somewhat sensitive to resolution, and hence our measurement of this quantity is by far the most accurate thus far for the mass scales investigated in this work.

2. We have shown explicitly from output of our simulations and merger trees constructed from them that the formation time of dark matter haloes, defined as the time at which the most massive substructure in a FOF halo reaches half of its final mass, only weakly depends on halo mass over about four orders of magnitude (e.g. mass scales of $\sim 10^3$–$10^7\,\mathrm{M_\odot}$). At larger mass scales, structures are known to form in a hierarchical fashion (formation redshift is a monotonically
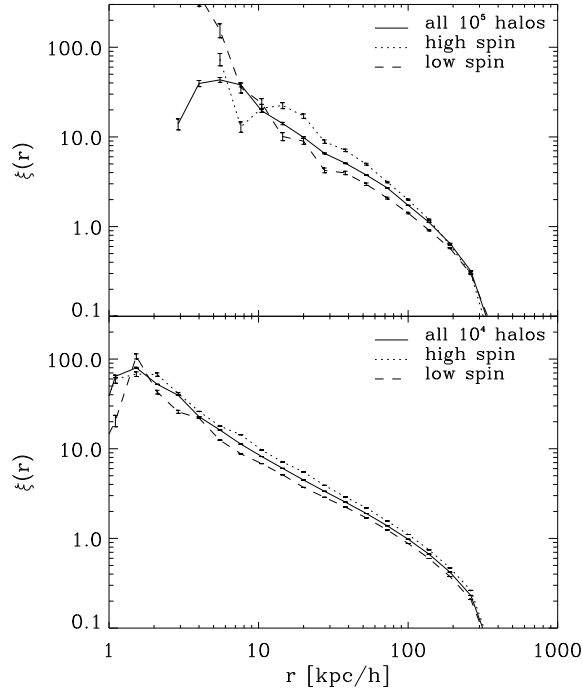
Figure 2.14: Two-point correlation function for dark matter haloes in the mass range $10^{5\pm0.2}\,h^{-1}\mathrm{M}_\odot$ and $10^{4\pm0.2}\,h^{-1}\mathrm{M}_\odot$. Distance is in units of comoving h^{-1}kpc. We have reproduced the trend seen in previous works that high spin haloes are more highly correlated than low spin haloes.

decreasing function of halo mass). But on the mass scales investigated here, this at least partially breaks down. The weak dependence of the formation time on mass is a result of the slope of the power spectrum of density perturbations at this scale, where it becomes close to the critical value of -3 for which all mass perturbations are expected to collapse simultaneously. The scatter in formation time is ~ 10 Myr.

3. The shapes of haloes are much less spherical and more highly prolate than haloes found at $z \sim 0$. The most frequent value of the sphericity parameter lies between 0.4 and 0.45. This could be due to more frequent mergers at high redshift. The majority of haloes have triaxiality parameter > 0.9. More massive haloes are more likely to be slightly less spherical and slightly more filamentary (prolate).

4. We have also investigated the relationship between formation time and halo properties such as shape, virial ratios, and spin which was not studied previously for the scales examined here. On average, haloes that formed more recently (young haloes) have higher values of the virial ratio, are less spherical, and have higher values of spin when observed at $z = 15$. This can be understood because the time passed between the formation of these young haloes and the end of the simulation is less than the relaxation time, $t_{\mathrm{relax}} \sim 60$ Myr, of these haloes.

5. Although not expected from excursion set theory, we find that haloes with high spin are more strongly clustered, where clustering is quantified by the two-point correlation function of the positions of different dark matter haloes. This could mean that haloes born in clustered environments experience stronger tidal torques during their formation.

In this study, we have investigated broad aspects of dark matter haloes at high-redshift and found many similarities with their low-redshift counterparts. Our findings could have important implications for the baryonic component of dark matter haloes found at high-redshift. Our results on the correlation between formation time and virial ratio/shape imply that the gas component inside each dark matter halo could evolve differently depending on accretion history and the actual dynamics of accretion.

Potential caveats of our work include starting redshift of our simulations and exclusion of surface terms in estimating the virial ratios. We will briefly discuss them in the following paragraphs.

Reed et al. (2007) show that an initial redshift of 139 should be safe for studying objects at $z \simeq 7$-15. Since suppression of high sigma density peaks that result from use of first order perturbation theory and low starting redshift is known to be stronger at high redshift (Crocce et al., 2006), it is possible that we are missing some of the dark matter haloes at the high mass end, especially when studying properties such as spin parameter of them at $z \sim 25$. Due to this suppression effect, we could be underestimating the two-point correlation function and formation time of dark matter haloes as well.

It is pointed out in recent literature (Ballesteros-Paredes 2006, Davis et al. 2011) that the surface terms in virial equations are in general not negligible. Once these

terms are taken into account, dark matter haloes tend to have less excess kinetic energy. However, Davis et al. (2011) show that even after correcting for the surface terms, dark matter haloes have virial ratios that are greater than one and that increase with increasing redshift. Therefore, although we would expect a systematic decrease in the absolute values of virial ratios once we include the surface terms, our main results regarding the dependence of the virial ratio on halo mass and formation redshift should be sound.

In a future study, it would be interesting to directly follow the star formation taking place in different dark matter mini-haloes by means of hydrodynamical simulations, and to clarify how the global dark matter properties investigated here are connected to the properties of the resulting Pop III stars.

Acknowledgements

3 Improving the advection of chemical species in the Arepo code

In this chapter, we first describe the basic principles of the AREPO code and later demonstrate some minor modifications we have made to the code.

3.1 Numerical methods

AREPO is a hybrid code that uses an unstructured mesh (i.e. Voronoi tessellation) to deal with the known shortcomings of previous Eulerian and Lagrangian methods for solving hydrodynamics. While it uses a Riemann solver to solve equations that govern hydrodynamics and there are mass flows between cell surfaces, it is particle-like in that the cells themselves are allowed to move. Thus it does not suffer from the lack of fluid instabilities or the lack of mixing at surfaces between fluids of different density, which results from the use of a smoothing kernel, or have difficulty treating shocks as traditional particle-based codes. It can also deal with fluids with large bulk motions without introducing errors, unlike traditional mesh-based codes. The detailed procedures that the simulation code follows is described in the chart in Fig. 3.1 (taken from Fig. 18 of Springel 2010), so we summarise only the most important aspects in this section.

From a purely Eulerian point of view, the fundamental equations of hydrodynamics are reduced to following the evolution of the vector

$$
\boldsymbol{U} = \begin{pmatrix} \rho \\ \rho\boldsymbol{v} \\ \rho e \end{pmatrix} = \begin{pmatrix} \rho \\ \rho\boldsymbol{v} \\ \rho u + \frac{1}{2}\rho|\boldsymbol{v}|^2 \end{pmatrix},
\tag{3.1}
$$

where ρ is the mass density, $\boldsymbol{v}$ is the velocity, u is the specific internal energy, and e is the specific total energy. This vector evolves according to a continuity equation of the form

$$
\frac{\partial \boldsymbol{U}}{\partial t} + \nabla \cdot \boldsymbol{F} = 0,
\tag{3.2}
$$

where the flux function $\boldsymbol{F}$ is given by

$$
\boldsymbol{F}(\boldsymbol{U}) = \begin{pmatrix} \rho\boldsymbol{v} \\ \rho\boldsymbol{v}\boldsymbol{v}^T + P \\ \rho(\rho e + P)\boldsymbol{v} \end{pmatrix}.
\tag{3.3}
$$

In understanding how this moving-mesh code works, it is important to know that there are two kinds of variables defined for each cell: 'primitive' and 'conserved'. Primitive quantities here include the density ρ, the velocity $\boldsymbol{v}$, and the pressure $P = (\gamma - 1)\rho u$ (ρ, $\boldsymbol{v}$, P). These quantities determine the state of each cell, and they are used for solving the Riemann problem. Conserved quantities, namely, the mass, the momentum, and the energy, are obtained by integrating vector $\boldsymbol{U}$ (defined in equation (3.1)) over the volume of the cell. By solving the Riemann problem at cell faces, we can calculate the change in conserved quantities. Simply put, the following procedures are what is taking place at every timestep to follow the evolution of vector $\boldsymbol{U}$ inside the code (according to a paragraph in section 3 in Springel 2010, notations similar):

1. Construct a new Voronoi tessellation based on the current coordinates of the mesh-generation points. From this, conserved quantities for each cell can be calculated.

2. From conserved quantities calculate the primitive quantities (ρ, $\boldsymbol{v}$, P) for each cell.

3. Estimate the gradients of the primitive quantities (ρ, $\boldsymbol{v}$, P).

4. Assign velocities to the mesh-generating points.

5. Use the Courant condition to determine appropriate timestep (divide radius of the cell by its sound speed to obtain a timescale).

6. For each surface between cells, compute the flux from the left and the right states of the face (solve the Riemann problem).

7. For each cell, update the conserved quantities.

8. Move the mesh-generating points with their assigned velocities for this timestep.

When we started working with the subroutine to solve primordial chemical reactions in AREPO, the code could already advect the species when the cells moved. This gave an approximately correct solution, but it did not account for the flux of species from cell to cell. Therefore we decided to make modifications to include this effect. Of course, already in the main body of AREPO, the fundamental quantities such as the mass, the momentum and the energy are properly calculated with fluxes from neighbouring cells taken into account (as described in the above procedure), but the abundance of chemical species that is transported to the neighbouring cell with the flow was neglected in the original setup. We describe here the details of the modifications we made to the code to account for this effect. Technically, the primordial chemical reactions are calculated inside a subroutine which is called at the end of each loop, after the second gravitational half kick is applied (Fig. 3.1). In the next section, we describe two technical (numerical) difficulties we have experienced, and the code fixes to get around such problems. These are both related to the computation of fluxes between neighbouring cells (step (6), (7) in the above diagram). The primordial
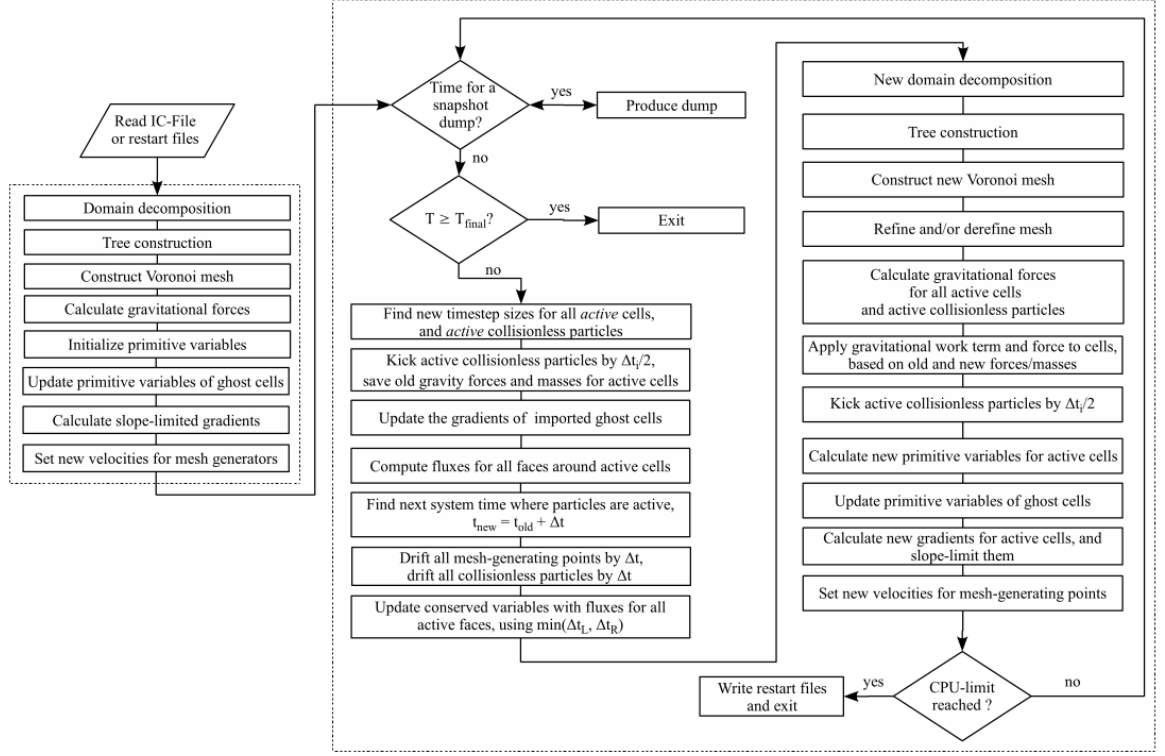
Figure 3.1: Flow chart of the simulation code: Figure taken from Springel (2010)

chemical network solver used here includes $H_2, H^+, D^+, HD, He^+, He^{++}, H, D, He, e^-$. Inside the code, two quantities relevant for each chemical species are stored. The intensive variable, 'abundances', and the extensive value, 'total amount of each chemical species (= cell mass × abundance of that species)' (hereafter, 'conserved abundances' for clarity). It is customary in the field of simulations with chemistry to normalise the 'abundance' of each chemical species by the number of protons. For example, in case of gas that consist purely of hydrogen atom (H) and helium atom (He), the abundance is $f_H = 0.76$ and $f_{He} = (1 - 0.76)/4 = 0.06$, respectively. By using this definition of abundances, the 'conserved abundances' inside each cell will be described simply by $m_i f_{x,i}$, where m_i is the mass of cell i, and $f_{x,i}$ is the abundance of chemical species x in cell i.

Technically, solving fluid equations numerically and the chemical reactions that are coupled to them simultaneously is a challenging task, since chemical reactions usually proceed much more quickly than the motion of the fluid. We briefly describe the methods adopted in our work here. If we represent the mass density of the chemical species i by ρ_i, the continuity equation for this species reads

$$\frac{\partial \rho_i}{\partial t} + \nabla \cdot (\rho_i \boldsymbol{v}) = C_i - D_i, \tag{3.4}$$

where C_i and D_i represent the source and sink terms of chemical species i due to chemical reactions. Timescales associated with source/sink terms are shorter than the the advection timescale. Therefore, when we solve the set of equations numerically, we use operator splitting, and solve the continuity equation without source or sink terms (equation (3.5)) separately from chemical rate equations (equation (3.6)).

$$\frac{\partial \rho_i}{\partial t} + \nabla \cdot (\rho_i \boldsymbol{v}) = 0 \tag{3.5}$$

$$\frac{d\rho_i}{dt} = C_i - D_i \tag{3.6}$$

After operator splitting, chemical rate equations can be solved by subcycling, with standard ordinary differential equation (ODE) solvers, as described for example in Greif et al. (2011, 2012). Technical challenges in this project involve the estimate of abundances of chemical species at cell surfaces and the estimate of fluxes between the cells, as we describe in the next section.

3.2 Technical challenges

In short, we have used the gradient estimation of scalar values inside the code, and estimated the chemical abundances of each species at the surface of each cell. This is done by adding two correction terms to the chemical abundances at the cell centre. One term is due to the spatial gradient and the disposition between cell face and cell centre (spatial-component). The other term accounts for the fact that each cell face have velocity and represents spatial gradient of chemical species times the distance the cell face travel in half the relevant timestep (time-component). Since the number of hydrogen atoms, helium atoms, and deuterium atoms should be conserved, we normalise these values at the surface of each cell, which is a recommended method when treating advection of multi-fluid flows (Plewa and Müller, 1999). Technically, this is done by multiplying the abundance of each chemical species by the correction factor, $1/\Sigma_j f_j$ where index j runs through all the chemical species in the chemical network that contain element H, He, and D respectively. Note that for chemical species HD, normalisation is done according to D (not H). In each cycle, when flow between the cell faces are allowed (note Fig. 3.1), the chemical abundances is also transported with the flow. This is essential in order to conserve elemental abundances in the simulation domain.

One technical difficulty was that the estimate of the chemical abundances at the cell surface can become negative due to moving-mesh nature of AREPO, especially when the chemical abundances of two neighbouring cells differ drastically. This could be the case since the sum of extrapolation due to spatial gradient and extrapolation due to velocity at the cell surface can become negative. Consider for example a spherical

region abundant in chemical species i that has some bulk velocity in the direction of the arrow (Fig. 3.2), and this species has a very small abundance outside of this sphere. The shaded boundary regions inside the sphere close to the left ridge gets a negative contribution from both the fact that it is closer to chemically-poor outside regions, and also from the fact that such regions are approaching. The same problems is present also for adiabatic indexes as well in the opposite side of the ridge if the spherical regions is fully molecular and the outside regions is fully atomic, since adiabatic index changes from $\frac{7}{5}$ inside of the sphere, to $\frac{5}{3}$ outside of the sphere in an abrupt way. At the cell interfaces the estimate of the chemical abundances is forced to be 0 (adiabatic index is forced to be $\frac{7}{5}$) inside the code in such a case. This can be a problem for very artificial test cases such as the ones described in Section 3.3.1. However, in real applications of the code, we did not experience cases where this becomes a problem, since in a primordial gas that we studied with this code, the abundance of H_2 is a gradually increasing function of the density of the gas, and we do not have very sharp changes in chemical abundances. Usually, in the real applications of this code, the problem we describe in the next paragraph was more common.

Another technical difficulty arises when there is mass outflow from a cell that has abundance of chemical species i to a cell that contains a much higher abundance of that species. Consider for example the case depicted in Fig. 3.3. In the two cells illustrated, the left cell has a low abundance of chemical species i, when the right cell is much more abundant in this species. At the left side of the interfaces between two cells (L), the estimate of chemical abundance is larger than inside the left cell (cell A), since the chemical abundance is increasing as you approach cell B. The amount of chemical species transported from the left cell to the right cell is determined by this estimated value at the left (upwind) side of the interface multiplied by the mass flow calculated from Riemann solvers. In such a case, the cell attempts to advect more of that species than is present inside the cell. One simple solution would be to simply abandon extrapolation at the cell faces and simply use the abundance at the cell centre when calculating flux of chemical species (Volker Springel, private communication). In our implementation, rather than using this lower-order method, after the flux is transported between cell faces, it is checked whether 'conserved abundances' of chemical species inside a cell becomes negative, and some small yet positive floor value is enforced if this condition is not satisfied.

3.3 Results

We have performed different kinds of test calculations to test our implementation. The first series of simulations test the behaviour of AREPO cells in a simple setup, namely, when the gas density is initially uniform, and only the chemical composition is different (fully molecular inside a sphere, and fully atomic outside). For simplicity, this first series of simulations do not include cooling due to chemical species or cooling/heating due to chemical reactions. We try with two different initial conditions in this setup. The second series of simulations is a more realistic application of the code to model a collapsing gas cloud in two different setups: an isolated rotating gas cloud and a gas
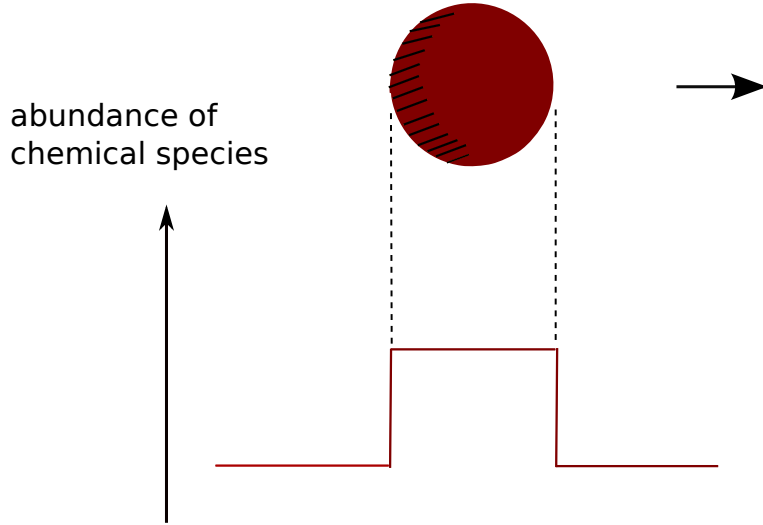
Figure 3.2: A simple example to illustrate a case where the estimate for chemical abundances/adiabatic index can be negative. The red sphere is abundant in chemical species i and is fully molecular. Everywhere outside of the sphere, there is very small abundance of this species and it is fully atomic. The sphere has a bulk velocity in the direction of the arrow. The shaded region in the red circle in the figure can get negative values.

cloud collapsing in a cosmological simulation. In total, we experiment with four kinds of test problems in this section.

3.3.1 Idealised tests

In this section, we test our implementation with two sets of test problems. Both cases involve a spherical region where hydrogen is molecular, and outside of this sphere, hydrogen is fully atomic. The main differences are for 'bulk velocity' set up, all the cells in the simulation box have a bulk velocity, whereas for 'turbulent velocity' set up, the velocity varies according to the location of the cell. The size of the simulation domain is also different for the two setups. On-the-fly refinement is not enabled for either of the two tests.

For the 'bulk velocity' setup, we placed a spherical region of fully molecular hydrogen inside a periodic box of uniform density, which is originally in pressure equilibrium with the fully atomic gas outside. The box size is 30.85 [10^{17}cm], with 100 $M_{\odot}$ inside. We have turned off **cooling due to chemical species** but not the primordial chemical network itself. All the gas cells in the box have bulk velocity in the positive x direction. We have compared abundance of molecular hydrogen for two cases with and without advection of chemical species. Note that the run with advection has 10^5 particles when the run without advection has 10^6 particles. We see that for the run with advection, the H_2 molecules are actually advected in the surrounding cell
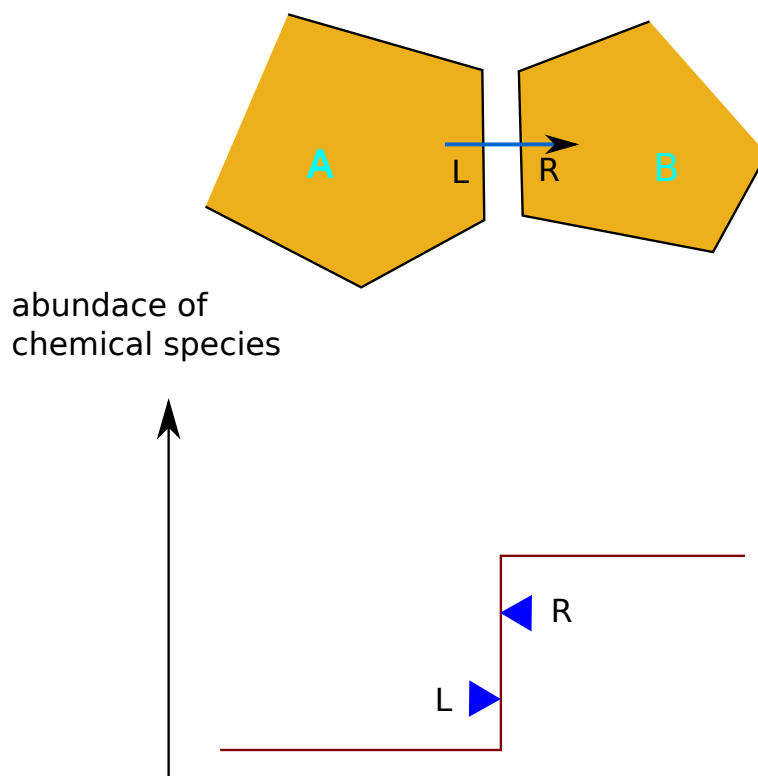
Figure 3.3: A simple example to illustrate a case where the total amount of chemical species can be negative after flux exchange. Cell A has a smaller abundance of chemical species i, when the neighbouring cell (cell B) has a much larger abundance of the same species. Assume there is mass flux into cell B from cell A. L and R represent the left side and the right side of a cell face described here. The blue triangles represent the estimated abundance of some chemical species according to gradient of chemical abundances at cell faces L and R, respectively. Note that the estimated abundance at L, which is used to calculate the amount of chemical species transported from cell A to cell B, is larger than the abundance in the centre of cell A, which is represented by the left lower plateau in the figure.

(Figs 3.4 and 3.5).

For the 'turbulent velocity' setup, we placed a spherical region of fully molecular hydrogen inside a periodic box of uniform density, which is originally in pressure equilibrium with the fully atomic gas outside. We have switched off both **cooling due to chemical species** and **primordial chemical network** in this run. Therefore, 'conserved abundances' for each of the species should be conserved inside the simulation box. We have used an initially uniform density distribution, with 10^6 particles that represent total mass of 100 $M_\odot$, inside the simulation box of length 10 $[10^{17}\text{cm}]$. Initially, the gas cells have turbulent velocity with velocity power spectrum $P(k) \propto k^{-4}$, scaled such that $E_{\text{grav}}/E_{\text{kin}} = 0.5$ where E_{grav} and E_{kin} represent the gravitational potential energy and the kinetic energy, respectively. We have compared molecular hydrogen abundance for two cases with and without cell-to-cell advection of chemical species (Figs 3.6 and 3.7). The error in 'conserved abundances' of H_2 is demonstrated in Fig. 3.8 for the calculation without cell-to-cell advection of chemical species (the error for calculation with cell-to-cell advection is 0 within machine precision for the time range presented here). Here, the error is defined as

$$\Delta_{\text{H}_2} = \frac{(\sum_i m_i f_{\text{H}_2,i})_t - (\sum_i m_i f_{\text{H}_2,i})_0}{(\sum_i m_i f_{\text{H}_2,i})_0}, \tag{3.7}$$

where the sum is taken for all the cells inside the simulation domain, m_i represents the mass of the cell, and $f_{\text{H}_2,i}$ represents the abundance of H_2 in the cell. Fig. 3.8 shows that at the point we stop our test calculation, $\sim 10^{-2}$ of the initial amount of H_2 was 'generated' artificially by not accounting for flux of chemical species between moving cell surfaces. This is a pretty big error—order of 5 larger than the round-off error even for single precision calculation.

3.3.2 Collapse tests

In this section, we test our implementation with two different sets of initial conditions: an isolated collapsing gas cloud and a gas cloud taken from cosmological hydrodynamical simulations. The initial condition for the isolated run use 10^6 particles with total mass of ~ 2700 $M_\odot$, with solid body rotation around the z-axis (constant angular velocity $\omega = 8.5 \times 10^{-16}$ s^{-1}), and an initial temperature of 100 K. The box size is 227.71 $[10^{17}\text{cm}]$. The particle distributions are created such that it has a Bonnor-Ebert sphere like density profile (but not exactly a Bonnor-Ebert sphere since we did not set external pressure). The initial central number density is $\sim 3.7 \times 10^6$ cm^{-3}. On-the-fly refinement is not enabled for the isolated run. We have also tested the validity of the code in a fully cosmological setup, which is mostly similar to the setup described in Section 4.2 (number of cells per Jeans length is 64 and the dark matter particle number is 256^3 here). The isolated run is stopped at number density of $\sim 10^{15}$ cm^{-3} whereas the cosmological run is stopped at $\sim$ several times 10^7 cm^{-3}.

As shown in Fig. 3.9, for a simple setup, there is little difference with and without cell-to-cell advection of chemical species. This is to be expected, since there should be little advection of mass or chemical species from cell to cell in this case—the cells follow the ordered flow.
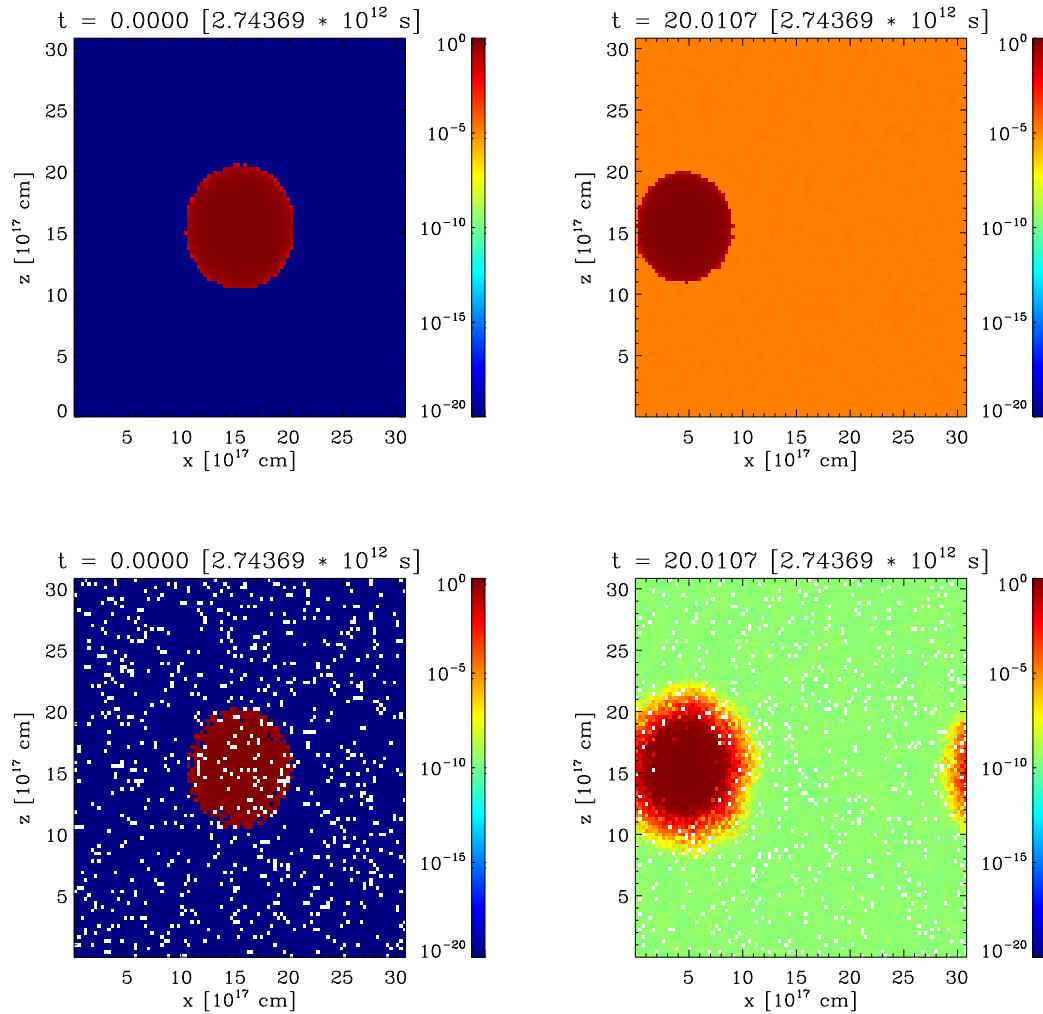
Figure 3.4: Map of mass-weighted hydrogen fraction f_{H_2} where all the cells have initial bulk velocity in the positive x direction (visualisation for a slice with thickness of a quarter of the box length). The columns correspond to two different output times (in the beginning of simulation, and when the blob has travelled through the periodic box in the x-direction and appeared again at left side of the panel). The upper (lower) row corresponds to test calculation without (with) cell-to-cell advection. The H_2 map with cell-to-cell advection of chemical species is more noisy due to lower particle numbers.
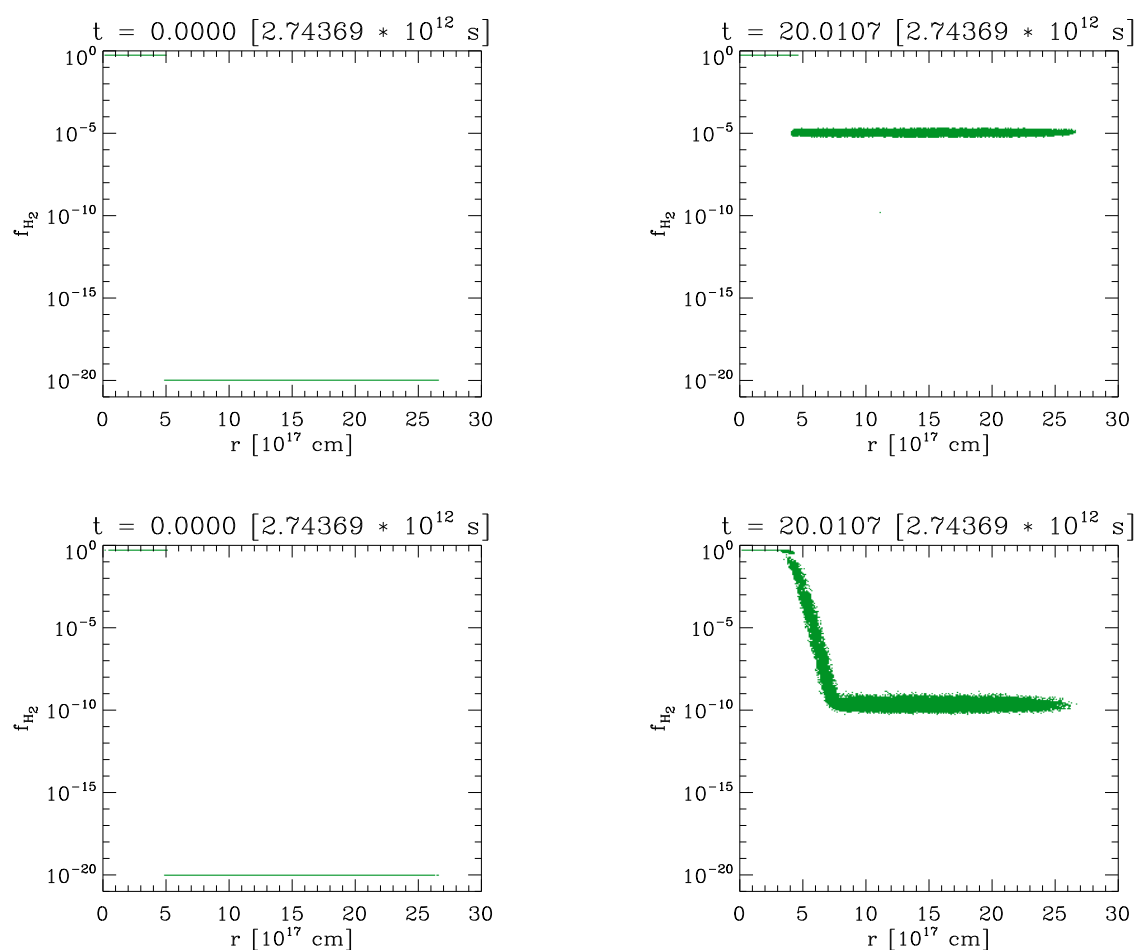
Figure 3.5: Radial profile of H$_2$ abundance (f_{H_2}) for 'bulk velocity' test calculation. Density profiles presented here correspond to density projections shown in Fig. 3.4
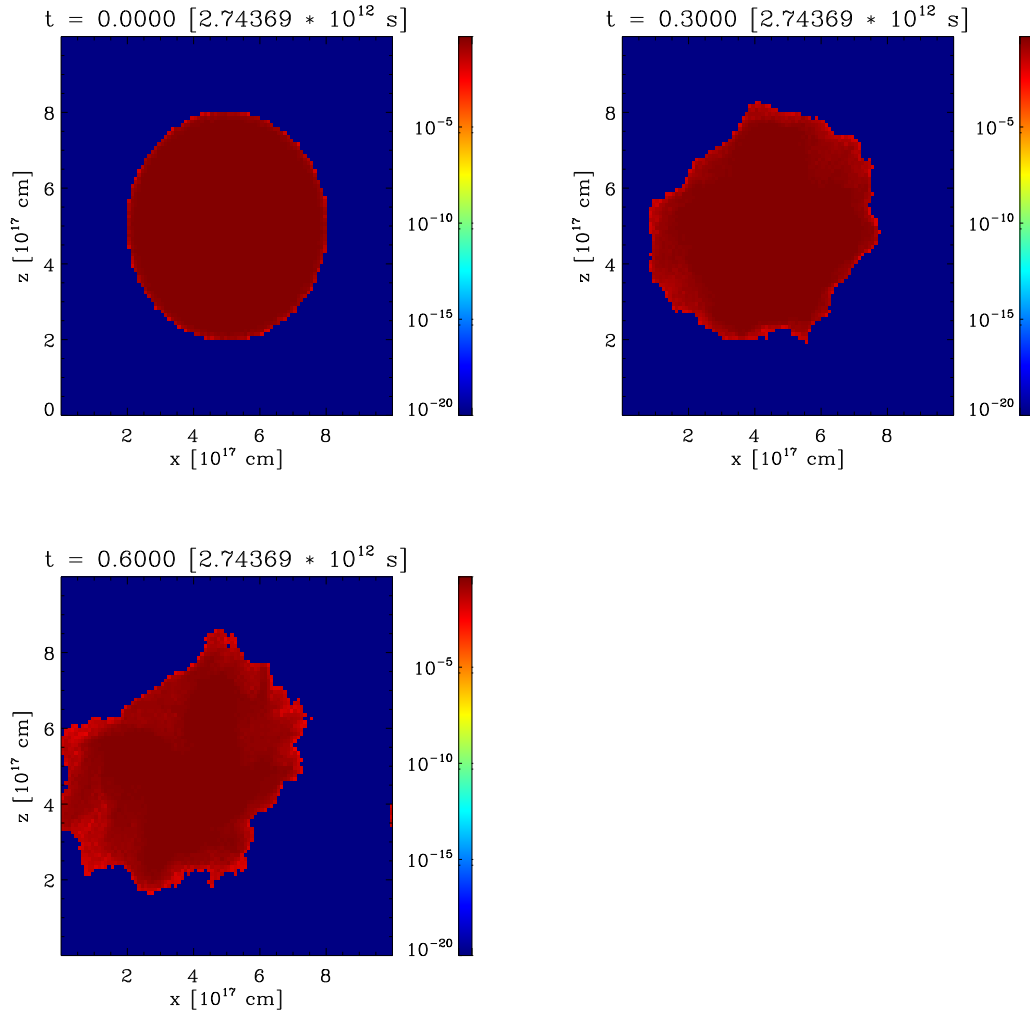
Figure 3.6: Time sequence of mass-weighted H_2 abundance (f_{H_2}) map for 'turbulent velocity' test calculation without cell-to-cell advection of chemical species. The slice has a thickness of one quarter of the box length.
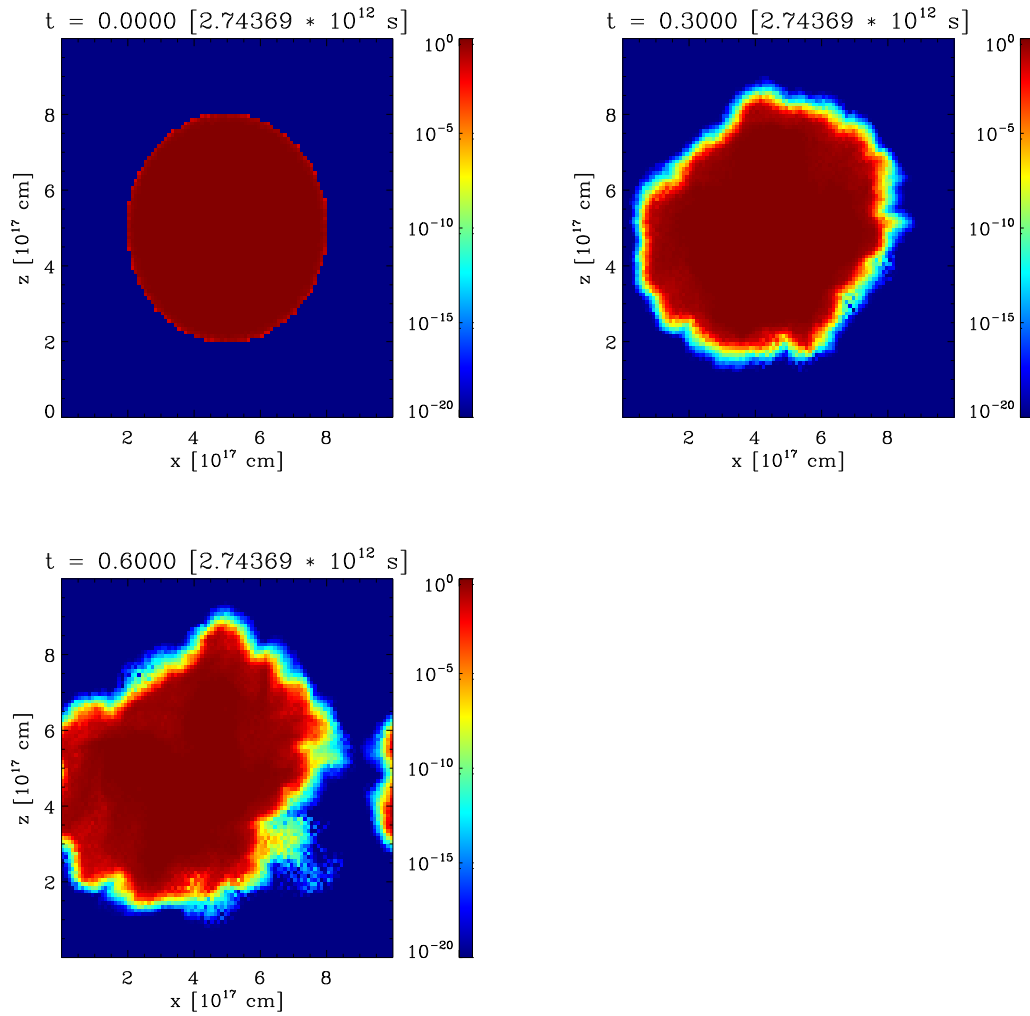
Figure 3.7: Time sequence of mass-weighted H_2 abundance (f_{H_2}) map for 'turbulent velocity' test calculation with cell-to-cell advection of chemical species. The slice has a thickness of one quarter of the box length.
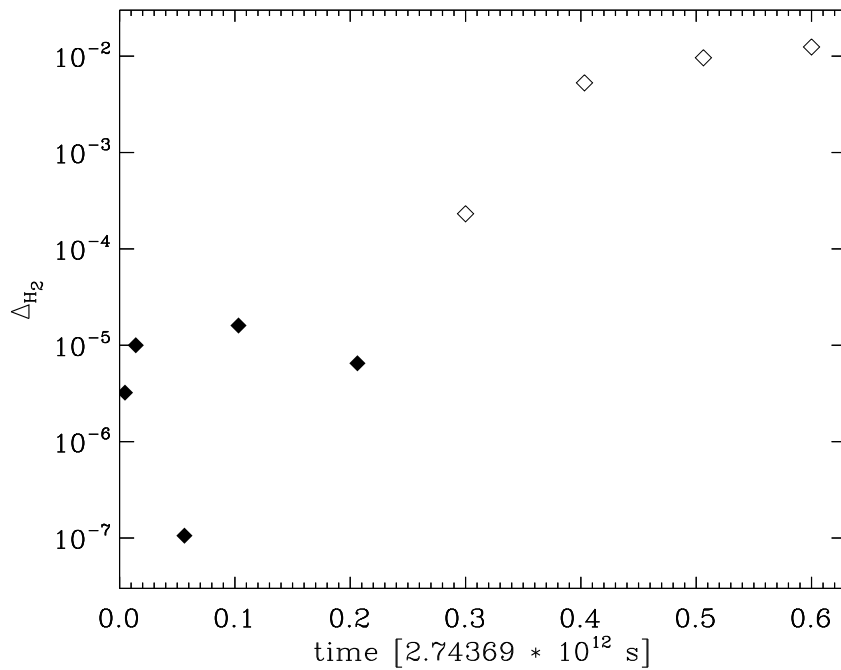
Figure 3.8: The fractional error in the total amount of H$_2$, Δ_{H_2} (defined in equation (3.7)), plotted as a function of time in simulation units for calculations without cell-to-cell advection of chemical species. Within the time range plotted here, the error in total amount of H$_2$ was 0 within machine precision for the case including cell-to-cell advection. The absolute values of the fractional error are shown in the y-axis. Negative values are represented by filled diamonds, while positive ones are represented by empty diamonds.
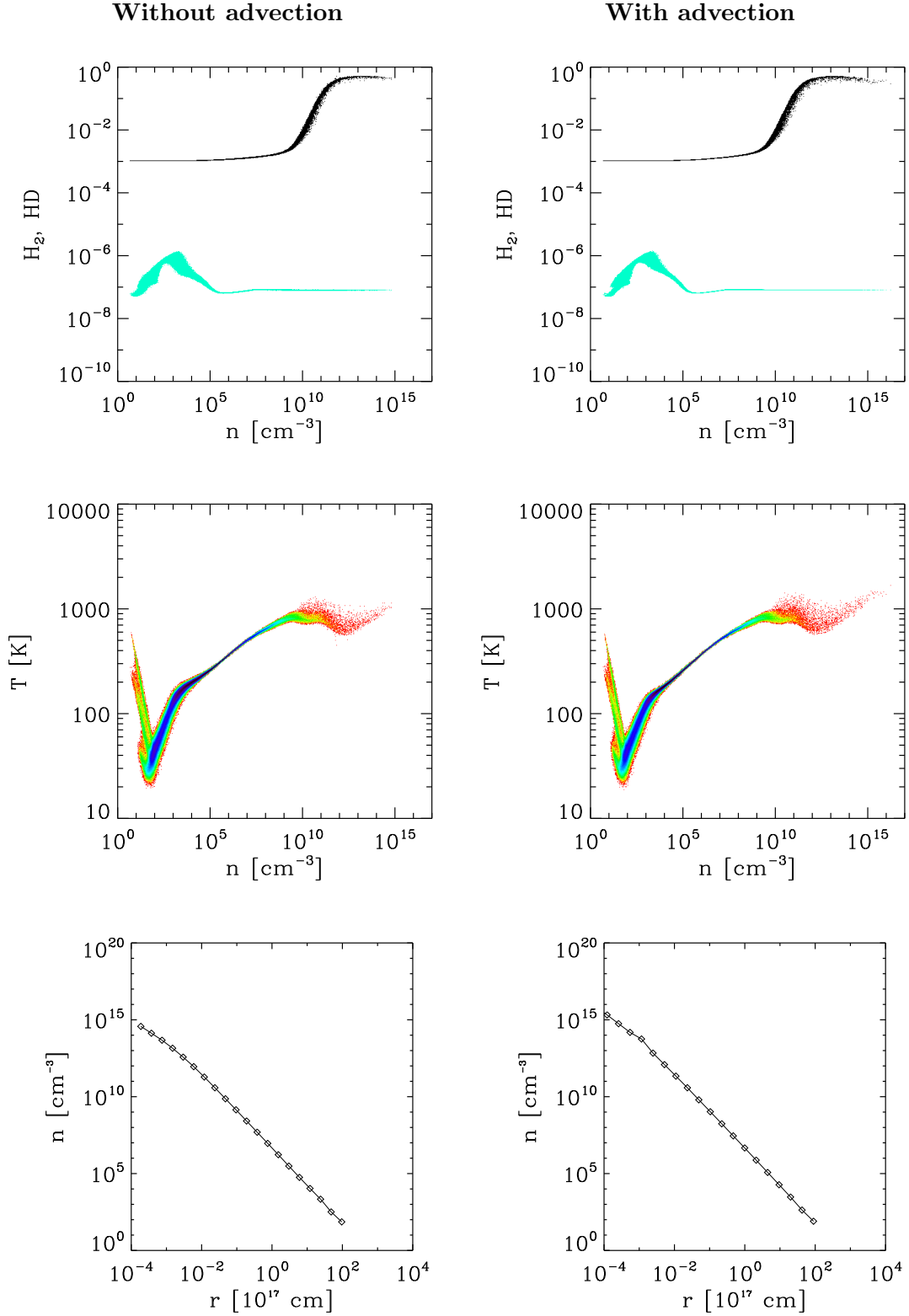
Figure 3.9: Comparison of chemical abundances f_{H_2} (black), f_{HD} (turquoise), ρ-T diagram, density profile of simulation with (right column) and without (left) advection for an isolated gas cloud with initially solid body rotation. For regions with $n < 10^4$-10^5 cm^{-3}, we see the influence of the initial conditions. However, the behaviour of the gas at higher densities is a result of gravitational collapse.
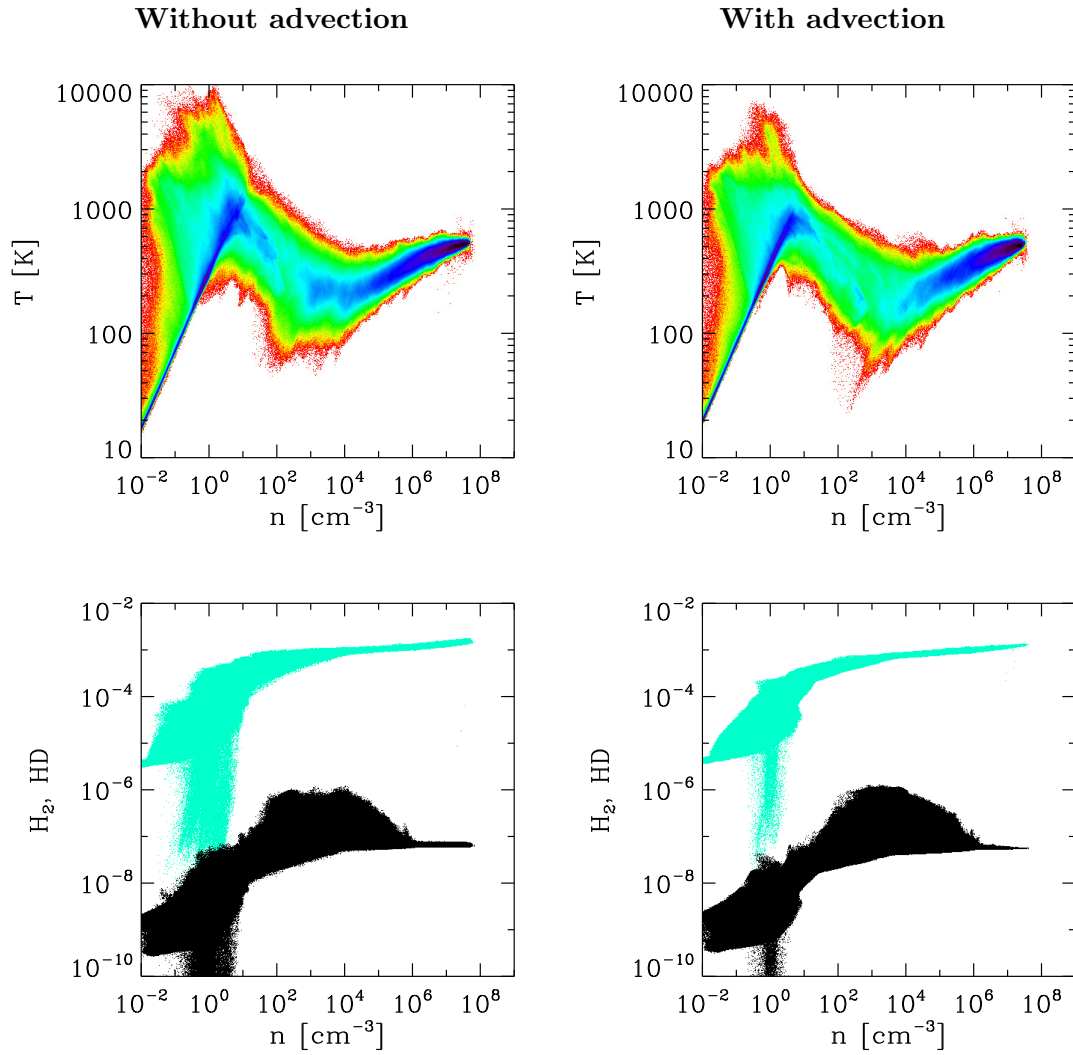
Figure 3.10: Comparison of chemical abundances f_{H_2} (turquoise), f_{HD} (black), ρ-T diagram, with (right column) and without (left) cell-to-cell advection in a cosmological setup.

As shown in Fig. 3.10, for a realistic cosmological initial condition, where there is more turbulent motions and therefore more flux between cell surfaces, introduction of cell-to-cell advection of chemical species makes a noticeable difference; it results in a more tight correlation between density and f_{H_2} or f_{HD}. There is also less scatter in the ρ-T diagram.

4 Criterion for the formation of HD in the early universe

4.1 Introduction

In primordial gas, which consists of only light elements produced by cosmic nucleosynthesis such as hydrogen, deuterium, helium and lithium, the elements responsible for most of the cooling in the local ISM (C, O, Si etc.) are absent. In such an environment, the hydrogen molecule (H_2) is the most important coolant. However, cooling due to H_2 is inefficient at low temperatures (T $<$ 200 K) because its lowest energy rotational transition has an energy of $E/k_B \sim 512$ K. On the other hand, its deuterated analogue, HD is able to cool the gas down below 100 K because its lowest accessible rotational transition occurs at much lower energy, $E/k_B \sim 130$ K. In the low density primordial gas, $[HD/H_2]$ is much larger than the cosmic ratio of $[D/H]$ $\sim 2.6 \times 10^{-5}$, obtained from absorption features in the spectra of distant systems (Burles and Tytler, 1998). This phenomenon is known as fractionation and arises due to the temperature dependence of the chemical reaction rates, which we will describe below. The chemical reactions that governs the abundance of HD are (Galli and Palla 1998, Galli and Palla 2002):

$$H_2 + D^+ \rightarrow HD + H^+ \tag{4.1}$$

$$HD + H^+ \rightarrow H_2 + D^+. \tag{4.2}$$

The destruction process of HD is slow at low temperatures because of its endothermic nature, so the abundance of HD is boosted at low temperatures. In equilibrium, the HD-to-H_2 ratio follows

$$[HD/H_2] = 2 \exp\left[\frac{464}{T}\right] [D/H]. \tag{4.3}$$

If sufficient amount of H_2 is present and the gas is cooled enough, then according to equation (4.3), HD abundance is boosted (in other words, reaction (4.1) is favoured), which allows the gas to cool even farther. Since the Jeans mass, the amount of mass necessary for gas clouds to become dynamically unstable (discussed in Section 1.9), changes as a function of density and temperature, how much HD forms in the early universe, and thus the extent to which primordial gas is able to cool and reduce its Jeans mass has a critical importance for the mass spectrum of the first generation of stars. However, there is also an opposing view about the role that HD plays in primordial star formation (Clark et al., 2011a), stating that more HD leads to less fragmentation. The latter adopts two sets of initial conditions to model two different

groups of Pop III stars, and since the initial conditions for the HD-rich case start from a higher abundance of electrons and ionized medium than in truly primordial cases, they are probing a slightly different regime than investigated here; thus care should be taken when comparing the results.

Since the very early works of Abel et al. (2002), Bromm et al. (2002), and Yoshida et al. (2003) many attempts have been made to numerically model the formation of protostars (Bromm, 2013). It is now known that the mass of protostars has some scatter and is different from halo to halo (for example, O'Shea and Norman, 2007). If we consider all the works aimed to follow the formation of Pop III protostars to date, many experiments have been performed to sample the whole spectrum of Population III (Pop III) stars. There are also some works that focus on the role that HD molecules play in the process of primordial star formation (Ripamonti, 2007; McGreer and Bryan, 2008). However, very few cosmological hydrodynamic simulations to date are dedicated to answer the simple question, 'what determines the amount of HD that forms during protostellar collapse?'.

HD is known to form in primordial gas that has a higher than usual abundance of electrons, such as in pristine gas clouds that have been exposed to the UV photons from previous generations of star formation. This is because the reaction (4.1) proceeds faster for highly ionized medium, and higher ionisation facilitates H_2 formation by reaction (4.4), which results in lower temperature, which leads to an increase in HD abundance (according to equation (4.3)).

$$
\begin{align}
H + e^- &\rightarrow H^- + \gamma \tag{4.4} \\
H^- + H &\rightarrow H_2 + e^- \tag{4.5}
\end{align}
$$

In the case of the 'very first' Pop III stars to form, or Pop III stars that form in locations where there are no previous history of star formation, there is no radiation emitted by previous generation of stars. Under such conditions, HD was believed to form only in gas experiencing shocks such as when the dark matter haloes are merging. This idea was proposed by Shchekinov and Vasiliev (2006) and investigated by numerical experiment by Bovino et al. (2014), who compare primordial gas collapse taking place in an isolated halo and in a halo experiencing violent merging events.

However, according to our inspection of the density maps of collapsing gas inside our cosmological simulations, we found no evidence of gas clumps colliding with each other out of 10 realizations. We conclude that the gas clouds that experience collisions with neighbouring gas clumps during their collapse (as investigated by Bovino et al. 2014) are very rare in number, and are in no way representative of numerous samples of dark matter haloes. Hirano et al. (2014) hints that the rotation of primordial gas delays collapse and thus allows for primordial gas to cool sufficiently, and form HD. They resort to comparison with one-zone simulations to make this point.

In this work, we ran many samples of moderate-resolution 3D cosmological hydrodynamical simulations, and without further assumptions, try to discover simple physical criteria that accounts for the abundance of HD molecules in primordial mini-haloes.

4.2 Numerical methods

The initial conditions of our simulations presented here are generated in the following way: First, we ran collisionless N-body simulations with 1 Mpc/h comoving in length with uniform mass resolution to capture collapsing dark matter haloes starting at $z=100$. We employ cosmological parameters consistent with the WMAP-7 measurements ($\Omega_m = 0.271$, $\Omega_\Lambda = 0.729$, $\sigma_8 = 0.809$, $h = 0.703$; Komatsu et al., 2011)[1] These collisionless simulations were executed with Gadget-3 (Springel et al., 2005). From this parent simulation, we generate a new set of initial conditions (zoom-in ICs) with finer dark matter resolution at the region of interest, where a specific mini-halo identified by friends-of-friends method that is present at the end of the parent simulation is located. The selected dark matter halo is shifted to the centre of the simulation box. The regions further away from this specific halo is represented by dark matter particles with progressively lower resolution. The parent simulation contains 512^3 particles, at the regions of interest the mass of the dark matter particles are improved by 4^3 (dark matter particle mass of 7.3 $M_\odot$). The results presented in this chapter analyses simulation outputs initiated from 10 zoom-in ICs, each centred on a different FOF halo from a single parent simulation. Therefore, they represent different regions in the same cosmological box.

From this newly generated initial condition with improved dark matter resolution, we start a hydrodynamical simulation with the moving-mesh code AREPO (Springel, 2010). During start-up of our hydrodynamic simulations, the code generates gas cells from dark matter only initial conditions. In order to numerically follow the dynamics of pristine gas in a cosmological context, we adopt on-the-fly mass refinement scheme according to Jeans length (32 cells per Jeans length in the production run, 8 cells per Jeans length for lower resolution comparison run shown in Section 4.4). In order to study abundance of HD in the early stages of protostellar collapse, we stop our simulation when the maximum density in the simulation domain reaches $\simeq 10^6\,\mathrm{cm}^{-3}$. In each timestep, the time-dependent chemical network and associated heating and cooling is solved for each gas cell (see Section 3.1).

4.3 Results

This chapter is intended to clarify the difference between HD-rich and HD-poor gas clouds. In doing so, the actual definition of the amount of HD in a given gas cloud is also critical. It is better to use mass-weighted HD abundance above certain density limit than using the HD abundance of the highest abundance cell. The mass-weighted HD abundance shows good numerical convergence, when the maximum value of HD abundance of individual cells can differ by a factor of few when the refinement criterion is changed. (See also Section 4.4.) In Chapter 3, we have defined f_{HD} as a fractional abundance of HD with respect to protons. In this chapter, let us define f_{HD} as the

---

[1]We would not expect our results to differ significantly if we were to use the cosmological parameters measured by Planck (Planck Collaboration et al., 2013). This choice of parameters is for consistency with our previous work Sasaki et al. 2014, see also Chapter 2.
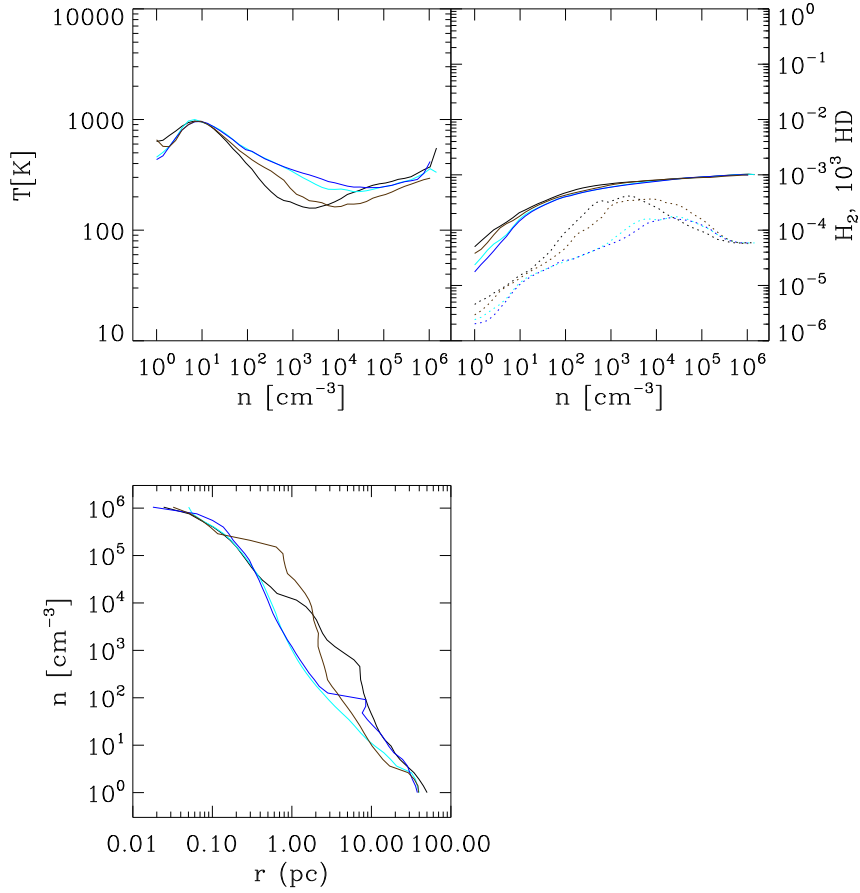
Figure 4.1: Temperatures, abundances of chemical species, and density profiles for different gas clouds. Out of 10 samples of gas clouds, black and brown lines indicate physical properties of gas clouds with the two highest values of f_{HD} (mass-weighted average of fractional HD abundance for all cells with densities $> 10^3$ cm^{-3}), and blue and cyan lines indicate those with the two lowest values of f_{HD}. Note that the gas clouds rich in HD have less smooth density profiles.

mass-average of previously defined f_{HD} over cells with densities $> 10^3$ cm^{-3}, and use it as a measure of HD-richness in each gas cloud.

In Fig. 4.1, we show the temperature, chemical abundances, and the density profile of primordial gas clouds for two most HD-rich clouds (black and brown solid lines) and two most HD-poor clouds (blue and cyan solid lines) out of 10 samples (similar color-coding is used for Fig. 4.4). We find that HD-rich clouds have lower temperature (compare densities between 10^2 and 10^5 cm^{-3}) than HD-poor clouds. We find that the density profiles for HD-rich clouds are noticeably more noisy than the HD-poor clouds. As will be shown in Fig. 4.4, they take longer time to collapse, and have allowed secondary density perturbations to grow inside the cloud. The comparison of the density maps illustrated in Fig. 4.2 and 4.3 further clarifies the morphological differences between HD-rich and HD-poor primordial collapsing gas.

We next study the evolutionary track of the densest point in the primordial gas cloud as a function of time (Fig. 4.4) to show that the speed of protostellar collapse is relevant for HD formation. Gas clouds that take longer to collapse tend to have higher HD fractions. After some numerical experiments, it is discovered that the time it takes for the central density to evolve from 10^4 cm^{-3} to 10^5 cm^{-3} is most correlated with the amount of HD that is formed. This is probably because HD is mostly formed when the density of gas is $\leq 10^5$ cm^{-3} (see Fig. 4.1). This may apparently seem as a contradiction, as more abundance of HD, or increased HD cooling could hasten the collapse. However, this is not the case. In the early phase of protostellar formation, the regime we study here, the gas is not supported mainly by thermal energy but by kinetic energy.

As shown in Fig. 4.5, there is a clear relationship between f_{HD} and the time it takes the gas cloud to collapse for the numerous haloes we have simulated, not just for the selected examples shown in Fig. 4.4.

Let us define the parameter f_{ratio} as the ratio between tangential component of velocity and the Keplerian velocity at the half-mass radius of gas particles included inside R_{200} (see Section 1.4 for definition) of a dark matter halo when the central gas density reaches 10^2 cm^{-3}. f_{ratio} defined this way characterises the spin of gas in the early stage in the gravitational collapse.

Fig. 4.6 (left) shows that the dark matter haloes in which the gas collapsed more recently are more likely to have higher mass. There seems to be little dependence of collapse redshift on f_{HD} (Fig. 4.6, right). Fig. 4.7 (left) shows that the correlation between f_{HD} and f_{ratio} is only weak. There is some physical reasons for this correlation, since the tangential component of velocity is likely to delay the collapse. The seemingly counter-intuitive positive correlation between subhalo mass and collapse time (namely, more massive subhaloes take longer time to collapse shown in Fig. 4.7, right) is most likely a reflection of the fact that the gas clouds that collapse slowly allows their host dark matter halo to grow more massive.

Rotation, however, is not the only physical process that could potentially delay the collapse of primordial gas inside dark matter mini-haloes. We find stronger positive correlation between velocity dispersion and f_{HD} (Fig. 4.8). We interpret this result such that turbulent velocity structures play more important role than rotation in delaying the collapse and allowing enough time for HD to form in collapsing primordial
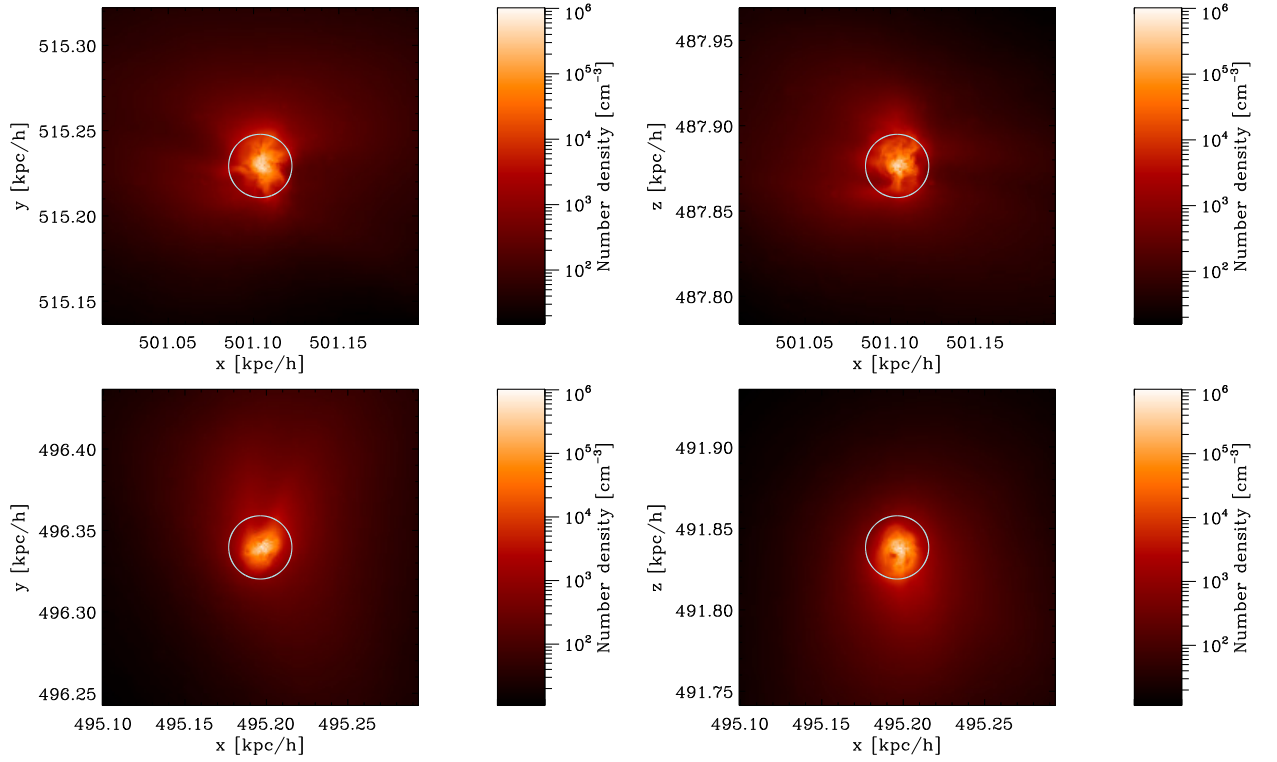
Figure 4.2: Density slice through the densest point of gas for HD-poor gas clouds at the final output time when the central density has reached 10^6 cm^{-3}. The circle indicates a radius of 1 proper pc, while the numbers on the axis indicate coordinates in comoving kpc/h. Compare with Fig. 4.3.
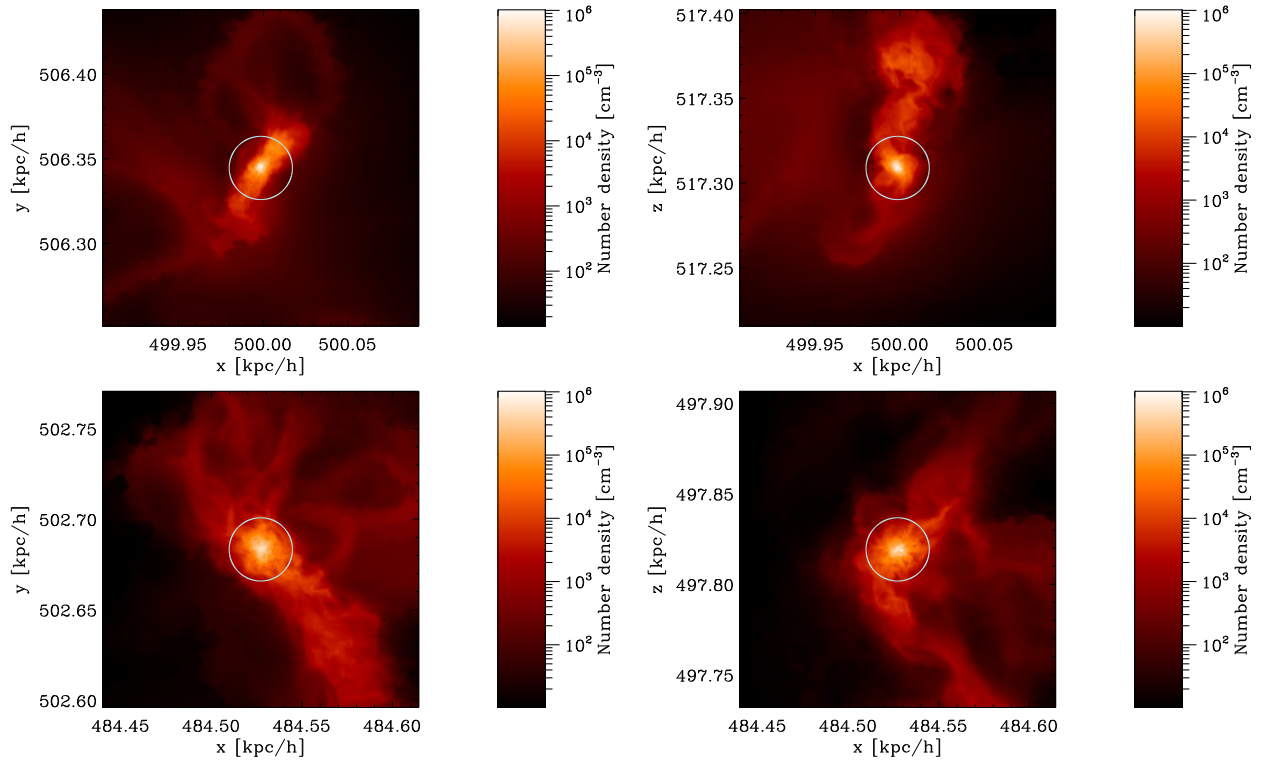
Figure 4.3: Density slice through the densest point of gas for HD-rich gas clouds at the final output time when the central density has reached 10^6 cm^{-3}. The circle indicates a radius of 1 proper pc, while the numbers on the axis indicate coordinates in comoving kpc/h. Compare with Fig. 4.2.
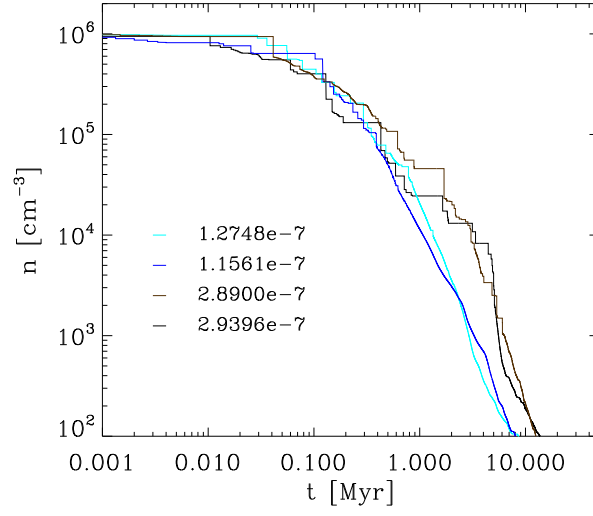
Figure 4.4: Central density of gas clouds as a function of time before collapse (origin of time is at the final time in the simulation). The numbers in the legend indicate value of f_{HD}. The clouds that result in high abundance of HD at the end of simulation (when the central density reaches 10^6 cm^{-3}) take longer time to collapse.
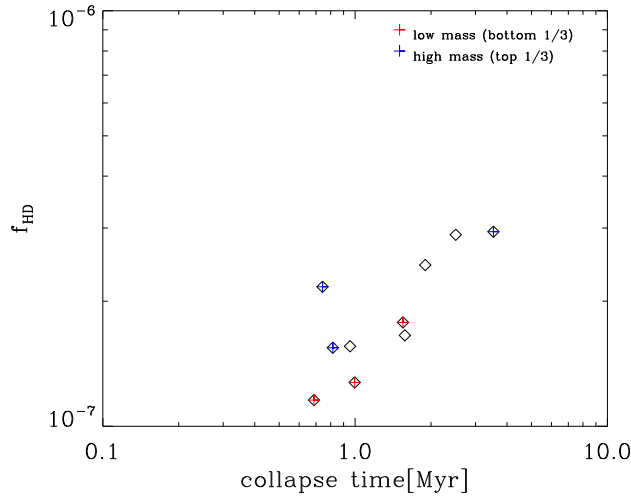
Figure 4.5: Relation between collapse time and f_{HD}. 'Collapse time' is defined as the time when the central density increases from 10^4 to 10^5 cm^{-3}.
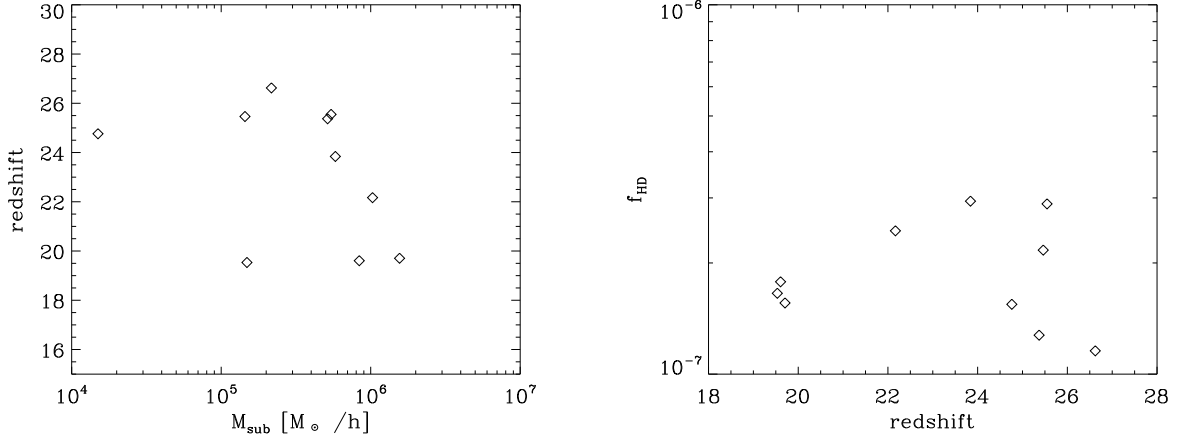
Figure 4.6: Relation between the subhalo mass and the collapse redshift (left). Relation between the collapse redshift and f_{HD} (right). All physical values are at the final output time when the maximum density of gas reaches 10^6 cm^{-3}. The collapse redshift is the redshift at the final output time.

gas clouds.

4.4 Numerical convergence

In order to confirm that the HD abundance we are measuring is stable even if we change the refinement criterion, it is important to run the same simulation with different resolution to check for numerical convergence. It is shown that as we increase the number of cells per Jeans length, the redshift at which the central gas density reaches 10^6 cm^{-3} is made slightly later in time, and the HD abundance of the highest abundance cell in a particular dark matter halo is slightly increased. As shown in Fig. 4.9, the temperature, the abundances of chemical species, and the density profile show good convergence.

4.5 Conclusion

In this chapter, by directly measuring the time it takes for the central density to reach a certain value, just from arguments based on outputs of 3D realistic cosmological hydrodynamical simulations, we have clarified that the speed of the gravitational collapse determines the amount of HD molecules in primordial gas. We have shown that disordered velocity fields play a more important role than rotation in delaying the collapse. In future work, we would like to show this in more detail.

Since this work neglects the effect of radiation from Pop III stars or the heavy elements produced by them, which becomes important after star formation starts to
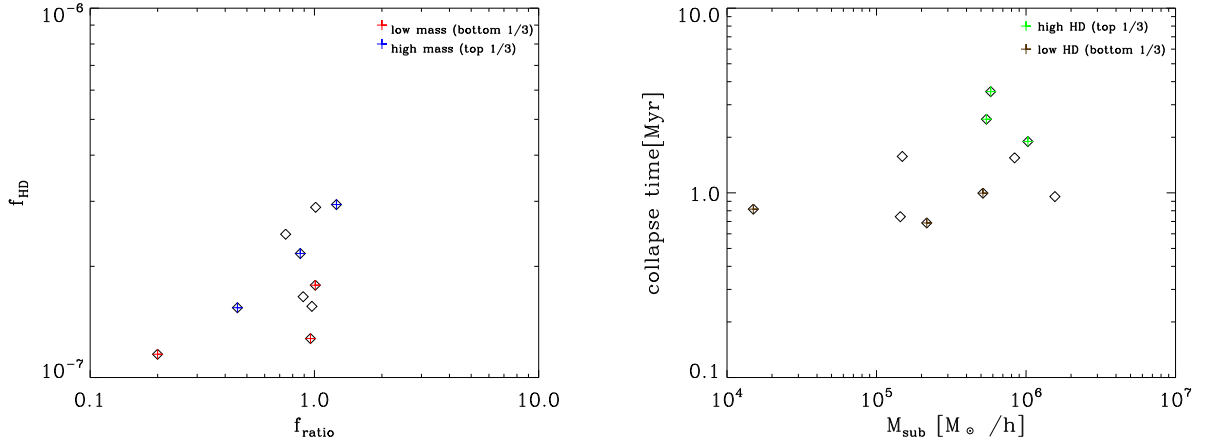
Figure 4.7: Relation between f_{HD} and f_{ratio} (left). Relation between the subhalo mass and the collapse time (right). All physical values are at the final output time, except for f_{ratio} (the ratio between tangential component of velocity and the Keplerian velocity, evaluated at the half-mass radius of gas cells inside R_{200}), which is measured when the central density reaches 10^2 cm^{-3}.
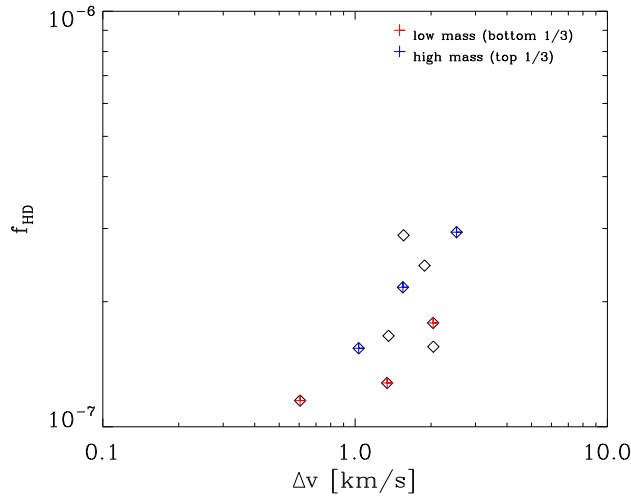
Figure 4.8: Correlation between f_{HD} and the velocity dispersion in the earlier stages of collapse (when the central density is 10^2 cm^{-3}), evaluated at the half-mass radius of gas cells inside R_{200}.
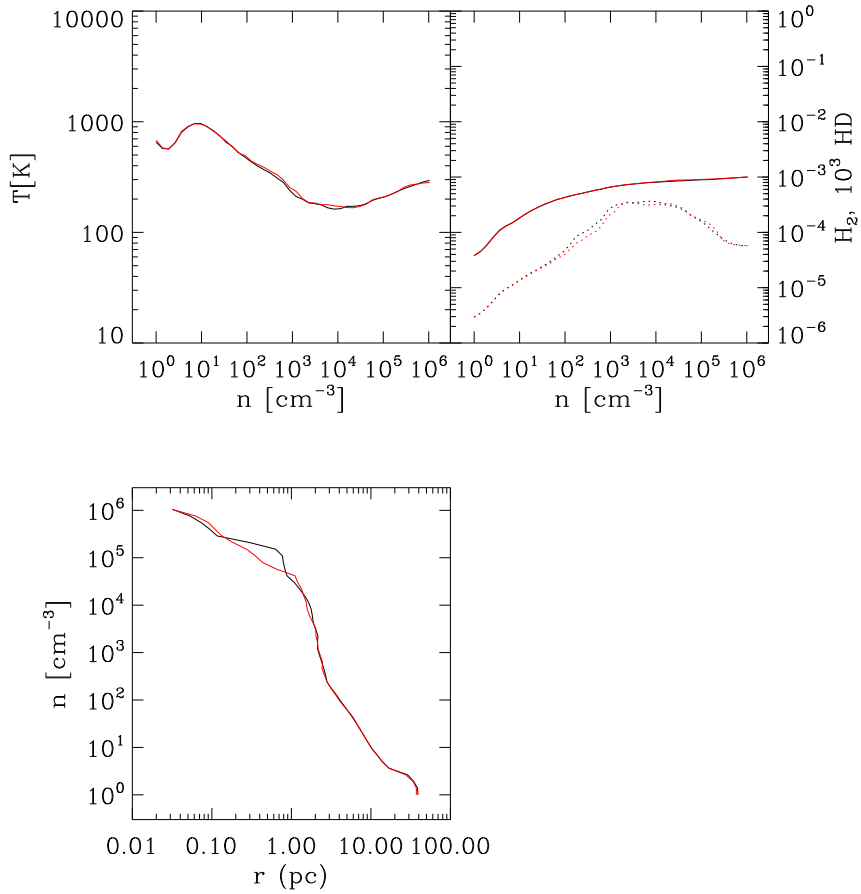
Figure 4.9: Comparison of temperature, abundances of chemical species, and density profile for the same gas cloud with different refinement criterion—8 cells per Jeans length (red solid line) and 32 cells per Jeans length (black solid line).

take place in a specific region of the universe, it is the lowest order approximation to real cosmic history, and in reality, the gas collapsing at lower redshift would be affected by the neighbouring gas clouds which have collapsed earlier in time.

5 Conclusions

In this thesis, we studied the formation of dark matter haloes and Pop III stars in the high-redshift universe. We used high-resolution N-body simulations to investigate the properties of dark matter mini-haloes found at redshifts $z \geq 15$ and to quantify the differences between these haloes and their more massive lower-redshift counterparts. Using the moving-mesh code AREPO, which we modified according to our needs (described in Chapter 3), we studied primordial gas initiating gravitational collapse in dark matter mini-haloes. By comparing multiple samples of collapsing gas clouds from cosmological simulations, we sought to find out what determines the amount of HD molecules that forms in primordial gas. Our scientific findings are summarised in two parts, corresponding to chapters 2 and 4 respectively.

5.1 Small-scale structure formation

- Dark matter haloes found in our simulations have a distribution of spin parameters that is well fitted by a log-normal function around $\bar{\lambda} = 0.0262$, with dispersion $\sigma_\lambda = 0.495$. This value for $\bar{\lambda}$ is similar to the value ~ 0.03 obtained by studying more massive objects at $z \sim 0$ (e.g. galaxy clusters). The dimensionless spin parameter λ is somewhat sensitive to resolution, and hence our measurement of this quantity is by far the most accurate thus far for the mass scales investigated in this work.

- We have shown explicitly from output of our simulations and merger trees constructed from them that the formation time of dark matter haloes, defined as the time at which the most massive substructure in a FOF halo reaches half of its final mass, only weakly depends on halo mass over about four orders of magnitude (e.g. mass scales of $\sim 10^3$–$10^7 \, \mathrm{M_\odot}$). At larger mass scales, structures are known to form in a hierarchical fashion (formation redshift is a monotonically decreasing function of halo mass). But on the mass scales investigated here, this at least partially breaks down. The weak dependence of the formation time on mass is a result of the slope of the power spectrum of density perturbations at this scale, where it becomes close to the critical value of -3 for which all mass perturbations are expected to collapse simultaneously. The scatter in formation time is ~ 10 Myr.

- The shapes of haloes are much less spherical and more highly prolate than haloes found at $z \sim 0$. The most frequent value of the sphericity parameter lies between 0.4 and 0.45. This could be due to more frequent mergers at high redshift. The majority of haloes have triaxiality parameter > 0.9. More massive haloes are more likely to be slightly less spherical and slightly more filamentary (prolate).

- We have also investigated the relationship between formation time and halo properties such as shape, virial ratios, and spin which was not studied previously for the scales examined here. On average, haloes that formed more recently (young haloes) have higher values of the virial ratio, are less spherical, and have higher values of spin when observed at $z = 15$. This can be understood because the time passed between the formation of these young haloes and the end of the simulation is less than the relaxation time, $t_{\mathrm{relax}} \sim 60$ Myr, of these haloes.

- Although not expected from excursion set theory, we find that haloes with high spin are more strongly clustered, where clustering is quantified by the two-point correlation function of the positions of different dark matter haloes. This could mean that haloes born in clustered environments experience stronger tidal torques during their formation.

Now that the properties of dark matter mini-haloes are studied in detail, we should run a separate set of simulations that include baryonic physics. It would be interesting to study how the dark matter properties studied here are connected to the properties of the resulting Pop III stars.

5.2 Criterion for HD formation in primordial gas

- We find that the amount of HD that forms in the gas is closely related to the speed of the gravitational collapse. If the collapse is slow, it allows time for HD molecules to form, which lowers minimum gas temperatures by a factor of two.

- There are several physical mechanisms that can potentially delay the gravitational collapse of gas in dark matter mini-haloes (e.g. turbulence, rotation etc.). Contrary to previous studies, we find that the amount of HD that form in primordial gas depends little on physical properties such as the dark matter halo mass, rotation of gas inside the halo, or merger history of the halo. It seems likely that turbulence (disordered velocity fields) is playing an important role in delaying the collapse.

The direct next step would be to demonstrate the contribution from turbulence and rotation in delaying the collapse in a more explicit way. It would also be quite interesting to use the HD-rich and the HD-poor gas clouds we investigated in Chapter 4 as initial conditions and investigate the differences in their later stages of collapse.

Appendix A

Appendix

A.1 Comparison of structure formation simulation at large and small scales.

As a validity check for the data analysis method we adopt, and to make a qualitative comparison between structure formation occurring at different scales, we performed a numerical experiment to follow the evolution of gravitational structures at larger scales with relatively small particle numbers. The basic simulation parameters of this comparison simulation and the main simulation are listed in Table A.1, where L_{box} is the size of the simulation box, N_{par} is the number of dark matter particles included in the simulation, and z_{fin} is the redshift at which we terminate each of the simulations. Since the size of the simulation box differs by two orders of magnitude in the two runs, the mass scales of the gravitational structures found in each of the two runs differ by $\sim 10^6$.

In Fig. A.2, we show the formation time of dark matter haloes found in the 'Large' run, also identified by the method described in Section 2.2.1. These results are consistent with the formation times as derived from the Millennium Simulation (Harker et al., 2006). Comparing Fig. A.2 with Fig. 2.8, a striking difference in the mass dependence of the formation time at the two different regimes is recognised: for dark matter structures present in the $z = 0$ simulations, the formation redshift decreases as a function of halo mass. In Fig. A.3, the virial ratios of these haloes is presented (consistent with earlier findings of Hetznecker and Burkert 2006). Comparing with Fig. 2.5, it is clear that dark matter structures identified at $z = 0$ are substantially closer to virial equilibrium compared to those at $z = 15$. In Fig. A.1, the median values of the sphericity parameter and triaxiality parameter are presented, which are consistent with results obtained from analysing the Millennium Simulation (Bett et al.,

Table A.1: Simulation parameters

Run	N_{par}	L_{box} $(h^{-1} \text{ Mpc})$	z_{fin}	ϵ $(h^{-1} \text{ kpc})$
Large	512^3	100	0	4.0
Small	2048^3	1	15	0.01
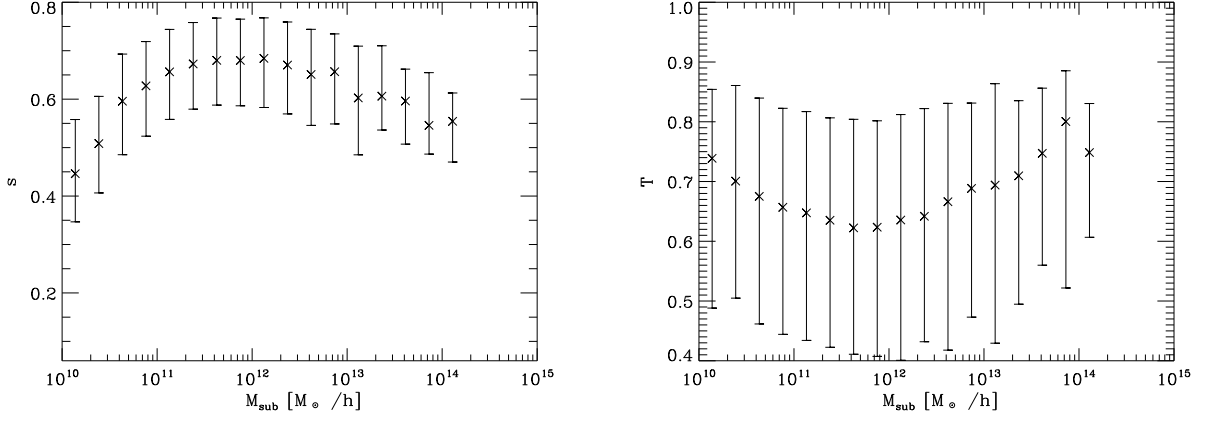
Figure A.1: Median of sphericity s and triaxiality T in different mass bins for dark matter haloes at $z = 0$. The sphericity and triaxiality are defined by equations (2.10) and (2.11), respectively.
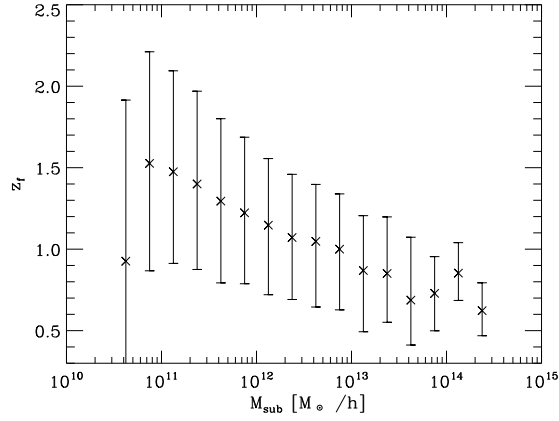
Figure A.2: Formation time of dark matter haloes as a function of their mass. Median, 20 %, and 80 % values in each mass bin are plotted. More massive dark matter haloes form at smaller redshift.
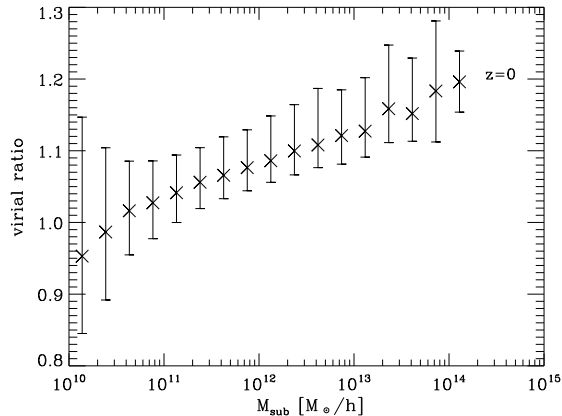
Figure A.3: Distribution of the virial ratio in dark matter haloes of different mass at redshift $z = 0$. The virial ratio is defined such that it converges to unity at virial equilibrium. Crosses indicate the median value of the virial ratio, while the error bars indicate the 20th and 80th percentiles. The mass bins are spaced logarithmically, and symbols are only plotted for bins containing at least 10 dark matter haloes.

2007). Comparison with Fig. 2.9 shows that halos found in the larger simulation box at lower redshift are much more spherical, and less prolate.

Overall, our results show good agreement with results found in the literature on large-scale structure formation at $z = 0$. This confirms the validity of the analysis methods we adopted in this work.

A.2 Influence of particle numbers on calculating sphericity parameter.

In order to test our algorithm to calculate the shape of dark matter haloes, we performed a series of controlled experiments; namely, we generated spherical distributions of particles with $\rho \propto r^{-2}$ from 100 different seeds for a range of particle numbers. Then, we deformed the sphere in y/z direction with a ratio of $b/a = 1$, $c/a = 2/3$, or $b/a = 1$, $c/a = 1/3$, or $b/a = 2/3, c/a = 1/3$ and finally calculated halo shapes using the prescription described in Section 2.3.5. We also measured the axis ratios of ideal spheres before applying any deformation. In this section, we adopt b/a and s $(=c/a)$ to describe the shape of the spheroid, rather than s and T $(=(a^2 - b^2)/(a^2 - c^2))$, as in other parts of this paper. This is because triaxiality cannot be defined properly for an ideal sphere.

In Table A.2, the average over 100 realisations is shown with an error bar that indicates the standard deviation obtained from 100 realisations for different types of spheroids investigated here. There is a general trend that with increasing number of

Table A.2: Convergence study of our method to calculate halo shapes described in Section 2.3.5 using several different types of spheroids. Average and standard deviation is calculated from 100 realisations in each case.

real value	No. of particles	c/a	b/a
b/a=1, c/a=1	100	0.8135 (0.0575)	0.9083 (0.0484)
	200	0.8649 (0.0467)	0.9345 (0.0327)
	500	0.9109 (0.0296)	0.9558 (0.0228)
	1000	0.9402 (0.0217)	0.9708 (0.0184)
	2000	0.9562 (0.0147)	0.9782 (0.0131)
b/a=1, c/a=2/3	100	0.6209 (0.0557)	0.8917 (0.0528)
	200	0.6354 (0.0392)	0.9222 (0.0415)
	500	0.6468 (0.0278)	0.9476 (0.0294)
	1000	0.6532 (0.0196)	0.9655 (0.0206)
	2000	0.6571 (0.0129)	0.9758 (0.0144)
b/a=1, c/a=1/3	100	0.3099 (0.0293)	0.8822 (0.0600)
	200	0.3175 (0.0200)	0.9152 (0.0472)
	500	0.3234 (0.0125)	0.9423 (0.0286)
	1000	0.3276 (0.0083)	0.9618 (0.0198)
	2000	0.3292 (0.0063)	0.9734 (0.0144)
b/a=2/3, c/a=1/3	100	0.3286 (0.0325)	0.6647 (0.0635)
	200	0.3313 (0.0227)	0.6658 (0.0476)
	500	0.3328 (0.0141)	0.6661 (0.0316)
	1000	0.3339 (0.0092)	0.6662 (0.0214)
	2000	0.3334 (0.0064)	0.6658 (0.0138)
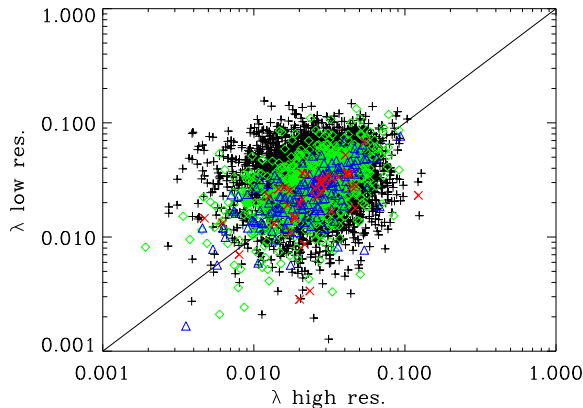
Figure A.4: Non-dimensional spin parameter calculated from high-resolution (2048^3) simulation and lower-resolution (512^3) simulation. Black plus signs denote 'main' subhalo with ≤ 300 particles, green diamonds > 300, ≤ 1000 particles, blue triangles > 1000, ≤ 3000 particles, red crosses > 3000 particles in the lower resolution simulation.

particles the measured axial ratios become ever closer to the real underlying value, and the standard deviation decreases.

It is shown here that in cases where the underlying values of c/a or b/a are unity, the real value and the estimated value do not match within standard deviations even with 2000 particles. Thus, our method tends to underestimate the axial ratios when they are close to unity. This tendency was already recognised earlier by Dubinski and Carlberg (1991), who performed similar numerical experiments for their method to estimate halo shapes (their method is not exactly identical to the method we adopted in this work).

A.3 Resolution study of the non-dimensional spin parameter

Since the non-dimensional spin parameter λ is known to depend severely on how well the dark matter structure is resolved, we performed a resolution study by running a lower-resolution version of our 'Small' run with 512^3 particles adopting the same cosmological parameters and the same random seed for initial conditions. By matching dark matter haloes at $z = 15$ in two different runs according to their positions, we compared the non-dimensional spin parameter. According to Fig. A.4, we find that haloes with > 1000 particles in the lower resolution run, have relatively good convergence. Therefore, for the high-resolution production run, we show the spin parameter of only haloes with ≥ 1000 particles, assuming that they have enough particles to capture the intrinsic angular momentum.

A.4 Non-dimensional spin parameter calculated for FOF haloes

In Fig. A.5, we present the non-dimensional spin parameter calculated for each **FOF haloes** as a function of mass. Comparison with Fig. 2.3 shows that FOF gives a positive correlation between spin and halo mass, which is not present for substructures identified by SUBFIND.

A.5 Density slice through the whole box.

In Fig. A.6 and A.7, we present the density projection on to the x-y and x-z planes from our 'Small' and 'Large' runs, respectively, in order to illustrate the differences in structure formation at different scales.
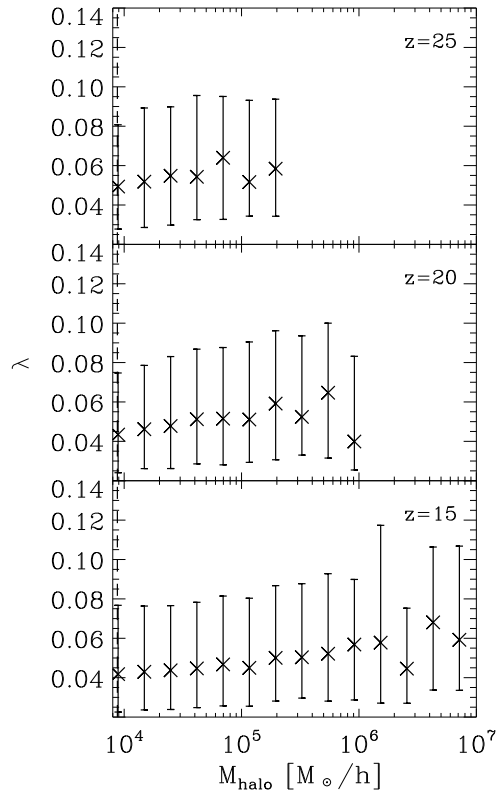
Figure A.5: Distribution of the dimensionless spin parameter λ in dark matter haloes of different mass at redshift $z \sim 25$ (top panel), $z \sim 20$ (middle panel), and $z \sim 15$ (bottom panel) calculated for **FOF haloes**. Crosses indicate the median value of λ, while the error bars indicate the 20th and 80th percentiles. The dashed vertical lines represent lower mass limit of 1000 particles.
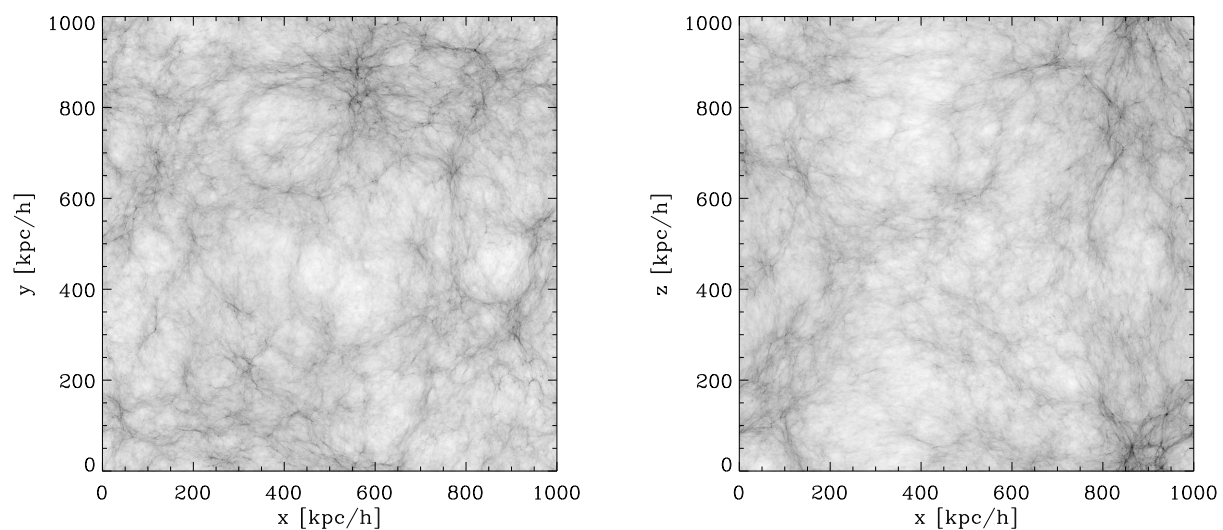
Figure A.6: A density projection on to the *x-y* (*x-z*) plane through the centre of the
box with thickness one-fifth of the simulation box size for our 'Small' run
at $z = 15$.
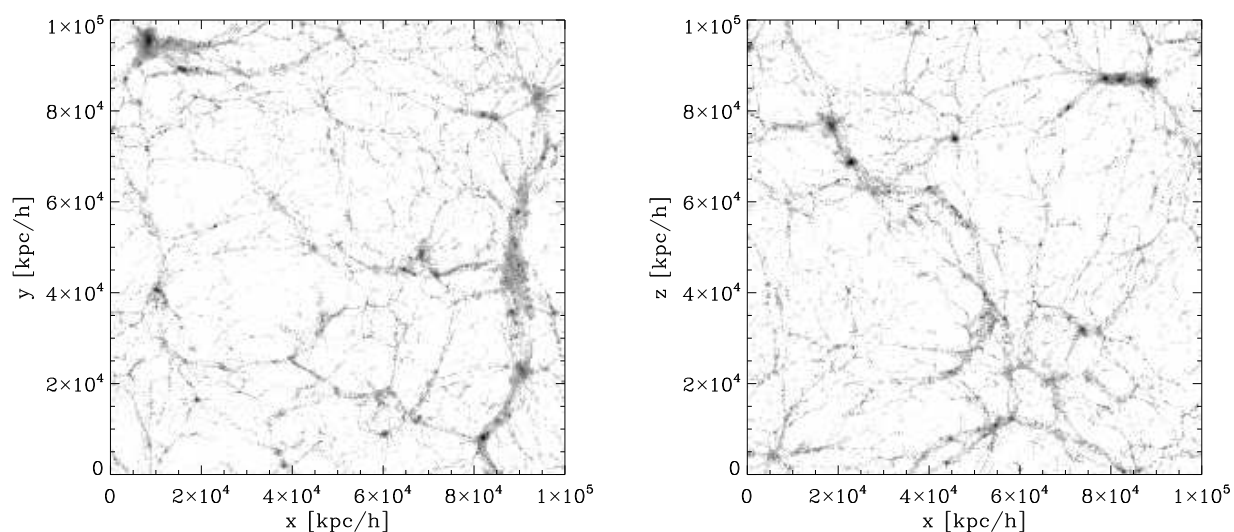
Figure A.7: A density projection on to the *x-y* (*x-z*) plane through the centre of box
with thickness one-fifth of the simulation box size for our 'Large' run at
$z = 0$.

Bibliography

Abel, T., Bryan, G. L., and Norman, M. L. (2002). The Formation of the First Star in the Universe. *Science*, 295:93–98.

Allgood, B., Flores, R. A., Primack, J. R., Kravtsov, A. V., Wechsler, R. H., Faltenbacher, A., and Bullock, J. S. (2006). The shape of dark matter haloes: dependence on mass, redshift, radius and formation. MNRAS, 367:1781–1796.

Ballesteros-Paredes, J. (2006). Six myths on the virial theorem for interstellar clouds. MNRAS, 372:443–449.

Barnes, J. and Hut, P. (1986). A hierarchical O(N log N) force-calculation algorithm. Nature, 324:446–449.

Bertschinger, E. and Gelb, J. M. (1991). Cosmological N Body Simulations. *Computers in Physics*, 5(2).

Bett, P., Eke, V., Frenk, C. S., Jenkins, A., Helly, J., and Navarro, J. (2007). The spin and shape of dark matter haloes in the Millennium simulation of a Λ cold dark matter universe. MNRAS, 376:215–232.

Binney, J. and Tremaine, S. (2008). *Galactic Dynamics: Second Edition*. Princeton University Press.

Bond, J. R., Cole, S., Efstathiou, G., and Kaiser, N. (1991). Excursion set mass functions for hierarchical Gaussian fluctuations. ApJ, 379:440–460.

Bond, J. R. and Efstathiou, G. (1984). Cosmic background radiation anisotropies in universes dominated by nonbaryonic dark matter. ApJ, 285:L45–L48.

Bouwens, R. J., Illingworth, G. D., Oesch, P. A., Labbé, I., Trenti, M., van Dokkum, P., Franx, M., Stiavelli, M., Carollo, C. M., Magee, D., and Gonzalez, V. (2011). Ultraviolet Luminosity Functions from 132 z ˜ 7 and z ˜ 8 Lyman-break Galaxies in the Ultra-deep HUDF09 and Wide-area Early Release Science WFC3/IR Observations. ApJ, 737:90.

Bovino, S., Latif, M. A., Grassi, T., and Schleicher, D. R. G. (2014). Dark-matter halo mergers as a fertile environment for low-mass Population III star formation. MNRAS, 441:2181–2187.

Bromm, V. (2013). Formation of the first stars. *Reports on Progress in Physics*, 76(11):112901.

Bromm, V., Coppi, P. S., and Larson, R. B. (2002). The Formation of the First Stars. I. The Primordial Star-forming Cloud. ApJ, 564:23–51.

Bromm, V., Ferrara, A., Coppi, P. S., and Larson, R. B. (2001). The fragmentation of pre-enriched primordial objects. MNRAS, 328:969–976.

Bromm, V. and Loeb, A. (2003). The formation of the first low-mass stars from gas with low carbon and oxygen abundances. Nature, 425:812–814.

Bromm, V. and Loeb, A. (2004). Accretion onto a primordial protostar. New A, 9:353–364.

Bromm, V. and Loeb, A. (2006). High-Redshift Gamma-Ray Bursts from Population III Progenitors. ApJ, 642:382–388.

Bullock, J. S., Kolatt, T. S., Sigad, Y., Somerville, R. S., Kravtsov, A. V., Klypin, A. A., Primack, J. R., and Dekel, A. (2001). Profiles of dark haloes: evolution, scatter and environment. MNRAS, 321:559–575.

Burles, S. and Tytler, D. (1998). The Deuterium Abundance toward Q1937-1009. ApJ, 499:699–712.

Clark, P. C., Glover, S. C. O., and Klessen, R. S. (2008). The First Stellar Cluster. ApJ, 672:757–764.

Clark, P. C., Glover, S. C. O., Klessen, R. S., and Bromm, V. (2011a). Gravitational Fragmentation in Turbulent Primordial Gas and the Initial Mass Function of Population III Stars. ApJ, 727:110.

Clark, P. C., Glover, S. C. O., Smith, R. J., Greif, T. H., Klessen, R. S., and Bromm, V. (2011b). The Formation and Fragmentation of Disks Around Primordial Protostars. *Science*, 331:1040–.

Crocce, M., Pueblas, S., and Scoccimarro, R. (2006). Transients from initial conditions in cosmological simulations. MNRAS, 373:369–381.

Dalgarno, A. and McCray, R. A. (1972). Heating and Ionization of HI Regions. ARA&A, 10:375.

Davis, A. J., D'Aloisio, A., and Natarajan, P. (2011). Virialization of high-redshift dark matter haloes. MNRAS, 416:242–247.

Davis, A. J. and Natarajan, P. (2009). Angular momentum and clustering properties of early dark matter haloes. MNRAS, 393:1498–1502.

Davis, A. J. and Natarajan, P. (2010). Spin and structural halo properties at high redshift in a Λ cold dark matter universe. MNRAS, 407:691–703.

Davis, M., Efstathiou, G., Frenk, C. S., and White, S. D. M. (1985). The evolution of large-scale structure in a universe dominated by cold dark matter. ApJ, 292:371–394.

de Souza, R. S., Ciardi, B., Maio, U., and Ferrara, A. (2013). Dark matter halo environment for primordial star formation. MNRAS, 428:2109–2117.

de Souza, R. S., Ishida, E. E. O., Whalen, D. J., Johnson, J. L., and Ferrara, A. (2014). Probing the stellar initial mass function with high-z supernovae. MNRAS, 442:1640–1655.

Diemand, J., Kuhlen, M., Madau, P., Zemp, M., Moore, B., Potter, D., and Stadel, J. (2008). Clumps and streams in the local dark matter distribution. Nature, 454:735–738.

Dopcke, G., Glover, S. C. O., Clark, P. C., and Klessen, R. S. (2011). The Effect of Dust Cooling on Low-metallicity Star-forming Clouds. ApJ, 729:L3.

Dopcke, G., Glover, S. C. O., Clark, P. C., and Klessen, R. S. (2013). On the Initial Mass Function of Low-metallicity Stars: The Importance of Dust Cooling. ApJ, 766:103.

Dubinski, J. and Carlberg, R. G. (1991). The structure of cold dark matter halos. ApJ, 378:496–503.

Efstathiou, G., Frenk, C. S., White, S. D. M., and Davis, M. (1988). Gravitational clustering from scale-free initial conditions. MNRAS, 235:715–748.

Eisenstein, D. J. and Hu, W. (1998). Baryonic Features in the Matter Transfer Function. ApJ, 496:605–614.

Frebel, A. (2010). Stellar archaeology: Exploring the Universe with metal-poor stars. *Astronomische Nachrichten*, 331:474–488.

Furlanetto, S. R., Oh, S. P., and Briggs, F. H. (2006). Cosmology at low frequencies: The 21 cm transition and the high-redshift Universe. Phys. Rep., 433:181–301.

Galli, D. and Palla, F. (1998). The chemistry of the early Universe. A&A, 335:403–420.

Galli, D. and Palla, F. (2002). Deuterium chemistry in the primordial gas. Planet. Space Sci., 50:1197–1204.

Gao, L., Springel, V., and White, S. D. M. (2005). The age dependence of halo clustering. MNRAS, 363:L66–L70.

Gao, L. and White, S. D. M. (2007). Assembly bias in the clustering of dark matter haloes. MNRAS, 377:L5–L9.

Gao, L., Yoshida, N., Abel, T., Frenk, C. S., Jenkins, A., and Springel, V. (2007). The first generation of stars in the Λ cold dark matter cosmology. MNRAS, 378:449–468.

Glover, S. (2013). The First Stars. In Wiklind, T., Mobasher, B., and Bromm, V., editors, *Astrophysics and Space Science Library*, volume 396 of *Astrophysics and Space Science Library*, page 103.

Greif, T. H., Bromm, V., Clark, P. C., Glover, S. C. O., Smith, R. J., Klessen, R. S., Yoshida, N., and Springel, V. (2012). Formation and evolution of primordial protostellar systems. MNRAS, 424:399–415.

Greif, T. H., Springel, V., White, S. D. M., Glover, S. C. O., Clark, P. C., Smith, R. J., Klessen, R. S., and Bromm, V. (2011). Simulations on a Moving Mesh: The Clustered Formation of Population III Protostars. ApJ, 737:75.

Hamilton, A. J. S. (1993). Toward Better Ways to Measure the Galaxy Correlation Function. ApJ, 417:19.

Harker, G., Cole, S., Helly, J., Frenk, C., and Jenkins, A. (2006). A marked correlation function analysis of halo formation times in the Millennium Simulation. MNRAS, 367:1039–1049.

Heavens, A. and Peacock, J. (1988). Tidal torques and local density maxima. MNRAS, 232:339–360.

Heger, A. and Woosley, S. E. (2002). The Nucleosynthetic Signature of Population III. ApJ, 567:532–543.

Heger, A. and Woosley, S. E. (2010). Nucleosynthesis and Evolution of Massive Metal-free Stars. ApJ, 724:341–373.

Hetznecker, H. and Burkert, A. (2006). The evolution of the dark halo spin parameters λ and λ' in a ΛCDM universe: the role of minor and major mergers. MNRAS, 370:1905–1914.

Hinshaw, G., Larson, D., Komatsu, E., Spergel, D. N., Bennett, C. L., Dunkley, J., Nolta, M. R., Halpern, M., Hill, R. S., Odegard, N., Page, L., Smith, K. M., Weiland, J. L., Gold, B., Jarosik, N., Kogut, A., Limon, M., Meyer, S. S., Tucker, G. S., Wollack, E., and Wright, E. L. (2013). Nine-year Wilkinson Microwave Anisotropy Probe (WMAP) Observations: Cosmological Parameter Results. ApJS, 208:19.

Hirano, S., Hosokawa, T., Yoshida, N., Umeda, H., Omukai, K., Chiaki, G., and Yorke, H. W. (2014). One Hundred First Stars: Protostellar Evolution and the Final Masses. ApJ, 781:60.

Hoekstra, H., Yee, H. K. C., and Gladders, M. D. (2004). Properties of Galaxy Dark Matter Halos from Weak Lensing. ApJ, 606:67–77.

Ishiyama, T., Fukushige, T., and Makino, J. (2009). Variation of the Subhalo Abundance in Dark Matter Halos. ApJ, 696:2115–2125.

Ishiyama, T., Rieder, S., Makino, J., Portegies Zwart, S., Groen, D., Nitadori, K., de Laat, C., McMillan, S., Hiraki, K., and Harfst, S. (2013). The Cosmogrid Simulation: Statistical Properties of Small Dark Matter Halos. ApJ, 767:146.

Jang-Condell, H. and Hernquist, L. (2001). First Structure Formation: A Simulation of Small-Scale Structure at High Redshift. ApJ, 548:68–78.

Katz, N., Hernquist, L., and Weinberg, D. H. (1999). The Clustering of High-Redshift Galaxies in the Cold Dark Matter Scenario. ApJ, 523:463–479.

Kauffmann, G., Colberg, J. M., Diaferio, A., and White, S. D. M. (1999). Clustering of galaxies in a hierarchical universe - I. Methods and results at z=0. MNRAS, 303:188–206.

Knebe, A., Pearce, F. R., Lux, H., Ascasibar, Y., Behroozi, P., Casado, J., Moran, C. C., Diemand, J., Dolag, K., Dominguez-Tenreiro, R., Elahi, P., Falck, B., Gottlöber, S., Han, J., Klypin, A., Lukić, Z., Maciejewski, M., McBride, C. K., Merchán, M. E., Muldrew, S. I., Neyrinck, M., Onions, J., Planelles, S., Potter, D., Quilis, V., Rasera, Y., Ricker, P. M., Roy, F., Ruiz, A. N., Sgró, M. A., Springel, V., Stadel, J., Sutter, P. M., Tweed, D., and Zemp, M. (2013). Structure finding in cosmological simulations: the state of affairs. MNRAS, 435:1618–1658.

Komatsu, E., Smith, K. M., Dunkley, J., and Bennett, C. L. (2011). Seven-year Wilkinson Microwave Anisotropy Probe (WMAP) Observations: Cosmological Interpretation. ApJS, 192:18.

Lacey, C. and Cole, S. (1994). Merger Rates in Hierarchical Models of Galaxy Formation - Part Two - Comparison with N-Body Simulations. MNRAS, 271:676.

Law, D. R., Majewski, S. R., and Johnston, K. V. (2009). Evidence for a Triaxial Milky Way Dark Matter Halo from the Sagittarius Stellar Tidal Stream. ApJ, 703:L67–L71.

Macciò, A. V., Dutton, A. A., and van den Bosch, F. C. (2008). Concentration, spin and shape of dark matter haloes as a function of the cosmological model: WMAP1, WMAP3 and WMAP5 results. MNRAS, 391:1940–1954.

Makino, J. (2002). An efficient parallel algorithm for O(N^2) direct summation method and its variations on distributed-memory parallel machines. New A, 7:373–384.

Makino, J., Taiji, M., Ebisuzaki, T., and Sugimoto, D. (1997). GRAPE-4: A Massively Parallel Special-Purpose Computer for Collisional N-Body Simulations. ApJ, 480:432–446.

Matzner, C. D. (2003). Supernova hosts for gamma-ray burst jets: dynamical constraints. MNRAS, 345:575–589.

McGreer, I. D. and Bryan, G. L. (2008). The Impact of HD Cooling on the Formation of the First Stars. ApJ, 685:8–20.

McLure, R. J., Dunlop, J. S., Cirasuolo, M., Koekemoer, A. M., Sabbi, E., Stark, D. P., Targett, T. A., and Ellis, R. S. (2010). Galaxies at z = 6-9 from the WFC3/IR imaging of the Hubble Ultra Deep Field. MNRAS, 403:960–983.

Meiksin, A. and Whalen, D. J. (2013). The radio signatures of the first supernovae. MNRAS, 430:2854–2863.

Moore, B., Kazantzidis, S., Diemand, J., and Stadel, J. (2004). The origin and tidal evolution of cuspy triaxial haloes. MNRAS, 354:522–528.

Neto, A. F., Gao, L., Bett, P., Cole, S., Navarro, J. F., Frenk, C. S., White, S. D. M., Springel, V., and Jenkins, A. (2007). The statistics of Λ CDM halo concentrations. MNRAS, 381:1450–1462.

Nishi, R. (2002). Star Formation in the Primordial Gas: Overview. *Progress of Theoretical Physics Supplement*, 147:1–9.

Nozawa, T., Kozasa, T., Umeda, H., Maeda, K., and Nomoto, K. (2003). Dust in the Early Universe: Dust Formation in the Ejecta of Population III Supernovae. ApJ, 598:785–803.

Oguri, M., Takada, M., Okabe, N., and Smith, G. P. (2010). Direct measurement of dark matter halo ellipticity from two-dimensional lensing shear maps of 25 massive clusters. MNRAS, 405:2215–2230.

Omukai, K. (2000). Protostellar Collapse with Various Metallicities. ApJ, 534:809–824.

Omukai, K. and Nishi, R. (1998). Formation of Primordial Protostars. ApJ, 508:141–150.

Omukai, K. and Palla, F. (2001). On the Formation of Massive Primordial Stars. ApJ, 561:L55–L58.

Omukai, K. and Palla, F. (2003). Formation of the First Stars by Accretion. ApJ, 589:677–687.

O'Shea, B. W. and Norman, M. L. (2007). Population III Star Formation in a ΛCDM Universe. I. The Effect of Formation Redshift and Environment on Protostellar Accretion Rate. ApJ, 654:66–92.

Peebles, P. J. E. (1980). *The large-scale structure of the universe.*

Planck Collaboration, Ade, P. A. R., Aghanim, N., Armitage-Caplan, C., Arnaud, M., Ashdown, M., Atrio-Barandela, F., Aumont, J., Baccigalupi, C., Banday, A. J., and et al. (2013). Planck 2013 results. XVI. Cosmological parameters. *arXiv:1303.5076*.

Planck Collaboration, Ade, P. A. R., Aghanim, N., Armitage-Caplan, C., Arnaud, M., Ashdown, M., Atrio-Barandela, F., Aumont, J., Baccigalupi, C., Banday, A. J., and et al. (2014). Planck 2013 results. XXIV. Constraints on primordial non-Gaussianity. A&A, 571:A24.

Plewa, T. and Müller, E. (1999). The consistent multi-fluid advection method. A&A, 342:179–191.

Press, W. H. and Schechter, P. (1974). Formation of Galaxies and Clusters of Galaxies by Self-Similar Gravitational Condensation. ApJ, 187:425–438.

Prieto, J., Jimenez, R., and Martí, J. (2012). Dark matter merging induced turbulence as an efficient engine for gas cooling. MNRAS, 419:3092–3108.

Reed, D. S., Bower, R., Frenk, C. S., Jenkins, A., and Theuns, T. (2007). The halo mass function from the dark ages through the present day. MNRAS, 374:2–15.

Ripamonti, E. (2007). The role of HD cooling in primordial star formation. MNRAS, 376:709–718.

Santoro, F. and Shull, J. M. (2006). Critical Metallicity and Fine-Structure Emission of Primordial Gas Enriched by the First Stars. ApJ, 643:26–37.

Sasaki, M., Clark, P. C., Springel, V., Klessen, R. S., and Glover, S. C. O. (2014). Statistical properties of dark matter mini-haloes at z ≥ 15. MNRAS, 442:1942–1955.

Schneider, R., Ferrara, A., Salvaterra, R., Omukai, K., and Bromm, V. (2003). Low-mass relics of early star formation. Nature, 422:869–871.

Shchekinov, Y. A. and Vasiliev, E. O. (2006). Formation of HD molecules in merging dark matter haloes. MNRAS, 368:454–460.

Sheth, R. K. and Tormen, G. (1999). Large-scale bias and the peak background split. MNRAS, 308:119–126.

Smith, R. J., Glover, S. C. O., Clark, P. C., Greif, T., and Klessen, R. S. (2011). The effects of accretion luminosity upon fragmentation in the early universe. MNRAS, 414:3633–3644.

Springel, V. (2010). E pur si muove: Galilean-invariant cosmological hydrodynamical simulations on a moving mesh. MNRAS, 401:791–851.

Springel, V., Wang, J., Vogelsberger, M., Ludlow, A., Jenkins, A., Helmi, A., Navarro, J. F., Frenk, C. S., and White, S. D. M. (2008). The Aquarius Project: the subhaloes of galactic haloes. MNRAS, 391:1685–1711.

Springel, V., White, S. D. M., Jenkins, A., Frenk, C. S., Yoshida, N., Gao, L., Navarro, J., Thacker, R., Croton, D., Helly, J., Peacock, J. A., Cole, S., Thomas, P., Couchman, H., Evrard, A., Colberg, J., and Pearce, F. (2005). Simulations of the formation, evolution and clustering of galaxies and quasars. Nature, 435:629–636.

Springel, V., White, S. D. M., Tormen, G., and Kauffmann, G. (2001). Populating a cluster of galaxies - I. Results at [formmu2]z=0. MNRAS, 328:726–750.

Stacy, A., Greif, T. H., and Bromm, V. (2010). The first stars: formation of binaries and small multiple systems. MNRAS, 403:45–60.

Stacy, A., Greif, T. H., and Bromm, V. (2012). The first stars: mass growth under protostellar feedback. MNRAS, 422:290–309.

Stadel, J., Potter, D., Moore, B., Diemand, J., Madau, P., Zemp, M., Kuhlen, M., and Quilis, V. (2009). Quantifying the heart of darkness with GHALO - a multibillion particle simulation of a galactic halo. MNRAS, 398:L21–L25.

Stahler, S. W., Palla, F., and Salpeter, E. E. (1986a). Primordial stellar evolution - The pre-main-sequence phase. ApJ, 308:697–705.

Stahler, S. W., Palla, F., and Salpeter, E. E. (1986b). Primordial stellar evolution - The protostar phase. ApJ, 302:590–605.

Susa, H. (2013). The Mass of the First Stars. ApJ, 773:185.

Tasitsiomi, A., Kravtsov, A. V., Gottlöber, S., and Klypin, A. A. (2004). Density Profiles of ΛCDM Clusters. ApJ, 607:125–139.

Tegmark, M., Silk, J., Rees, M. J., Blanchard, A., Abel, T., and Palla, F. (1997). How Small Were the First Cosmological Objects? ApJ, 474:1.

Todini, P. and Ferrara, A. (2001). Dust formation in primordial Type II supernovae. MNRAS, 325:726–736.

Tominaga, N., Umeda, H., and Nomoto, K. (2007). Supernova Nucleosynthesis in Population III 13-50 M_{solar} Stars and Abundance Patterns of Extremely Metal-poor Stars. ApJ, 660:516–540.

Trenti, M., Smith, B. D., Hallman, E. J., Skillman, S. W., and Shull, J. M. (2010). How Well do Cosmological Simulations Reproduce Individual Halo Properties? ApJ, 711:1198–1207.

Turk, M. J., Abel, T., and O'Shea, B. (2009). The Formation of Population III Binaries from Cosmological Initial Conditions. *Science*, 325:601–.

van den Bosch, F. C., Abel, T., Croft, R. A. C., Hernquist, L., and White, S. D. M. (2002). The Angular Momentum of Gas in Protogalaxies. I. Implications for the Formation of Disk Galaxies. ApJ, 576:21–35.

Warren, M. S., Quinn, P. J., Salmon, J. K., and Zurek, W. H. (1992). Dark halos formed via dissipationless collapse. I - Shapes and alignment of angular momentum. ApJ, 399:405–425.

Wechsler, R. H., Bullock, J. S., Primack, J. R., Kravtsov, A. V., and Dekel, A. (2002). Concentrations of Dark Halos from Their Assembly Histories. ApJ, 568:52–70.

Weinmann, S. M. and Lilly, S. J. (2005). The Number and Observability of Population III Supernovae at High Redshifts. ApJ, 624:526–531.

White, S. D. M. (1984). Angular momentum growth in protogalaxies. ApJ, 286:38–41.

Wiggins, B., Whalen, D. J., Migenes, V., and Astrophysics Research Group at Los Alamos National Laboratory (2014). Finding the First Cosmic Explosions: Hypernovae and Pair-Instability Supernovae. In *American Astronomical Society Meeting Abstracts #223*, volume 223 of *American Astronomical Society Meeting Abstracts*, page 102.02.

Yoshida, N., Abel, T., Hernquist, L., and Sugiyama, N. (2003). Simulations of Early Structure Formation: Primordial Gas Clouds. ApJ, 592:645–663.

Yoshida, N., Omukai, K., and Hernquist, L. (2008). Protostar Formation in the Early Universe. *Science*, 321:669–.

Yoshida, N., Omukai, K., Hernquist, L., and Abel, T. (2006). Formation of Primordial Stars in a ΛCDM Universe. ApJ, 652:6–25.

Yoshikawa, K., Yoshida, N., and Umemura, M. (2013). Direct Integration of the Collisionless Boltzmann Equation in Six-dimensional Phase Space: Self-gravitating Systems. ApJ, 762:116.